Microscopic modelling of compact stars and planets

Adrien Licari

Numéro national de thèse : 2016LYSEN022

THÈSE de DOCTORAT DE L'UNIVERSITÉ DE LYON
opérée par
l'École Normale Supérieure de Lyon

École Doctorale 52
Physique & Astrophysique de Lyon (PHAST)

Spécialité de doctorat : Astrophysique
Discipline : Physique

Soutenue publiquement le 20 septembre 2016, par :
Adrien Licari

Microscopic modelling of compact stars and planets

Modélisation microscopique des étoiles et planètes compactes

---

sous la direction de : **Gilles Chabrier et Stéphane Mazevet**

Devant le jury composé de :

M. Michel Koenig:	Laboratoire pour l'Utilisation des Lasers Intenses, Paris-Saclay	Président
M. Robert Mochkovitch:	Institut d'Astrophysique de Paris, Paris	Rapporteur
M. François Guyot:	Institut de Minéralogie et de Physique des Milieux Condensés, Paris	Rapporteur
M. Gilles Chabrier:	École Normale Supérieure de Lyon Lyon	Directeur
M. Stéphane Mazevet:	Laboratoire de l'Univers et THéories, Meudon	Directeur

Remerciements

Que dire dans ces quelques lignes... S'il est évident que je dois beaucoup, à de nombreuses personnes, pour m'avoir permis de mener cette thèse, il est toujours compliqué de coucher ces quelques mots sur le papier.

Commençons par le plus évident : je me dois ici de remercier mes deux directeurs, Gilles et Stéphane, pour m'avoir pris comme thésard et m'avoir permis de participer à cette aventure. Discuter longuement - de physique, mais pas que - avec eux a toujours été un plaisir, et j'ai pu grâce à eux découvrir le monde de la recherche en profondeur, et assister à plusieurs colloques ou écoles qui m'ont permis de parfaire ma formation de physicien.

Les collègues du CRAL, bien entendu, ont aidé par leurs éclairages et leurs discussions, parfois autour de nos recherches, parfois à côté : Alex, Mickaël, Pierre et Pierre, François, Jacques, Neil, Gérard, Christophe, Benoît ; et, bien sûr, Stéphanie, qui nous a toujours permis de faire nos recherches pendant qu'elle faisait tourner le laboratoire - que serions-nous sans elle ? Autour de cette équipe, je dois également remercier l'équipe du PSMN, notamment Loïs et Emmanuel, qui m'ont supporté à chaque fois que mes calculs ne voulaient pas compiler sur les serveurs. Et bien que je n'aie réellement passé qu'un mois à l'Observatoire de Paris-Meudon, j'ai pu passer quelques excellents moments - de recherche comme de détente - notamment avec Riccardo et Claire.

Au-delà de l'équipe du CRAL et de la thèse en elle-même, je voulais ici dire un mot de remerciement à l'École Normale Supérieure de Lyon, dans son ensemble, pour m'avoir acceuilli pendant sept années. Cette école a marqué des années charnières de ma formation, et de mon existence. Parmi les enseignants qui ont contribué à construire le physicien que je suis devenu, je pense - en vrac - à Henning Samtleben, Thierry Dauxois, Pierre Salati, Sébastien Manneville, Angel Alastuey, Arnaud Le Diffon, et encore bien d'autres... Tous ont su me transmettre la beauté d'un ou l'autre domaine de la physique. Par ailleurs, l'opportunité d'y enseigner trois ans, conjointement à ma thèse, a été une formidable occasion de me confronter une première fois à l'enseignement, qui était mon but premier.

Puisqu'on parle de l'École, au-delà des enseignements, il y a tous les autres, tous ceux que l'ont rencontre dans un tel lieu, et qui font un bout de chemin avec vous. Je ne puis là citer tous ceux qui m'ont apporté toutes ces années, sur tous les plans - social, intellectuel ailleurs qu'en physique, mais aussi associatif ou musical : Juan Pablo, Anh Thy, Aisling, Arthur, Élie, Maxime, Bibiane, Bertrand, Vincent et tous les - trop nombreux pour être cités - autres... Si ces années ont été pour moi aussi enrichissantes sur tous les plans, vous y êtes aussi pour beaucoup.

Bien entendu, je ne serais jamais arrivé dans cette école sans le soutien que j'ai pu avoir en amont : ma famille et notamment mes parents, depuis toujours, et mes propres enseignants successifs, de la primaire à la prépa, qui m'ont donné envie de faire ce métier. Cette thèse est l'aboutissement d'un parcours auquel ils ont pris part, par

leur écoute et leurs encouragements maintes fois renouvellés à poursuivre mon but.

Et enfin, bien sûr, la plus importante à mes yeux : Isabelle, ma fiancée, bientôt ma femme, qui m'a soutenu à travers l'agreg, à travers la thèse, à travers cette première année d'enseignement qui s'achève ; qui m'a donné la force de tenir bon quand les difficultés de la recherche me faisaient perdre espoir ; qui m'a encouragé à continuer quand je voulais abandonner ; et qui a patiemment corrigé l'anglais approximatif de ce manuscrit... Merci à toi.

Abstract

A correct knowledge of dense stars and planets need an accurate determination of the thermodynamic behavior of matter in these objects. One of the most efficient approaches nowadays is to perform ab initio simulations, using both the statistical physics formalism and the density functionnal theory. This approach has shown its capabilities by reproducing many experimental data.

In the first part of this thesis project, these methods are used to study planetary "ices", found in planets such as Uranus or Neptun. We first confirmed the existing literature on water (equations of state and existence of a superionic phase); we then extended these results to denser planets, such as the so-called "super-Jupiter" exoplanets. We reach very high pressures, until where the behavior is analytically established; this permitted us to construct a numerical fit for water in a very large temperature and pressure range. The other planetary ices (methane and ammonia) were then studied in the conditions of our solar system.

We then considered white dwarves, and their cooling dynamics: they are the most usual star remnants, so that they can be used as cosmochronometers. The composition of these objects lead to binary phase transitions, which can have important consequences on their cooling time. We used ab inition methods to investigate this binary diagram, and we suggest new numerical strategies, leading to new results which partially confirm the previous literature.

Résumé

La connaissance des étoiles et des planètes denses nécessite une détermination fine du comportement thermodynamique de la matière dans ces objets. L'une des approches les plus fécondes aujourd'hui est celle des simulations ab initio, utilisant le formalisme de la physique statistique et la théorie de la fonctionnelle de la densité. Cette approche a notamment montré ses performances en reproduisant avec succès un grand nombre de résultats expérimentaux.

Dans la première partie de ce travail de thèse, ces méthodes sont appliquées à l'étude des glaces, impliquées dans des planètes telles que Uranus ou Neptune. Nous avons dans un premier temps confirmé le travail pré-existant sur le cas de l'eau (équations d'état et existence d'une phase superionique), puis nos avons étendu ces résultats aux cas de planètes plus denses, telles que les exoplanètes appelées super-Jupiters. Nous atteignons des limites de pression auxquelles le comportement est analytiquement connu, nous permettant de proposer un ajustement numérique pour l'eau dans une gamme de pression et température extrêmement large. Les autres glaces (méthane et ammoniac) ont seulement été étudiés dans les conditions des planètes de notre système solaire.

Nous nous sommes ensuite intéressés au cas des naines blanches et à leur dynamique de refroidissement ; il s'agit des restes d'étoiles les plus courants, et ils peuvent ainsi être utilisés comme moyen de datation de la galaxie. En particulier, la composition de ces objets conduit à des transitions de phase binaires ayant de lourdes répercussions sur leur temps de refroidissement. Nous avons investigué ce diagramme binaire à l'aide d'une méthode ab initio, et nous proposons de nouvelles stratégies numériques ainsi que des résultats confirmant partiellement les récents travaux dans le domaine.

Contents

Remerciements ii

Abstract - Résumé iv

Introduction 3

I Studying dense plasmas: physical considerations and numerical approaches 6

1 Description of dense plasmas: an overview 8
I Plasma parameters . . . 9
II Plasma states evolution in the (P, T) plane . . . 11
III Conclusion . . . 13

2 Statistical mechanics and numerical simulations 14
I Statistical ensembles . . . 15
II Sampling the phase space . . . 17
III Estimating the relevant quantities from a microscopic configuration . . . 21
IV Conclusion . . . 26

3 The Thomas-Fermi model and the Density Functional Theory 28
I The Born-Oppenheimer approximation . . . 29
II The Thomas-Fermi model . . . 30
III Density Functional Theory . . . 32
IV Numerical use of the DFT . . . 38
V The Orbital-Free approach . . . 43
VI Conclusion . . . 44

II Planetary interiors: models and construction of equations of state for " ices " 45

4 How to build a planetary interior model 47
I The equations of a self-gravitating model . . . 48
II A quick overview of existing models for giant planets . . . 55
III Conclusion . . . 57

5 An equation of state for water in planetary interiors 59
I Water EOS and planetary interiors . . . 60
II Building our equation of state . . . 62

III A numerical fit . . . 67
IV Testing the equation of state: comparison with water shock experiments 70
V Conclusion . . . 73

6 Ammonia and methane: the other components of planetary "ices" 76
I Ammonia . . . 77
II Methane . . . 82
III Conclusion . . . 86

III Phase diagrams for White Dwarf Stars 88

7 A brief overview of white dwarfs and their cooling 90
I Introduction: white dwarfs and implications . . . 91
II Cooling theory of white dwarfs . . . 94
III Conclusion . . . 96

8 Binary mixtures crystallizing in white dwarfs 99
I State of the art . . . 100
II Our plasma mixture simulations . . . 102
III Results and discussion . . . 105
IV Conclusion . . . 109

IV Conclusions and perspectives 110

V Appendix 115

A Ewald sums 117
I Describing a periodic system . . . 118
II Separating the potential . . . 119
III Efficiently computing the long-ranged contribution . . . 121
IV Ewald sums and the pressure estimator . . . 123

B Hugoniot experiments 124
I Shock experiments: an overview . . . 125
II The Rankine-Hugoniot equations . . . 126
III Theoretically estimating the Hugoniot . . . 127

C Numerical Tables 131
I Water . . . 132
II Ammonia . . . 134
III Methane . . . 135

D Useful formulae 137
I The atomic units system . . . 138
II Unit conversions . . . 138
III Physical constants . . . 138
IV The degenerate electron gas . . . 138

Introduction

Even with our current knowledge of physics which has been built up over centuries, understanding the structure, evolution and properties of the objects present in our universe is by no means a simple task. A general picture of these objects - stars and planets - can be constructed from simple models ; for instance, the behavior of a gaseous sphere can be obtained from the equations of fluid dynamics (a review can be found, e.g., in [**?**]) ; and the general picture of the white dwarves behavior was understood as soon as 1926 by Fowler [**?**]. A simple polytropic model can already provide insight on observable characteristics such as the mass-radius relationship (the reader can find a review in [**?**]).

However, understanding the fine aspects of the structure and evolution of most common objects still raise many questions and the newest observations constantly force us to refine the picture ; 3438 planets are already discovered[1], and they challenge this simple picture. We can see on Figure (1) that the newly discovered planets challenge even more refined models (see, e.g., [**?**] for a review), forcing scientists to find finer models, taking into account many aspects of the underlying physics.

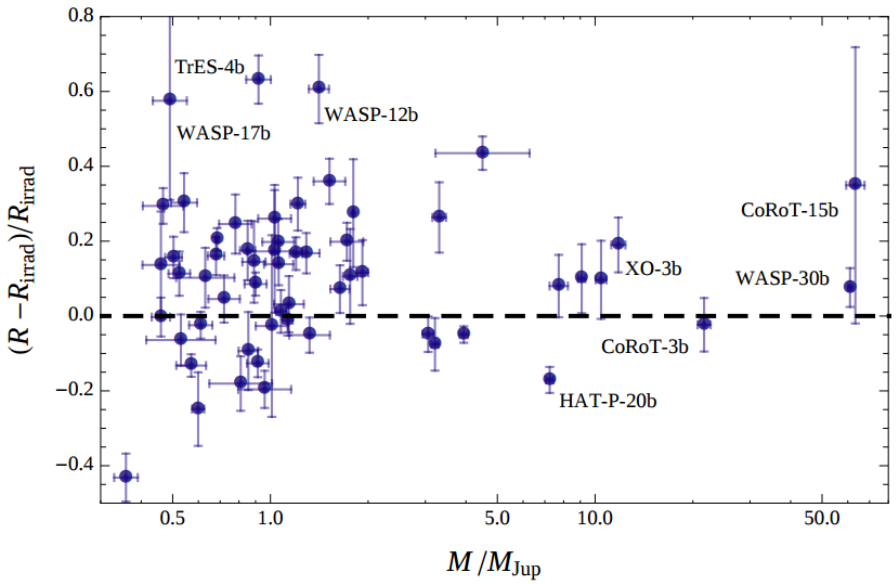

Figure 1: Relative radius excess between the observationally and the theoretically determined values for 57 transiting systems (taken from [**?**]). The theoretical mass-radius relationship is computed from a polytropic model taking irradiation from the star into account.

Among the challenging parts of these models are the object interior coupling with the atmosphere, or the detailed composition of the interior. This second point hides a lot of complexity : the thermodynamic behavior at such density and temperature

[1] Update of June, 27th 2016 on the exoplanets.eu website [**?**]

regimes are between difficult and impossible to reach in our experiments (a typical planetary interior pressure is a few Mbar, while dense stars such as white dwarfs can reach up to the Tbar regime ; for comparison, the highest pressures reached for water in compression experiments is 7 Mbar; moreover, planetary interiors show these pressures at relatively cold temperatures, around 10000 K, while shock-compression experiments reach much higher temperatures). The knowledge of a "simple" reliable equation of state for these systems is thus bound to a theoretical understanding. Reaching a usable knowledge is even more complicated since the planetary and stellar models often imply isentropic layers, and the isentropic pressure-density relationship is difficult to obtain in experimental or theoretical work. Evolutionary models also need the explicit knowledge of the entropy, thus making this difficulty important.

Moreover, phase transitions and binary mixtures effects can lead to major structural changes in the interior of a self-gravitating object ; a good example of this aspect is the still on-going research on the hydrogen-helium phase separation and its possible influence on the interior structure of Saturn.

These properties must be investigated within the theoretical framework of quantum statistical mechanics, describing the plasma as a mixture of ions and electrons, which may be described with a classical or a quantum approach depending on the thermodynamic conditions that reign in the considered object. These equations are generally impossible to solve analytically - excepted in rare cases in which simple approximations lead to a correct picture, such as the perfect gas or the perfect solid limits. In the case of liquids or complex electronic behavior - which is the case of the thermodynamic regimes we study - it is not possible. However, one can formulate these equations into a set of approximative - and very lengthy - numerical calculations. Thankfully, the numerical tools have grown more and more powerful during the past decades, allowing for these very complex calculations to extend the analytical limits. The Density Functional Theory formalism permits numerical experiments to be conducted, leading to a new insight on these complex questions.

This work is separated into three main parts, in which I detailed both the numerical tools we used and the research context in which this work is inserted:

- I first reviewed the various methods usable for studying the equations of state of a coupled plasma through various ranges of density and temperature. Indeed, the microscopic phenomena implied in the macroscopic behavior vary with the thermodynamic conditions, and may require various theoretical frameworks and numerical tools.

- The most important part of this work focuses on what are called "planetary ices", and mainly consist of water, ammonia and methane. In planetary interiors, these components are present in minor proportions in Jupiter or Saturn, but are major components of Uranus and Neptune. They also are found in some extrasolar planets, often called "Hot Neptunes". These components (or at least water and ammonia) show a rich phase diagram in this multi-megabar regime, and in particular they exhibit a superionic phase with interesting conducting properties. This phase may be a key ingredient for correct models of Uranus and Neptune, providing an explanation for their unusual magnetic field. In this context, the quantum behavior of electrons plays a key role. We use the Density

Functional Theory to construct ab initio simulations which permit us to determine the thermodynamic properties of ices in these conditions. Our aim is to extend the previous knowkedge to higher pressure regimes (thus accounting for very massive extrasolar planets, the so-called super-Jupiter) and to give an analytical representation of this equation of state. While the compression properties along the isentropic profile are the main goal here, we show that the superionic phase extends at higher densities.

- In a third part, we focused on white dwarfs stars ; they are the most common stellar remnants, and are used as cosmochronometers to estimate the age of the galaxy. In order to link their luminosity to their age, it is important to understand their cooling dynamics. As their temperatures decrease, white dwarves undergo a crystallization, which leads to an energy release modifying their luminosity. However, a white dwarf is composed mainly of carbon and oxygen mixtures. While it cools down, the shape of the binary diagram, together with the high gravity fields that are found in these objects, can lead to strong sedimentation effects. In consequence, cooling models are substantially affected by this binary phase diagram and can lead to an important difference in the estimated age of these objects. Therefore, we worked on a new determination of this binary mixture phase diagram. In this case, the electronic behavior is analytically well-known, and the complex part stems from the ionic part, which is simulated in our work.

Part I

Studying dense plasmas: physical considerations and numerical approaches

Chapter 1

Description of dense plasmas: an overview

Contents

I Plasma parameters 9

I.1 Density, ionic coupling and mixture composition 9

I.2 Electronic part of the plasma 9

I.3 Ionic degeneracy 10

II Plasma states evolution in the (P, T) plane 11

III Conclusion 13

I Plasma parameters

I.1 Density, ionic coupling and mixture composition

The ionic and electronic densities n, n_e can be represented by the ionic and electronic Wigner-Seitz radii, which is the mean inter-particle distance:

$$a_i = \left(\frac{3}{4\pi n}\right)^{1/3} \quad \text{and} \quad a_e = \left(\frac{3}{4\pi n_e}\right)^{1/3} \tag{1.1}$$

which are linked through electroneutrality:

$$n_e = \langle Z \rangle n \Rightarrow a_i = \langle Z \rangle^{1/3} a_e \tag{1.2}$$

The electronic one is often expressed in atomic units as the electronic density parameter:

$$r_s = \frac{a_e}{a_0} \tag{1.3}$$

where a_0 is the Bohr radius. It is intuitive from this expression that if r_s is of the order of 1, the bound states of the atoms will overlap, leading to pressure ionization. One of the most important parameters to characterize a plasma is the coupling parameter

$$\Gamma = \frac{\langle Z \rangle^2 e^2}{a_i k_B T} = \frac{\langle Z \rangle^{5/3} e^2}{a_e k_B T} \tag{1.4}$$

which is easily interpreted as the ratio of the typical potential interaction energy between ions and their kinetic energy. We can also define its electronic counterpart:

$$\Gamma_e = \frac{e^2}{a_e k_B T} \tag{1.5}$$

It is important to notice that we mapped the natural thermodynamic intensive parameters n, T to new intensive parameters r_s, Γ, which are constructed to immediately provide some insight about the physics that will be dominant in the considered conditions. This direct conversion may be used to obtain this information:

$$r_s = \left(\frac{3}{4\pi} \frac{\langle A \rangle}{\langle Z \rangle} \frac{\text{amu} a_0^3}{\rho}\right)^{1/3} \tag{1.6}$$

$$\Gamma = \frac{\langle Z \rangle^{5/3} e^2}{r_s k_B T} \tag{1.7}$$

where amu is the atomic mass unit and k_B is expressed in Hartree. Finally, since we are going to study ionic mixtures of k species represented by N_i ions each, we can define the number fraction of a given species j:

$$x_j = \frac{N_j}{\sum_{i=1}^{k} N_i}, \quad \sum_{i=1}^{k} N_i = N_{tot} \tag{1.8}$$

I.2 Electronic part of the plasma

A few other parameters may be relevant to estimate the electronic effect in a given regime. Since the electrons may exhibit a quantum behavior, it is important to find

a correct parameter for quantum effects. This is the role of the so-called degeneracy parameter:

$$\theta = \frac{k_B T}{E_F} \tag{1.9}$$

where E_F is the Fermi level of a perfect degenerate electron gas at r_s. The expression for E_F is different if the electrons are at moderate velocities or relativistic velocities. We recall that the Fermi wavevector is related to the density through $k_F = (3\pi n_e)^{1/3} = (9\pi/4)^{1/3}/r_s a_0$ and introduce yet another parameter to represent the relativistic nature of the electrons, the Fermi parameter:

$$x_F = \frac{\hbar k_F}{m_e c} = \left(\frac{9\pi}{4}\right)^{1/3} \frac{\alpha}{r_s} \tag{1.10}$$

with $\alpha \sim 1/137$ the fine structure constant. Above $x_F \sim 1$, the electrons are non-relativistic. This distinction leads to:

$$E_F = \begin{cases} \dfrac{\hbar^2 k_F^2}{2m_e} = \dfrac{e^2}{2a_0}\left(\dfrac{9\pi}{4}\right)^{2/3}\dfrac{1}{r_s^2} & \text{non-relativistic case} \\ \sqrt{(\hbar c k_F)^2 + (m_e c^2)^2} = m_e c^2\sqrt{1+x_F^2} & \text{relativistic case} \end{cases} \tag{1.11}$$

leading to the dimensionless degeneracy parameter:

$$\theta = \begin{cases} \left(\dfrac{4}{9\pi}\right)^{2/3} 2\langle Z\rangle^{5/3}\dfrac{r_s}{\Gamma} & \text{non-relativistic case} \\ \dfrac{\alpha^2}{\sqrt{1+x_F^2}}\dfrac{\langle Z\rangle^{5/3}}{\Gamma r_s} & \text{relativistic case} \end{cases} \tag{1.12}$$

I.3 Ionic degeneracy

In case the plasma is dense enough, quantum behavior may kick in for the ions as well. In consequence, we should exhibit a parameter for the ionic degeneracy. Since they can be either fermions or bosons, a transposition of the θ parameter is not suitable. It must also be underlined that the plasma physics do not exhibit ions behaving as a completely degenerate Fermi gas or a Bose condensate. We turn to a parameter constructed from the plasma ionic frequency:

$$\omega_P = \left[4\pi n \frac{e^2}{\text{amu}}\langle\frac{Z^2}{A}\rangle\right]^{1/2} \tag{1.13}$$

which can be compared to the temperature to create a suitable dimensionless parameter:

$$\eta = \frac{\hbar\omega_P}{k_B T} \tag{1.14}$$

The diffraction effects are important when η is not negligible against one. It is also possible to construct a parameter from the thermal de Broglie's wavelength $\Lambda = \sqrt{h^2/2\pi m k_B T}$:

$$\kappa = \frac{\Lambda}{a_i} = \sqrt{\frac{2\pi}{\langle A\rangle \text{amu}/m_e}}\langle Z\rangle^{-7/6}\sqrt{\frac{\Gamma}{r_s}} \tag{1.15}$$

When κ reaches around 1, the quantum behavior of the ions cannot be neglected anymore.

It is interesting to note that $\eta \sim T^{-1}\rho^{1/2}$, while $\kappa \sim T^{-1/2}\rho^{1/3}$; since the quantum effects can appear at high density or low temperature, η will reach unity faster than κ; in consequence, η will be kept as a useful parameter.

In summary, we provided $r_s, \Gamma, x, x_F, \theta$ and η; if all these parameters may seem a lot, ultimately they only depend on the temperature and the density, and the value of each of them give insight as to the relevant physical phenomena to be considered.

II Plasma states evolution in the (P, T) plane

Let us try to understand the microscopic physics that can occur if one varies thermodynamic conditions; the discussion to follow is summarized in Figure (1.1), and a similar discussion can be found in [**?**].

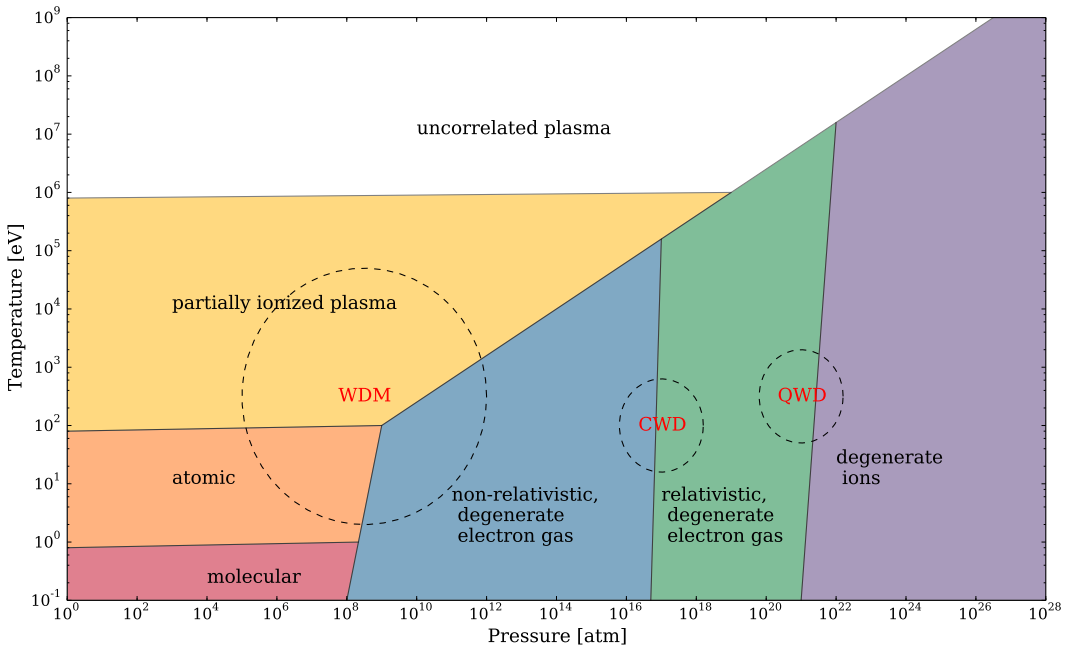

Figure 1.1: Evolution of the state of the matter in the (P, T) plane; the numerical values are indicative orders of magnitude and may have to be adapted depending on the considered species.

Under atmospheric conditions, matter is mainly found as stable molecules which interact through the classical Van der Waals interaction. The perfect gas equation may apply correctly, and the Van der Waals model may be required at higher densities. Increasing the temperature to around 1eV, the chemical bonds in the molecules may break, leading to an atomic state: the microscopic phenomena implied in these conditions are nearly the same.

At even higher temperatures ($\sim$ 1eV), partial ionization of the atoms will occur. If the density is sufficiently small, the ionization is correctly described by the Saha equation [**?**], and the system can be described as a mixture of classical perfect gases (ionic and electronic). This regime can be found, for example, in the solar photosphere ($r_s \sim 200, \Gamma \sim 0.5$). Finally, by increasing the temperature further, this thermal ionization will continue until the atoms are completely ionized and the kinetic effects are dominant. This is an uncorrelated regime, since the Γ parameter is less than 1 (e.g., in the attempts of controlled fusion the desired regime is at $r_s \sim 200, \Gamma \sim 10^{-5}$). In these regimes, $\theta \gg 1$, so that the electrons can be described by a classical perfect

gas without any problem. These cases are well described with the sole kinetic effects of the ion-electron mixture, and will not be our issue in this work.

Let us now start again from moderately hot regimes and increase the density - less than 1 eV: as the density increases, the inter-nucleus distance shortens and the potential around each nucleus is modified by its neighbours. This modification of the potential leads to a hybridization of the outermost bound states into propagating waves, until too few bound states remain to contain all electrons, see Figure (1.2). A more classical picture of this phenomenon is to consider that the typical radii of the outermost orbitals are larger than the inter-ionic distance a_i. This phenomenon is called *pressure ionization*; when it reaches the occupied states, around a particle density of $10^{17}\text{g}\cdot\text{cm}^{-3}$, it defines the boundary of the so-called warm dense matter (WDM) conditions. These conditions are relevant for planetary interiors [**?** **?**], for example, and they will be found in the second part of this work. In this zone, $\theta < 1$, so that the quantum behavior of the pressure-ionized electrons must be correctly accounted for; we will discuss this issue in Chapter 3. These thermodynamic conditions are the place of many interesting physical phenomena, such as a phase transition for hydrogen from an isolating to a conducting phase [**?** **?**], a hydrogen-helium demixing [**?** **?**], or a superionic phase of water [**?** **?**], the last of which will interest us in this work.

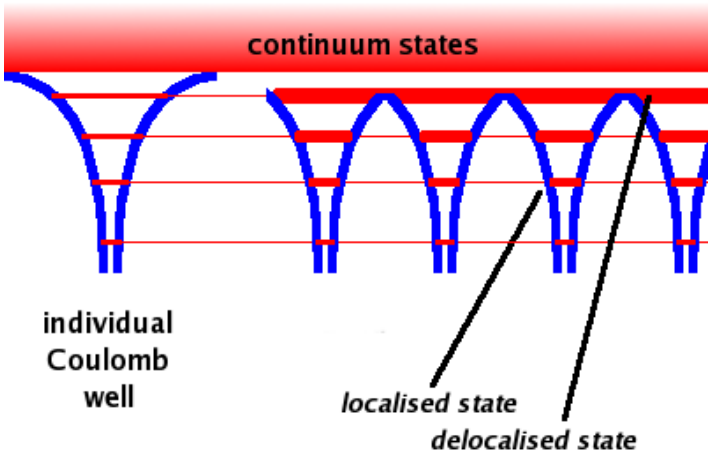

Figure 1.2: Pressure ionization mechanism: when the potential is modified, the bound states become delocalized

As the pressure increases, the system becomes totally ionized, and electron gas behave more and more as a perfect Fermi gas, since the Fermi energy increases with density faster than the interaction energy. In white dwarfs cores, the system can be described as the mixture of a perfect Fermi gas and a classical ion gas in a neutralizing weakly polarizable background whose effect in described through an effective ionic pair-potential. Such systems have been extensively studied, and various equations of state already exist, taking into account more or less fine effects [**?** **?** **?**]. The ions may arrange themselves in a crystal lattice or in a fluid phase, depending on the temperature; this phase transition has also been studied [**?** **?** **?**], and it has important consequences on the luminosity function of such objects [**?**].

At even higher pressures, the density may be such that the ions' de Broglie wavelengths overlap, and the system description must take into account the diffraction effects of the ions. Such extreme conditions are found the in the heavier white dwarfs

($M \sim 1.4 M_\odot$). Since we did not have time to exploit this method in this work, we will not give an overview of this description. This domain has been less studied that its classical counterpart [**?** **?**], although its importance in white dwarfs has been pointed out [**?** **?**].

III Conclusion

We have shown what parameters can be used to describe a plasma, and the typical phenomena that occur when these parameters reach some typical values. Depending on the thermodynamic conditions we consider, these parameters give us insight about which phenomena must be taken into account with a numerical procedure. We now turn to detail these procedures depending on the microscopic physics outlined here.

Chapter 2

Statistical mechanics and numerical simulations

Contents

I Statistical ensembles 15

II Sampling the phase space 17

II.1 Molecular Dynamics 17

II.2 Monte-Carlo methods 19

II.3 Finite size effects: how to ensure the volume properties are sampled 20

III Estimating the relevant quantities from a microscopic configuration 21

III.1 Macroscopic quantities 21

III.2 Pair correlation function 22

III.3 Lattice parameters 23

III.4 Dynamical quantities 24

IV Conclusion 26

The computer simulations of a given material are directly inspired from the statistical mechanics approach: given the microscopic equations of motion (which are generally the Newton laws of dynamics), one tries to infer the macroscopic properties of matter using statistical analysis.

This chapter is by no means an introduction to statistical mechanics. Such an introduction can be found in many reference books, including [**?**] or [**?**] (or in French, [**?**]). Our aim here is only to recall the necessary notions which are useful for a computer treatment, and reformulate them in an appropriate manner. It is important to notice that only indistinguishable classical particles (Boltzmannions) will be considered here.

I Statistical ensembles

Let us consider a system of N particles, described by their instantaneous positions and velocities $\{\mathbf{r}_i, \mathbf{p}_i\}$ and a Hamiltonian $\mathcal{H}(\{\mathbf{r}_i, \mathbf{p}_i\})$ - or, in the quantum picture, a Hamiltonian operator $\hat{\mathcal{H}}$ and its possible eigenstates $|\psi_\lambda\rangle$. From a macroscopic point of view, this system can be subject to diverse constraints, for instance fixed total energy, volume, pressure, temperature and so on. The macroscopic constraints define a macroscopic state of the system, while a particular point $\{\mathbf{r}_i, \mathbf{p}_i\}$ of the available phase space (hereafter denoted Γ) define a microscopic state.

What we call a statistical ensemble is a collection of such systems of N particles, all corresponding to the same macroscopic state, and with diverse microscopic states corresponding to:

- in the classical picture, a given probability distribution $p(\{\mathbf{r}_i, \mathbf{p}_i\}) = \frac{1}{\Omega} f(\{\mathbf{r}_i, \mathbf{p}_i\})$
- in the quantum picture, a given density matrix $\hat{\rho} = \frac{1}{\Omega} \sum_{\lambda=1}^{N_\lambda} f_\lambda |\psi_\lambda\rangle\langle\psi_\lambda|$

The partition function Ω corresponding to the ensemble is then the normalization constant of this probability distribution:

$$\Omega = \begin{cases} \dfrac{1}{N! h^{3N}} \displaystyle\int_\Gamma \prod_{i=1}^{N} d\mathbf{r}_i d\mathbf{p}_i f(\{\mathbf{r}_i, \mathbf{p}_i\}) & \text{in the classical case} \\ \dfrac{1}{N!} \mathrm{Tr}\left[\hat{f}\right] = \displaystyle\sum_{\lambda=1}^{N_\lambda} f_\lambda & \text{in the quantum case} \end{cases} \tag{2.1}$$

where the $N!$ term is only relevant in the case of indistinguishable particles.

Let us give some examples. The most basic ensemble is the microcanonical ensemble, defined by the macroscopic values of the internal energy U, the volume V and the number of particles N. In this case, the possible microscopic states are equiprobable, leading to the microcanonical partition function:

$$\Omega(U, V, N) = \begin{cases} \dfrac{1}{N! h^{3N}} \displaystyle\int_{\Gamma_{(N,V)}} \prod_{i=1}^{N} d\mathbf{r}_i d\mathbf{p}_i \delta(U - \mathcal{H}(\{\mathbf{r}_i, \mathbf{p}_i\})) \\ \dfrac{1}{N!} \mathrm{Tr}\left[\delta(U - \hat{\mathcal{H}})\right] \end{cases} \tag{2.2}$$

which is easily interpreted as the number of microscopic states compatible with the macroscopic constraint (U, V, N).

The other common ensemble, which will be the one considered in this work, is the canonical ensemble. It represents a system submitted to a fixed temperature T, a volume V and a number of particles N, and is generally thought of as a system in contact with a thermostat imposing its temperature. The corresponding probability distribution is the so-called Boltzmann distribution:

$$\begin{cases} f(\{\mathbf{r}_i, \mathbf{p}_i\}) = e^{-\beta \mathcal{H}(\{\mathbf{r}_i, \mathbf{p}_i\})} \\ \hat{f} = e^{-\beta \hat{\mathcal{H}}} \end{cases} \tag{2.3}$$

where $\beta = 1/k_B T$, k_B being the Boltzmann constant. In this case, the quantum canonical partition function is generally denoted Z and reads:

$$Z(T, V, N) = \begin{cases} \dfrac{1}{N! h^{3N}} \displaystyle\int_{\Gamma_{(N,V)}} \prod_{i=1}^{N} d\mathbf{r}_i d\mathbf{p}_i e^{-\beta \mathcal{H}(\{\mathbf{r}_i, \mathbf{p}_i\})} \\ \dfrac{1}{N!} \mathrm{Tr}\left[e^{-\beta \hat{\mathcal{H}}}\right] \end{cases} \tag{2.4}$$

In this case, the canonical function can be interpreted as the number of activated energy states: in the case $T \to 0$, only the ground-state will contribute to the macroscopic behavior, while in the limit $T \to \infty$, all the microscopic states will play a similar role.

A third common ensemble is the so-called grand-canonical ensemble, in which the number of particles is allowed to fluctuate with a fixed chemical potential μ. This ensemble is particularly suitable for the description of quantum statistics (fermions of bosons). The quantum grand-canonical partition reads:

$$\Xi(T, \mu, V) = \frac{1}{N!} \mathrm{Tr}\left[e^{-\beta(\hat{\mathcal{H}} - \mu N)}\right] \tag{2.5}$$

For the rest of this chapter, we will stick to the canonical description with Newtonian dynamics. We start with the classical part of (2.4); on nearly every system, the Hamiltonian is expressed as the sum of the kinetic and potential energies. Following this idea, the partition function is generally separated into two parts:

$$Z(T, V, N) = \frac{1}{N! h^{3N}} \int \prod_{i=1}^{N} d\mathbf{p}_i e^{-\beta \sum_i \frac{1}{2} \frac{\mathbf{p}_i^2}{m_i}} \int \prod_{i=1}^{N} d\mathbf{r}_i e^{-\beta \mathcal{V}(\{\mathbf{r}_i\})} \tag{2.6}$$

$$= \left(\frac{V}{\Lambda^3}\right)^N \int \prod_{i=1}^{N} d\mathbf{r}_i e^{-\beta \mathcal{V}(\{\mathbf{r}_i\})} \tag{2.7}$$

where $\mathcal{V}$ is the potential energy of the system and Λ the de Broglie wavelength of a particle. The second integral is called the configurational part of the partition function:

$$Z^{conf}(T, V, N) = \frac{1}{V^N} \int \prod_{i=1}^{N} d\mathbf{r}_i e^{-\beta \mathcal{V}(\{\mathbf{r}_i\})} \tag{2.8}$$

An interesting result is that the different ensembles yield the same properties when they reach the thermodynamic limit, i.e the limit

$$N \to \infty, V \to \infty, \frac{N}{V} \text{constant} \tag{2.9}$$

Of course, a partition function does not seem a practical tool at this point, since what we are interested in are the observables values of the system. Let us consider

then an observable $\mathcal{A}$ (e.g., the kinetic energy or the pressure), associated with its microscopic estimator $a(\{\mathbf{r}_i, \mathbf{p}_i\})$; the observed macroscopic value is defined as the mean of a over the ensemble:

$$\langle A \rangle_{ens} = \frac{1}{N! h^{3N}} \int_{\Gamma} \prod_{i=1}^{N} d\mathbf{r}_i d\mathbf{p}_i p(\{\mathbf{r}_i, \mathbf{p}_i\}) a(\{\mathbf{r}_i, \mathbf{p}_i\}) \tag{2.10}$$

The link between this ensemble mean and the measured value at a macroscopic scale is given by the ergodicity principle: given enough time, the system will explore the available phase space in a manner representative of the probability distribution. Finally the mean over the ensemble of microscopic states will equal the mean over time of one system:

$$\langle A \rangle_{ens} = \lim_{\tau \to \infty} \frac{1}{\tau} \int_0^{\tau} a(t) dt \tag{2.11}$$

From this point, we can specify what the aim of our numerical approach will be:

- we want to correctly sample the probability distribution $p(\{\mathbf{r}_i, \mathbf{p}_i\})$ in a reasonable amount of time; in other words, we want to create a subset of microscopic states small enough for the observables to be representative of the theoretical value defined in (2.10)
- we have to define a correct estimator for any observable we may be interested in; if this seems easy in the case of the kinetic or potential energy, it may be more complicated for the pressure or the temperature

II Sampling the phase space

Our aim in this section is to describe how one can generate a subset of microscopic states efficiently. We are going to review very quickly the two main methods: molecular dynamics and Monte-Carlo techniques. A more in-depth discussion can be found in several books or reviews, e.g. [**?** **?**], or more recently in [**?**]. We will also discuss the size of the microscopic system.

II.1 Molecular Dynamics

The idea of the Molecular Dynamics (MD) methods is to follow the Newtonian dynamics of the system:

$$\begin{cases} \dfrac{d\mathbf{r}_i}{dt} = \dfrac{\mathbf{p}_i}{m_i} & (2.12) \\ \dfrac{d\mathbf{p}_i}{dt} = -\nabla_i \mathcal{H}(\{\mathbf{r}_j, \mathbf{p}_j\}) = \mathbf{f}_i & (2.13) \end{cases}$$

where $\mathbf{f}_i$ is the total force exerted on the ion i. The idea is to exploit the ergodicity principle (2.11) over a finite period of time to estimate the observables. One generates the trajectory on M discrete time points t_k, and estimates the observables values by mean:

$$A = \frac{1}{M} \sum_{k=0}^{M} a(t_k) \tag{2.14}$$

In this approach, the first practical limitation will be the evaluation of the forces: since it requires N^2 evaluations (for a two-body interaction), it will be the most time-consuming part of the algorithm.

Integration scheme

If the general idea of the MD approach may seem simple, the practical use still requires caution. First of all, the integration scheme must be chosen carefully depending on the mathematical form of the interaction, and tested accordingly. Ideally, an integration algorithm should be time-reversible, energy-conserving, perfectly stable numerically, and permit a large enough time-step to generate a long-time solution with relatively few timesteps.

A classical approach is a finite-difference method: performing a Taylor expansion of the Newton equations of motion with a timestep δt, one can show that:

$$\begin{cases} \mathbf{r}_i(t+\delta t) = \mathbf{r}_i(t) + \dfrac{\mathbf{p}_i(t)}{m_i}\delta t + \dfrac{1}{2}\mathbf{a}_i(t)\delta t^2 + \dfrac{1}{6}\mathbf{b}_i(t)\delta t^3 + \dots & (2.15) \\ \mathbf{p}_i(t+\delta t) = \mathbf{p}_i(t) + m_i\mathbf{a}_i\delta t + \dfrac{1}{2}m_i\mathbf{b}_i(t)\delta t^2 + \dots & (2.16) \\ \mathbf{a}_i(t+\delta t) = \mathbf{a}_i(t) + \mathbf{b}_i(t)\delta t + \dots & (2.17) \\ & (2.18) \end{cases}$$

The practical limitation here is the evaluation of $\mathbf{a}_i, \mathbf{b}_i$ and so on to the desired accuracy. Since the errors accumulate, many smart methods have been designed to increase the efficiency and accuracy of the integration, such as predictor-corrector integration or adaptive stepsize algorithms (for more details on these methods, see for example [**?**]). The method we are going to use in the following is the so-called velocity Verlet algorithm [**?**] [**?**], in which the positions and the momenta are integrated on a staggered time grid:

$$\begin{cases} \mathbf{r}_i(t+\delta t) = \mathbf{r}_i(t) + \dfrac{\mathbf{p}_i(t+\frac{1}{2}\delta t)}{m_i} & (2.19) \\ \mathbf{p}_i(t+\dfrac{1}{2}\delta t) = \mathbf{p}_i(t-\dfrac{1}{2}\delta t) + \mathbf{f}_i(t)\delta t & (2.20) \\ & (2.21) \end{cases}$$

The pros of this simple algorithm are the time-reversibility, the oscillations stability and the few evaluations of the forces which are required (as opposed as the Runge-Kutta method, for instance). The energy conservation in the microcanical ensemble is often used as a test for the timestep choice.

Extension to the canonical sampling

Another point must be underlined here: the previously sampled probability distribution is the microcanonical ensemble. If one wants to sample the canonical ensemble, which is the most frequent case, the Newton equations must be modified in order to add the constrains associated to the constant of motion of the statistical ensemble.

Different algorithms have been proposed for this purpose. The best known is probably the Nose-Hoover method [**?**] [**?**], which supplements the equations of motion with a thermostat variable $s(t)$ with a thermal inertia Q, following its own evolution equation:

$$\begin{cases} \dot{\mathbf{r}}_i = \dfrac{\mathbf{p}_i}{m_i} & (2.22) \\ \dot{\mathbf{p}}_i = \dfrac{\mathbf{f}_i}{s^2} - 2\dfrac{\dot{s}\mathbf{p}_i}{m_i s} & (2.23) \\ Q\ddot{s} = \displaystyle\sum_i \frac{\mathbf{p}_i}{m_i}s - (f+1)\frac{k_B T}{s} & (2.24) \end{cases}$$

where f is the total number of degrees of freedom ($3N-3$ if the total momentum is fixed).

A simpler approach is to constrain the kinetic energy to a given value corresponding to the desired kinetic temperature:

$$\sum_i \frac{1}{2}\frac{\mathbf{p}_i^2}{m_i} = \frac{1}{2} f k_B T \tag{2.25}$$

It is clear here that this does not correspond to the canonical ensemble, but to the so-called isokinetic ensemble, in which the partition function is:

$$Z^K(T,V,N) = \frac{1}{N!h^{3N}} \int_{\Gamma(N,V)} \prod_{i=1}^{N} d\mathbf{r}_i d\mathbf{p}_i \delta\left(\sum_i \frac{1}{2}\frac{\mathbf{p}_i^2}{m_i} - \frac{1}{2} f k_B T\right) \tag{2.26}$$

In the thermodynamic limit, the isokinetic ensemble reaches the canonical one, since the configurational part of the integral is the same and the kinetic part is the same at the thermodynamic limit [**?**].

This may be achieved by diverse means: the more simple one is to brutally rescale the velocities at each time-step in order to ensure the desired kinetic energy [**?**]. A less crude approach [**?**] is to add a friction force to the equations of motion:

$$\begin{cases} \dot{\mathbf{r}}_i = \dfrac{\mathbf{p}_i}{m_i} & (2.27) \\ \dot{\mathbf{p}}_i = \mathbf{f}_i - \eta(\{\mathbf{r}_j, \mathbf{p}_j\})\mathbf{p}_i & (2.28) \end{cases}$$

with

$$\eta(\{\mathbf{r}_j, \mathbf{p}_j\}) = \frac{\sum_i \mathbf{f}_i \cdot \mathbf{p}_i / m_i}{\sum_i \mathbf{p}_i^2 / m_i} \tag{2.29}$$

This method is the one that will be used in the present work.

Let us mention two other possibilities. It is possible to soften the perturbation induced by the rescaling on the velocities: the rescaling can be spread over many timesteps [**?**]. This possibility is usable for equilibration processes, but does not samples a well-defined statistical ensemble. Finally, a hybrid approach was proposed by Bussi *et al.* [**?**], in which the velocity-rescaling does not aim at the thermostat temperature T_0 but at a randomly-picked temperature in a well-chosen distribution, which itself depends on the current temperature of the system. This approach directly generates the proper canonical distribution. Finally, it is worth mentionning than these methods can be generalized to sample other ensembles, such as the (P,T) ensemble.

II.2 Monte-Carlo methods

The other possibility to generate the probability distribution of a given ensemble is random states-generation. Since this method will not be used in this work, only a small sketch is given here.

Basically, if one tries to sample an integral of the form

$$A = \int a(x)p(x)dx \tag{2.30}$$

with x being a multidimensional variable, the idea is to generate M random points x in the phase space according to the probability distribution p, and the evaluation of the integral will be:

$$A \simeq \frac{1}{M}\sum_{k=1}^{M} a(x_k) \tag{2.31}$$

In one dimension, direct approaches such as the conventional quadratic procedure are more efficient than such a stochastic procedure; but in the case of multidimensional integrals such as (2.10), the direct approaches rapidly become computationally too expensive.

In the - most important - case of the canonical ensemble, another difficulty must be underlined. In this case, the probability distribution is the Boltzmann distribution, so that most points in the phase space do not contribute significantly to the configurational partition function (2.8) or to any observable (2.10). It would be more efficient to create a random set of points in the phase space which are likely to contribute to Z^{conf}. The solution to this problem is called importance sampling, and was first proposed by Metropolis *et al.* [**?**]; it consists in constructing any new phase space point from the previous one as a Markov chain. A more detailed discussion of this problem can be found in [**?**] and [**?**].

Let us illustrate the basics of this algorithm in the canonical ensemble. Starting from a given configuration x_k, one generates a trial point in the phase space x_t - e.g. by moving one particle randomly - and computes the quantity

$$p_k = e^{-\beta(\mathcal{V}(x_t)-\mathcal{V}(x_k))} \tag{2.32}$$

This trial configuration can now be accepted as a new state in the chain with a probability $\min(1, p_k)$. If the move is accepted, the newly generated state is the new one in the Markov chain, so that $x_{k+1} = x_t$; if not, the previous state x_k is recounted as x_{k+1}.

II.3 Finite size effects: how to ensure the volume properties are sampled

A simple question is: how big a system do we have to consider in order to have correct statistical properties of the system? In real-life experiments, the order of magnitude of the number of particles is the Avogadro number; but in numerical experiments, such a large system is out of reach. In fact, the most current methods consists in replicating the system: the simulated box is considered as a primitive cell which interacts with its own replicas. An illustration of this idea is given in Figure (2.1).

In the case of a short-ranged potential, such as the Lennard-Jones potential for instance, the user can define a cutoff range and consider the pair-forces to be null if two particles are further than this cutoff. The size of the system is then easily fixed: the box must be twice as large as the interaction cutoff, so that each particle only interacts with one replica of each other particle. In this case, the distance used to compute the pair's interaction is the minimum distance arising from all the images of the system; this is called the *minimum image convention*. It is still important to check that the thermodynamic quantities extracted from such a simulation are converged with respect to the size of the box and to the cutoff length; when these quantities are converged up to the desired precision, one can use this simulation size.

In the case of long-range interactions, such as Coulomb or gravitational forces, the lack of a typical length scale leads to the difficulty of defining such a cutoff. One can increase the box size until convergence is reached, but this is generally way too time-consuming. A widely used solution is presented in Appendix A, which consists in computing the contribution of the replicas in the Fourier space, where it has good convergence properties. The close contributions are still computed using the minimum image convention.

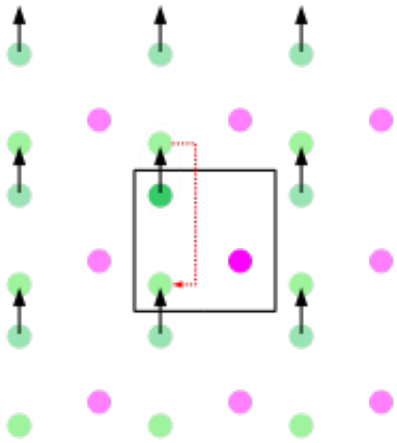

Figure 2.1: Representation of a periodicized system: the box represents the actually simulated system. The interaction between the green particles is not directly computed using the distance between them inside the cell, but using the minimum image convention, as shown by the arrow.

III Estimating the relevant quantities from a microscopic configuration

III.1 Macroscopic quantities

Here we are interested in estimating macroscopic quantities such as the energy or the pressure from microscopic states $\{\mathbf{r}_i, \mathbf{p}_i\}$ obtained from the simulation. For the kinetic and potential energies, the microscopic definition is straightforward and can be applied:

$$E_{pot}(\{\mathbf{r}_i, \mathbf{p}_i\}) = \frac{1}{2} \sum_{i=1, j=1, j\neq i}^{N} u_{pair}(|\mathbf{r}_j - \mathbf{r}_i|) \tag{2.33}$$

$$E_{kin}(\{\mathbf{r}_i, \mathbf{p}_i\}) = \sum_{i=1}^{N} \frac{\mathbf{p}_i^2}{m_i} \tag{2.34}$$

The case of the pressure is slightly more complicated. Applying the identity

$$P = -\left(\frac{\partial F}{\partial V}\right)_{N,T} = \left(\frac{1}{\beta Z}\frac{\partial Z}{\partial V}\right)_{N,T} \tag{2.35}$$

and using the typical length $a = V^{-1/3}$, one can express the coordinates as $\{\mathbf{u}_i a\}$, leading to:

$$Z^{conf}(T, V, N) = \int \prod_{i=1}^{N} d\mathbf{u}_i e^{-\beta \mathcal{V}(\{\mathbf{u}_i a\})} \tag{2.36}$$

with the integration over the cube of length 1. In this equation, one can see that only the potential energy contribution depends on V, so that:

$$P = NkT + \frac{1}{3V} \int \prod_{i=1}^{N} d\mathbf{r}_i \frac{\partial \mathcal{V}}{\partial V}(\{\mathbf{r}_i\}) \frac{1}{Z^{conf}} e^{-\beta \mathcal{V}(\{\mathbf{r}_i\})} \tag{2.37}$$

$$= NkT + \langle \frac{\partial \mathcal{V}}{\partial V} \rangle \tag{2.38}$$

This formula is true in the general case, but still cannot be used to define an estimator since the derivative of the potential energy is not straightforward. In the (usual) case of a potential energy which does not depend explicitly on the volume, the reduced coordinates $\{\mathbf{u}_i a\}$ can be re-used to show that:

$$\frac{\partial \mathcal{V}}{\partial V} = -\frac{1}{3V}\sum_{i=1}^{N} \nabla_i \mathcal{V} \cdot \mathbf{r}_i = \frac{1}{3V}\sum_{i=1}^{N} \mathbf{f}_i \cdot \mathbf{r}_i \tag{2.39}$$

where $\mathbf{f}_i$ is the force exerted on the particle i. This quantity is the well-known virial, and leads to the pressure estimator:

$$P = NkT + \frac{1}{3V}\int \prod_{i=1}^{N} d\mathbf{r}_i \sum_{i=1}^{N} \mathbf{f}_i \cdot \mathbf{r}_i p(\{\mathbf{r}_i, \mathbf{p}_i\}) \tag{2.40}$$

$$= NkT + \frac{1}{3V}\langle \sum_{i=1}^{N} \mathbf{f}_i \cdot \mathbf{r}_i \rangle \tag{2.41}$$

where $\mathbf{f}_i$ is the total force exerted on ion i. An estimator for the pressure is then:

$$P(\{\mathbf{r}_i, \mathbf{p}_i\}) = NkT + \frac{1}{3V}\sum_{i=1}^{N} \mathbf{f}_i \cdot \mathbf{r}_i \tag{2.42}$$

and use it to estimate the pressure in molecular dynamics or Monte-Carlo simulations. Nevertheless, the minimum image convention may create problems with this definition of the virial; we can reformulate it using the pair interactions:

$$\sum_{i=1}^{N} \mathbf{f}_i \cdot \mathbf{r}_i = \sum_{i=1}^{N}\sum_{j\neq i} \mathbf{f}_{j\to i} \cdot \mathbf{r}_i \tag{2.43}$$

$$= \frac{1}{2}\sum_{i=1}^{N}\sum_{j\neq i} (\mathbf{f}_{j\to i} \cdot \mathbf{r}_i + \mathbf{f}_{i\to j} \cdot \mathbf{r}_j) \tag{2.44}$$

$$= -\frac{1}{2}\sum_{i=1}^{N}\sum_{j\neq i} \mathbf{f}_{j\to i} \cdot (\mathbf{r}_j - \mathbf{r}_i) \tag{2.45}$$

In the case of a potential with an explicit dependence on V, one has to be more careful. Such a case is given in Appendix A, in which the Coulomb or Yukawa interactions are split into short-ranged and long-ranged contributions with a splitting parameter depending on V.

Another possibility is to evaluate the instantaneous stress tensor in order to obtain the pressure on the box via the trace. This approach can be found in [**?**] for instance.

In our computations, we will fix the box size; in consequence, we generally use the virial estimator, as it is simple and quick enough for very large particle numbers such as in our white dwarf simulations.

III.2 Pair correlation function

The pair correlation function $g(\mathbf{r}_1, \mathbf{r}_2)$ represents the probability of finding any particle at a position $\mathbf{r}_2$ knowing that another particle is at the fixed position $\mathbf{r}_2$. Intuitively, it will also be defined with the partition function. The usual normalized definition is:

$$g(\mathbf{r}_1, \mathbf{r}_2) = \frac{N(N-1)}{n^2 Z}\int \prod_{i=3}^{N} d\mathbf{r}_i e^{-\beta \mathcal{V}(\{\mathbf{r}_i\})} \tag{2.46}$$

where $n = N/V$ is the numerical density. The choice $i = 1, j = 2$ is obviously arbitrary in a system of identical particles. Generally, the system is isotropic, so that $g(\mathbf{r}_1, \mathbf{r}_2) = g(|\mathbf{r}_1 - \mathbf{r}_2|) = g(r)$.

The pair correlation function gives us insight on the structure of the system. Two limit cases are given on Figure (2.2): in the case of a perfect ideal crystal, the pair correlation function is a succession of peaks, while in the case of a liquid the sterical effects give a short-range structure and the long-range part reaches a uniform distribution. The normalization is such that this limit of the uniform distribution is 1.

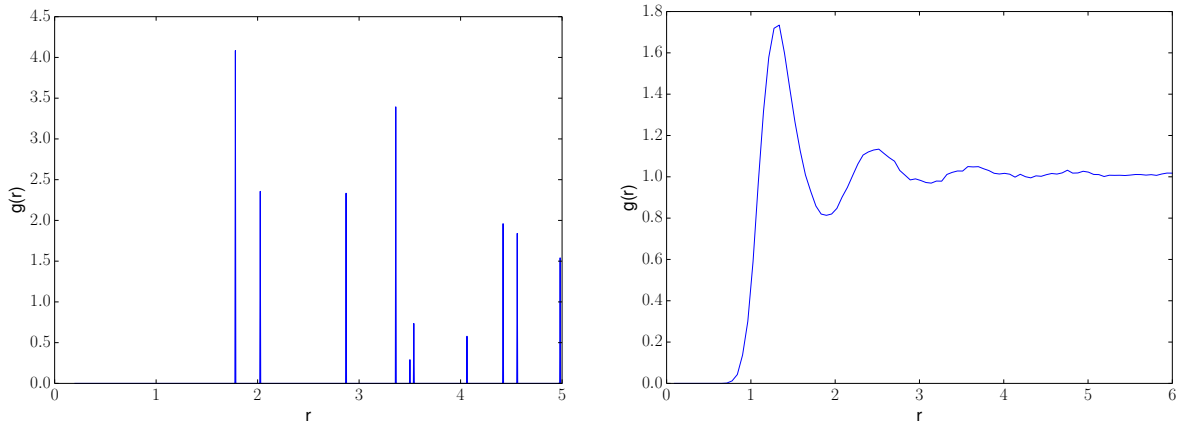

(a) Ideal BCC lattice

(b) Typical fluid phase

Figure 2.2: Typical pair distribution functions

If this definition is correct from a theoretical point of view, it is not very usable in the case of a numerical sampling. The following - equivalent - definition is much more useful:

$$g(r) = \frac{1}{n^2} \langle \sum_i \sum_{j \neq i} \delta(\mathbf{r}_i) \delta(\mathbf{r}_j - \mathbf{r}) \rangle \tag{2.47}$$

since it shows us after integration that the number of particles in a shell at distance r and width dr of a fixed particle is then given by:

$$\mathcal{N}(r, dr) = 4\pi r^2 g(r) dr \tag{2.48}$$

This formulation suggests to evaluate the pair-distribution function via a histogram of the inter-particular distances, which is quite straightforward.

III.3 Lattice parameters

It will be important in our work to identify if a collection of particles is in a solid or liquid phase. We must then use parameters to differentiate a lattice organization from a liquid structure. The pair correlation function may be one of these tools, since perfect lattices exhibit specific structures; but within a simulation, a solid phase is never exactly a perfect crystal arrangement, and thus broadens the peaks. Furthermore, the pair correlation functions of the liquid and of the solid are similar near the transition. More precise tools are then needed.

Many phase indicators can be used; one of the more accurate (but quite complex) is the local order parameter proposed in [**?**] or the global order parameter Q_6 proposed

by [**?**]; a review of the existing methods can be found in [**?**]. In this work, we will only use a simple centrosymmetry parameter, originally suggested in [**?**].

The centrosymmetry property of some lattices (e.g. FCC and BCC) can be used to build the so-called centrosymmetry parameter, which quantifies the local loss of centrosymmetry at an atomic site. The centrosymmetry parameter of an atom having N_n nearest neighbors is defined as

$$csp_j = \sum_{i=1}^{N_n/2} |\mathbf{r}_{i,j} + \mathbf{r}_{i+N_n/2,j}|^2 \tag{2.49}$$

where $\mathbf{r}_{i,j}$ and $\mathbf{r}_{i+N_n/2,j}$ are vectors from the central atom j to a pair of opposite neighbors. The number of nearest neighbors depends on the structure studied: in the cases relevant for this work, we can give the cases of a BCC structure (8 nearest neighbors) and of a FCC structure (12 nearest neighbors).

The interpretation is quite simple: in a perfectly centrosymmetric structure (e.g., BCC), the neighbor associated to $\mathbf{r}_i$ and the neighbor associated to $\mathbf{r}_{i+N_n/2}$ are such as $\mathbf{r}_{i+N_n/2} = -\mathbf{r}_i$, and the centrosymmetry parameter is exactly zero. In a real simulation, one has to find the requested nearest neighbors, and pair them in order to minimize the centrosymmetry parameter.

In this work, we adopted a normalized definition of the centrosymmetry parameter:

$$csp_j = \frac{1}{\sum_{i=1}^{N_n} |\mathbf{r}_{i,j}|^2} \sum_{i=1}^{N_n/2} |\mathbf{r}_{i,j} + \mathbf{r}_{i+N_n/2,j}|^2 \tag{2.50}$$

A histogram of typical centrosymmetry parameter distributions in a liquid and a solid phase are given in Figure (2.3).

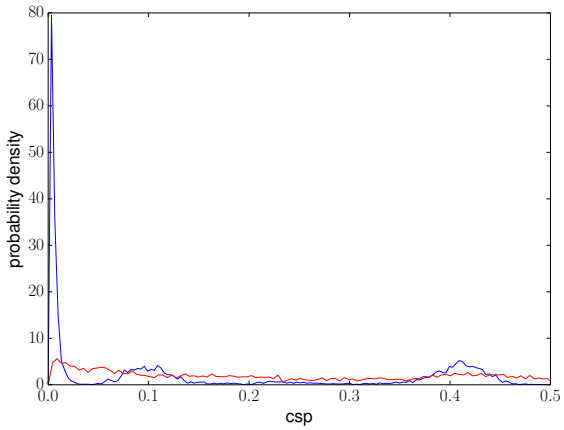

Figure 2.3: Typical distribution of the CSP values in a carbon plasma; in blue, BCC configuration with thermal broadening and defects; in red, liquid phase

III.4 Dynamical quantities

The main advantage of the Molecular Dynamics approach over the Monte-Carlo schemes is the access to the time evolution, giving the possibility of studying the relaxation or non-equilibrium dynamics. The dynamics are quantified with temporal correlation quantities. The general definition of a - non-normalized - correlation function between two quantities $\mathcal{A}$ and $\mathcal{B}$ is:

$$C_{\mathcal{AB}} = \langle (\mathcal{A} - \langle \mathcal{A} \rangle)(\mathcal{B} - \langle \mathcal{B} \rangle) \rangle \tag{2.51}$$

where the average is over the considered statistical ensemble (generally canonical or isokinetic). A time-correlation function between $\mathcal{A}$ and $\mathcal{B}$ is:

$$C_{\mathcal{AB}}(t_1, t_2) = \langle(\mathcal{A}(t1) - \langle\mathcal{A}\rangle)(\mathcal{B}(t2) - \langle\mathcal{B}\rangle)\rangle \tag{2.52}$$

Generally, the equilibrium correlation function is self-similar, so that it only depends on $t_2 - t_1$ and can be written:

$$C_{\mathcal{AB}}(t) = \langle(\mathcal{A}(t) - \langle\mathcal{A}\rangle)(\mathcal{B}(0) - \langle\mathcal{B}\rangle)\rangle \tag{2.53}$$

For identical quantities, $C_{\mathcal{AA}}(t)$ is called an autocorrelation function and its time integral (from $t = 0$ to $t = \infty$) is a correlation time $t_{\mathcal{A}}$.

The time correlation functions are useful since:

- they give quantified information on the dynamics of the system
- their time integrals are often related to transport cœfficients
- their Fourier transforms $\hat{C}_{\mathcal{AA}}(\omega)$ may often be related to experimental spectra

In this work, we are going to use the diffusion cœfficient as a complementary phase diagnostic: the particles diffuse in the liquid but not in the solid at the time scale considered in the simulation. The diffusion cœfficient is related to the velocity correlation time:

$$D = \frac{1}{3}\int_0^\infty \langle \mathbf{v}_i(t) \cdot \mathbf{v}_i(0)\rangle dt \tag{2.54}$$

or, using the corresponding Einstein relation (valid at long time):

$$2tD = \frac{1}{3}\langle|\mathbf{r}_i(t) - \mathbf{r}_i(0)|^2\rangle \tag{2.55}$$

We give a typical evolution of $\langle|\mathbf{r}_i(t) - \mathbf{r}_i(0)|^2\rangle$ on Figure (2.4), for both solid and liquid phases.

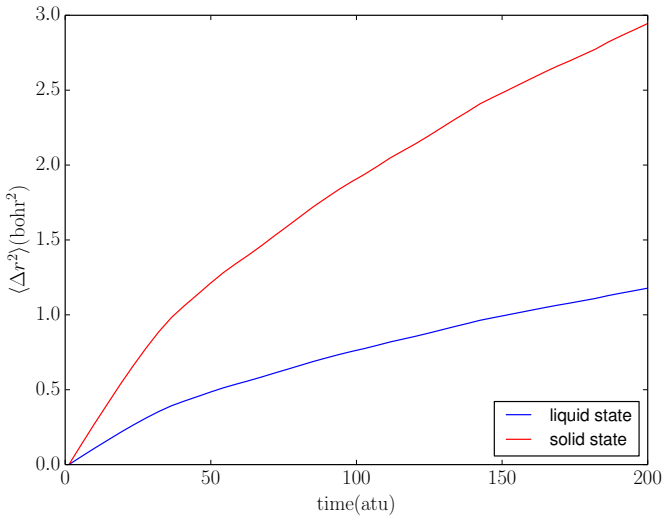

Figure 2.4: Typical mean-square displacement for solid and liquid states

IV Conclusion

We have shown how statistical mechanics can be used to design numerical schemes in order to extract thermodynamic properties of matter from first-principles physics. The knowledge of the partition function is difficult to extract, but macroscopic estimators allow us to access the relevant first-order derivatives, such as the energy or the pressure of the system at fixed (N, V, T). In addition, the molecular dynamics methods gives access to dynamic quantities, such as the diffusion coefficients.

We assumed the system could be reduced to a collection of particles subjected to Newtonian dynamics; this is generally a good description of a molecular or atomic system, as well as of the ions in a plasma, since they interact through a classical Lennard-Jones or Coulomb potential. In the case where the electrons are not linked to the ions, their behavior is generally more difficult to take into account. In the case of very dense systems such as classical white dwarfs, the electrons behave nearly as a perfect quantum polarizable gas, and their contribution can be included into an effective pair potential between the nucleus; as a consequence, all the tools we outlined in this chapter can still apply. However, there exists a whole range of conditions - planetary interiors for instance - in which the electrons exhibit a highly quantum behavior, but cannot be simulated with a simple effective potential. In the next chapter, we are going to review the most widely used theory which tackles this issue.

Chapter 3

The Thomas-Fermi model and the Density Functional Theory

Contents

I The Born-Oppenheimer approximation 29

II The Thomas-Fermi model 30

III Density Functional Theory 32

III.1 Hohenberg-Kohn theorems 32

III.2 The Kohn-Sham formulation 34

III.3 Mathematical representations of the exchange-correlation functional 36

III.4 Finite-temperature DFT 37

IV Numerical use of the DFT 38

IV.1 Numerical procedure 38

IV.2 Solving the Kohn-Sham equation into the reciprocal space . . 38

IV.3 Replacing the ions with pseudo-potentials 41

V The Orbital-Free approach 43

VI Conclusion 44

We saw in the previous chapter that a system described by a classical Hamiltonian can be simulated, and statistical properties extracted from this simulation. However, in the case of Molecular Dynamics (MD) simulations, the capacity to solve the hamiltonianian equations of motion is necessary. This is perfectly sufficient for molecular or ionic systems which are correctly described by Newtonian dynamics.

However, when the density of the system increases, pressure ionization takes place and the electrons exhibit highly quantum behavior; therefore, they are not correctly described by Newtonian dynamics. We must then try to find another formalism in which one can simulate the correct behavior for the electrons, and insert it into the methods we exposed in chapter 2.

We will first discuss the core approximation of this approach, and we will then present two computationally workable formalisms describing the electronic properties: the Thomas-Fermi model, simple but valid at very high densities, and the Density Functional Theory, extension of the previous one, much more reliable at intermediate densities.

I The Born-Oppenheimer approximation

Our aim in this section is to properly separate the ionic and electronic contributions to the dynamics. Let us consider a system consisting in a collection of ions and electrons, interacting through a Coulomb potential; this system is described by a Hamiltonian (in atomic units):

$$\hat{\mathcal{H}} = \sum_{\alpha=1}^{N_n} \frac{\mathbf{P}_\alpha^2}{2M_\alpha} + \sum_{\alpha<\beta}^{N_n} \frac{Z_\alpha Z_\beta}{|\mathbf{R}_\alpha - \mathbf{R}_\beta|} + \sum_{i=1}^{N_e} \frac{\mathbf{p}_i^2}{2} + \sum_{i<j}^{N_e} \frac{1}{|\mathbf{r}_i - \mathbf{r}_j|} - \sum_{i,\alpha}^{N_e,N_n} \frac{Z_\alpha}{|\mathbf{R}_\alpha - \mathbf{r}_i|} \tag{3.1}$$

We must refer to the first two terms as the nuclear Hamiltonian $\hat{\mathcal{H}}_n$, and to the last three as the electronic Hamiltonian $\hat{\mathcal{H}}_e$.

The difficulty of treating the ions and the electrons in the same formalism arises in the last term of (3.1), as it couples the electronic and ionic parts of the system. The key point is that the ions are much heavier than the electrons ($M_\alpha \approx 1837$ for hydrogen, the lightest of the ions). In consequence, the time scales associated with the nucleus dynamics are very different; we can then simplify the problem by considering that the electrons react instantly to any change in the nucleus position. This is the so-called Born-Oppenheimer approximation [**?**], also called the adiabatic approximation. In this case, the ions move in an electric potential instantly created by the electrons.

In this picture, the electronic Hamiltonian represents a system of N_e electrons in an electric field created by N_n fixed ions, so that the $\{\mathbf{R}_\alpha\}$ become parameters of $\hat{\mathcal{H}}_e = \hat{\mathcal{H}}_{e\{\mathbf{R}_\alpha\}}$. From the resolution of $\hat{\mathcal{H}}_{e\{\mathbf{R}_\alpha\}}$, one can then obtain the coupling interaction energy between the ions and the electrons, and then the forces exerted by the electronic system on the ions. The microcanonical formalism introduced in chapter 2 is then usable for the collection of ions subject to the effective potential:

$$\sum_{\alpha<\beta}^{N_n} \frac{Z_\alpha Z_\beta}{|\mathbf{R}_\alpha - \mathbf{R}_\beta|} + \epsilon_{\{\mathbf{R}_\alpha\}} \tag{3.2}$$

where

$$\epsilon_{\{\mathbf{R}_\alpha\}} = \langle \Psi_{\{\mathbf{R}_\alpha\}} | H_{e\{\mathbf{R}_\alpha\}} | \Psi_{\{\mathbf{R}_\alpha\}} \rangle \tag{3.3}$$

$|\Psi_{\{\mathbf{R}_\alpha\}}\rangle$ being the wavevector associated with the ground state of $H_{e\{\mathbf{R}_\alpha\}}$.

In the canonical ensemble at temperature $k_B T = 1/\beta$, the statistical effects must be taken into account, but the partition function can be factorized:

$$Z(T,V,N) = \frac{1}{N_e!}\mathrm{Tr}\left[e^{-\beta\hat{\mathcal{H}}_n} e^{-\beta\hat{\mathcal{H}}_{e\{\mathbf{R}_\alpha\}}}\right] \tag{3.4}$$

and, using the classical formulation of the partition function for the ionic part, the partition function may be rewritten $Z(T,V,N) = Z^{kin}Z^{conf}$ as in chapter 2, with a modified configurational part:

$$Z^{conf}(T,V,N) = \frac{1}{V^{N_n}}\int_{\Gamma_{(N_n,V)}} \prod_{\alpha=1}^{N_n} d\mathbf{R}_\alpha e^{-\beta U_n(\{\mathbf{R}_\alpha,\mathbf{P}_\alpha\})}\mathrm{Tr}\left[e^{-\beta\hat{\mathcal{H}}_{e\{\mathbf{R}_\alpha\}}(\{\mathbf{r}_i,\mathbf{p}_i\})}\right] \tag{3.5}$$

with U_n the nuclear pair interaction.

Finally, we can apply the formalism of chapter 2 if we consider the system as the ions screened by the electrons, which react instantaneously to the ions' positions. The core difficulty is now to estimate the screening of the electrons, since the estimation of the trace in (3.5) must include the quantum effects.

II The Thomas-Fermi model

In theory, the resolution of the trace part of (3.5) would imply to solve Schrödinger's equation:

$$\hat{\mathcal{H}}_{e\{\mathbf{R}_\alpha\}}|\Psi_{\{\mathbf{R}_\alpha\}}\rangle = \epsilon_{\{\mathbf{R}_\alpha\}}|\Psi_{\{\mathbf{R}_\alpha\}}\rangle \tag{3.6}$$

with the suitable boundary conditions. Unfortunately, this is not possible for large systems; from a theoretical standpoint, even for something as small as a two-electron system, the solution can only be approximate. In chemistry, the Hartree-Fock methods and its derivative (see, e.g., [**?**]) are currently used, but their efficiency is limited when the electrons number becomes large. In the following sections, we are going to describe another approach, based on the idea that the electronic N-particles system may be described by its local density $n(\mathbf{r})$, and the properties that interest us may be extracted from this description.

The first approach we are going to explain is the one proposed by L. Thomas and E. Fermi in 1927 [**?** **?**]. The space is divided into cubic cells of size l at point $\mathbf{r}$, containing ΔN electrons. If one assumes that the electrons are independent 1/2-spin particles at zero temperature, and that each cell is bounded by an infinite potential well containing the electrons, the states' density is readily obtained:

$$g(\epsilon) = \frac{\pi}{2}\left(\frac{8m_e l^2}{h^2}\right)^{3/2}\epsilon^{1/2} \tag{3.7}$$

where ϵ is the considered energy level, h the Planck constant and m_e the electron mass. The occupation level is the well-known Fermi-Dirac function [**?** **?**], which at zero temperature reduces to:

$$f(\epsilon) = \begin{cases} 1 & \text{if} \quad \epsilon \leq \epsilon_F \\ 0 & \text{if} \quad \epsilon > \epsilon_F \end{cases} \tag{3.8}$$

where ϵ_F denotes the Fermi energy. The total number of electrons in the cell and the

energy ΔE of these electrons are then related to ϵ_F:

$$\Delta N = \int_0^\infty f(\epsilon)g(\epsilon)d\epsilon = \frac{8\pi}{3}\left(\frac{2m_e}{h^2}\right)^{3/2} l^3\epsilon_F^{3/2} \tag{3.9}$$

$$\Delta E = \int_0^\infty \epsilon f(\epsilon)g(\epsilon)d\epsilon = \frac{8\pi}{5}\left(\frac{2m_e}{h^2}\right)^{3/2} l^3\epsilon_F^{5/2} \tag{3.10}$$

Making l go to 0, $\Delta N/l^3$ and $\Delta E/l^3$ reduce respectively to the electronic density $n(\mathbf{r})$ and the energy $\epsilon(\mathbf{r})$. From (3.9) and (3.10), they are directly related by:

$$\epsilon(\mathbf{r}) = C_F\frac{\hbar^2}{m_e}n(\mathbf{r})^{5/3} \tag{3.11}$$

where $C_F = \frac{3}{10}(3\pi^2)^{2/3}$. One can then integrate the energy over the whole system to obtain the energy as a functional of the electronic density:

$$\mathcal{T}[n] = C_F\frac{\hbar^2}{m_e}\int n(\mathbf{r})^{5/3}d\mathbf{r} \tag{3.12}$$

This functional, $\mathcal{T}[n]$, only represents the kinetic energy. This expression can be obtained by taking the well-known total kinetic energy of a perfect Fermi gas and considering that its expression is valid locally.

In the Thomas-Fermi model, this expression of the kinetic energy is added to the interaction energy between the electrons and with the nucleus to obtain the total energy:

$$E[n] = \mathcal{T}[n] + \frac{1}{2}\iint\frac{n(\mathbf{r})n(\mathbf{r}')}{|\mathbf{r}-\mathbf{r}'|}d\mathbf{r}d\mathbf{r}' - \int\sum_{\alpha=1}^{N_n}\frac{Z_\alpha n(\mathbf{r})}{|\mathbf{R}_\alpha-\mathbf{r}|}d\mathbf{r} \tag{3.13}$$

This expression of the energy of the electronic fluid is interesting since it is only a functional of the electronic density. This way, the ground state may be determined by a variational principle with the constraint on the number of electrons:

$$\delta\left\{E[n] - \mu\left(\int n(\mathbf{r})d\mathbf{r} - N_e\right)\right\} = 0 \tag{3.14}$$

In this last equation, μ is a Lagrange multiplier which can be evaluated as:

$$\mu = \frac{\delta E}{\delta n(\mathbf{r})} = \frac{5}{3}C_F n(\mathbf{r})^{2/3} + \int\frac{n(\mathbf{r}')}{|\mathbf{r}-\mathbf{r}'|}d\mathbf{r}' - \sum_{\alpha=1}^{N_n}\frac{Z_\alpha}{|\mathbf{R}_\alpha-\mathbf{r}|} \tag{3.15}$$

If we write $v(\mathbf{r}) = -\sum_{\alpha=1}^{N_n}\frac{Z_\alpha}{|\mathbf{R}_\alpha-\mathbf{r}|}$ the nucleus potential, the variational principle can be rewritten:

$$\int\delta n(\mathbf{r})\left[v(\mathbf{r}) + \int\frac{n(\mathbf{r})n(\mathbf{r}')}{|\mathbf{r}-\mathbf{r}'|}d\mathbf{r}d\mathbf{r}' + \frac{\delta\mathcal{T}}{\delta n(\mathbf{r})}\right]d\mathbf{r} = 0 \tag{3.16}$$

This leads to a numerically self consistent procedure: starting from a trial density, one can minimize the energy functional with the constraint $N_e = \int n(\mathbf{r})d\mathbf{r}$.

It is important to note that this is sufficient to solve our problem, since it allows us to calculate the forces exerted by the electrons on the nucleus. On the other hand, this model seems to be a strong approximation of the system, so we are going to discuss its domain of validity.

The core approximation lies in the expression of the kinetic energy as a functional of the density. We will spend more time on this idea when we get to the density

functional theory, but for the time being, it is important to notice what this choice implies. In this case, the chosen functional is the same as the perfect electron gas; it contains the corresponding exchange effects, but the kinetic energy also contains correlation effects in the quantum formalism. As a consequence, the Thomas-Fermi approximation is valid when the electrons behave more like a perfect gas. From (3.12), the specific kinetic energy grows as $n^{2/3}$, while, from crude dimensional analysis, we can show that the specific interaction energy of the electronic gas grows as $1/a_e \sim n^{1/3}$, with a_e the Wigner-Seitz radius. Finally,

$$\frac{E_{coul}}{E_{kin}} \sim n^{-1/3} \tag{3.17}$$

so that the denser the gas, the closer it gets from the ideal gas limit. This behavior, counter-intuitive for a classical gas, arises directly from the quantum zero-point energy of the Fermi gas.

In conclusion, the Thomas-Fermi model will be a satisfying approximation at high pressure or high temperature. When the pressure is lower, the expression of the kinetic energy as a density functional is not usable, and it is not even clear that a density functional can represent the kinetic energy. We are going to show that this approach can be generalized.

III Density Functional Theory

We are going to show how the idea of the Thomas-Fermi model can be generalized into a more powerful formalism. Most of this section can be found - with more details - in many reference books, including [**?**]. For French readers, [**?**] also presents a good review.

III.1 Hohenberg-Kohn theorems

Let us start with the zero-temperature electronic system, described by the electronic Hamiltonian:

$$\hat{\mathcal{H}}_e = \sum_{i=1}^{N_e} \frac{\mathbf{p}_i^2}{2} + \sum_{i<j}^{N_e} \frac{1}{|\mathbf{r}_i - \mathbf{r}_j|} - \sum_{i,\alpha}^{N_e,N_n} \frac{Z_\alpha}{|\mathbf{R}_\alpha - \mathbf{r}_i|} \tag{3.18}$$

and the associated eigenvalue equation:

$$\hat{\mathcal{H}}_e|\Psi\rangle = E|\Psi\rangle \tag{3.19}$$

which can be re-written in direct space:

$$\left(\sum_i^{N_e} \frac{\Delta_i}{2} + \sum_i^{N_e} v(\mathbf{r}_i) + \sum_{i<j}^{N_e} \frac{1}{|\mathbf{r}_i - \mathbf{r}_j|} \right) \Psi(\{\mathbf{x}_k\}) = E\Psi(\{\mathbf{x}_k\}) \tag{3.20}$$

where $\mathbf{x} = (\mathbf{r}, s)$ represents the space and spin coordinates, and v any non-electronic potential - typically the Coulomb potential created by the nucleus in (3.18). Let us recall that the difficulty here is that the third term in the Hamiltonian couples the electrons, and the fermionic nature of the electrons impose the wavefunction Ψ to be antisymmetric. If the system is in its ground-state of energy E, it can be written as:

$$E = \frac{\langle\Psi|\hat{\mathcal{H}}_e|\Psi\rangle}{\langle\Psi|\Psi\rangle} = \mathcal{T} + V + U \tag{3.21}$$

where each contribution arises from one of the operators in $\hat{\mathcal{H}}_e$:

$$\mathcal{T} = \frac{1}{2}\int \Psi^*(\{\mathbf{x}_k\}) \sum_i^{N_e} \Delta_i \Psi(\{\mathbf{x}_k\}) d\mathbf{x}^{N_e} \tag{3.22}$$

$$V = \int \Psi^*(\{\mathbf{x}_k\}) \sum_i^{N_e} v(\mathbf{r}_i) \Psi(\{\mathbf{x}_k\}) d\mathbf{x}^{N_e} \tag{3.23}$$

$$U = \int \Psi^*(\{\mathbf{x}_k\}) \sum_{i<j}^{N_e} \frac{1}{|\mathbf{r}_i - \mathbf{r}_j|} \Psi(\{\mathbf{x}_k\}) d\mathbf{x}^{N_e} \tag{3.24}$$

Let us also define the electronic density as:

$$n(\mathbf{r}) = Ne \int |\Psi|^2(\mathbf{r}, s_1, \mathbf{x}_2, \ldots \mathbf{x}_{N_e}) ds_1 d\mathbf{x}_2 \ldots d\mathbf{x}_{N_e} \tag{3.25}$$

The original article by Hohenberg and Kohn in 1964 [**?**] showed two fundamental theorems:

1. *There is a one-to-one relationship between the potential $v(\mathbf{r})$ - up to an additive constant - and the electron density $n(\mathbf{r})$.*
   The trivial part is that v defines the Hamiltonian, and hence the wavefunction Ψ and the density $n(\mathbf{r})$. The interesting part is that v is also uniquely determined by $n(\mathbf{r})$, and thus Ψ and the total energy are also functionals of n.
   Let us show it by supposing two potentials v and v', associated with different ground-states E, Ψ and E', Ψ', but with the same density n. Supposing that the ground-states are not degenerated:

$$E' = \langle \Psi' | \hat{\mathcal{H}}' | \Psi' \rangle < \langle \Psi | \hat{\mathcal{H}}' | \Psi \rangle = \langle \Psi | \hat{\mathcal{H}} + V' - V | \Psi \rangle$$
$$\Rightarrow E' < E + \int [v'(\mathbf{r}) - v(\mathbf{r})] n(\mathbf{r}) d\mathbf{r} \tag{3.26}$$

   The same reasoning applies if one interverts the primed and non-primed quantities, leading by summation to:

$$E' + E < E + E' \tag{3.27}$$

   This contradiction implies that different v lead to different n, and then prooves that n fixes v, and the total energy. We mention here that an extension to degenerated states exists, see e.g. [**? ? ? ?**].
   We have shown that the total ground-state energy is defined by n, so that E can be written as a functional of n, which was our aim:

$$E[n] = \int v(\mathbf{r}) n(\mathbf{r}) d\mathbf{r} + F[n] \tag{3.28}$$

   The functional F represents the kinetic and electronic potential contributions, so that its mathematical form is independent of v; as a consequence, it is called a universal functional. Of course, this mathematical expression is not easy to find, and we will discuss this problem later.

2. *The groundstate energy can be obtained variationally: the density that minimises the total energy under the constraint $\int n(\mathbf{r}) d\mathbf{r} = N_e$ is the exact groundstate density.*

In other words, let us consider a potential v and an associated functional $E_v[n] = \int v(\mathbf{r})n(\mathbf{r})d\mathbf{r} + F[n]$; it is straightforward that, for the correct $n(\mathbf{r})$, E_v equals the ground-state energy E. What this theorem states - and what we are going to proove - is that this correct density is also the one that minimizes E_v.
Let us consider the ground-state eigenfunction $|\Psi_{gs}\rangle$ associated with $n_{gs}(\mathbf{r})$; by definition $E_v[n_v]$ is the ground-state energy associated with v, and is written:

$$E_v[n_{gs}] = \langle\Psi_{gs}|\hat{\mathcal{H}}_e|\Psi_{gs}\rangle \tag{3.29}$$

If we take another wavefunction $|\Psi'\rangle$, we have shown that it is necessarily associated with a different density $n' \neq n_{gs}$; and, by definition of the ground-state:

$$\langle\Psi_{gs}|\hat{\mathcal{H}}_e|\Psi_{gs}\rangle < \langle\Psi'|\hat{\mathcal{H}}_e|\Psi'\rangle \Rightarrow E_v[n_{gs}] < E_v[n'] \tag{3.30}$$

which proves the theorem.

With these theorems, one can find the correct ground-state density by minimizing the correct functional. These theorems allows us to find the ground-state properties of the system without finding the complete antisymmetric wavefunction Ψ, which is a way more difficult task. The problem we still have at this point is to define a correct mathematical representation of F, especially the kinetic part which, as shown in (3.22), is not simply defined in terms of the density.

III.2 The Kohn-Sham formulation

Kohn and Sham suggested in 1965 [**?**] to use an auxiliary system of fictitious independent electrons. Let us rewrite (3.24) using the antisymmetry of the wavefunction:

$$U = \frac{N_e(N_e-1)}{2}\int\frac{1}{|\mathbf{r}-\mathbf{r}'|}d\mathbf{r}d\mathbf{r}'\int|\Psi|^2(\mathbf{r},s_1,\mathbf{r}',s_2,\mathbf{x}_3\ldots\mathbf{x}_{N_e})ds_1ds_2d\mathbf{x}_3\ldots d\mathbf{x}_{N_e} \tag{3.31}$$

and introduce the pair density function:

$$n_2(\mathbf{r}_1,\mathbf{r}_2) = \frac{N_e(N_e-1)}{2}\int|\Psi|^2(\mathbf{r}_1,s_1,\mathbf{r}_2,s_2,\mathbf{x}_3\ldots\mathbf{x}_{N_e})ds_1ds_2d\mathbf{x}_3\ldots d\mathbf{x}_{N_e} \tag{3.32}$$

as in [**?**], it can be expressed with the density function:

$$n_2(\mathbf{r}_1,\mathbf{r}_2) = \frac{1}{2}n(\mathbf{r}_1)n(\mathbf{r}_2)[1+h(\mathbf{r}_1,\mathbf{r}_2)] \tag{3.33}$$

h being the pair-correlation function. One can then express U as:

$$U = \frac{1}{2}\iint\frac{n(\mathbf{r})n(\mathbf{r}')}{|\mathbf{r}-\mathbf{r}'|}d\mathbf{r}d\mathbf{r}' + \frac{1}{2}\iint\frac{n(\mathbf{r})n(\mathbf{r}')h(\mathbf{r},\mathbf{r}')}{|\mathbf{r}-\mathbf{r}'|}d\mathbf{r}d\mathbf{r}' \tag{3.34}$$

and, consequently rewrite the total energy functional:

$$E[n] = \int v(\mathbf{r})n(\mathbf{r})d\mathbf{r} + \frac{1}{2}\iint\frac{n(\mathbf{r})n(\mathbf{r}')}{|\mathbf{r}-\mathbf{r}'|}d\mathbf{r}d\mathbf{r}' + G[n] \tag{3.35}$$

Here, G is a functional that contains the kinetic, correlation and quantum effects, and which embodies all the difficulty.

Kohn and Sham's idea is to separate G into two parts:

$$G[n] = \mathcal{T}_s[n] + E_{xc}[n] \tag{3.36}$$

where $\mathcal{T}_s[n]$ is the known kinetic energy of a system of non-interacting electrons at density $n(\mathbf{r})$. E_{xc} contains all the exchange and correlation effects, plus the difference between the kinetic energy of an interacting and a non-interacting electronic system; it is once again the part which is not trivially known. A discussion about its mathematical form will be given in the next section; for now, we are going to assume that it exists.

The variational principle may now be used on the functional (3.35):

$$\int \delta n(\mathbf{r}) \left[\varphi(\mathbf{r}) + \frac{\delta \mathcal{T}_s}{\delta n(\mathbf{r})} + v_{xc}(\mathbf{r}) \right] d\mathbf{r} = 0 \tag{3.37}$$

$$\text{with} \quad \varphi(\mathbf{r}) = v(\mathbf{r}) + \int \frac{n(\mathbf{r}')}{|\mathbf{r} - \mathbf{r}'|} d\mathbf{r}' \tag{3.38}$$

$$\text{and} \quad v_{xc} = \frac{\delta E_{xc}}{\delta n(\mathbf{r})} \tag{3.39}$$

This formulation can be compared with the Thomas-Fermi formulation (3.16): this system is the same as a Thomas-Fermi one submitted to an effective potential $v_{eff}(\mathbf{r}) = v(\mathbf{r}) + v_{xc}(\mathbf{r})$. Following Kohn and Sham, we can introduce a set of N_e independent orbitals (the so-called Kohn-Sham orbital) satisfying the equations:

$$\begin{cases} \left(-\frac{1}{2}\Delta + v_{eff}(\mathbf{r}) \right) \psi_i(\mathbf{r}) = \epsilon_i \psi_i(\mathbf{r}) \\ v_{eff}(\mathbf{r}) = v(\mathbf{r}) + \int \frac{n(\mathbf{r}')}{|\mathbf{r} - \mathbf{r}'|} d\mathbf{r}' + v_{xc}(\mathbf{r}) \\ n(\mathbf{r}) = \sum_i^{N_e} |\psi_i(\mathbf{r})|^2 \end{cases} \tag{3.40}$$

These equations may be solved by a self-consistent procedure: starting from a trial density, the effective potential is fixed, the orbitals computed and the density recomputed, until the density is stable from one iteration to the following one. Once the set of Kohn-Sham orbitals is converged, the energy of the ground-state level can be easily computed with $\mathcal{T}_s[n] = \sum_{i=1}^{N_e} \langle \psi_i | -\frac{1}{2}\Delta | \psi_i \rangle$ and the explicit functionals of the density.

The following figure - taken from [**?**] - sums up the combination of the Hohenberg-Kohn theorems and the Kohn-Sham formulation: Hohenberg and Kohn (HK) ensure

$$\begin{array}{ccccccc} v(\mathbf{r}) & \overset{HK}{\Longleftarrow} & n_0(\mathbf{r}) & \overset{KS}{\Longleftrightarrow} & n_0(\mathbf{r}) & \overset{HK}{\Longrightarrow} & v_{eff}(\mathbf{r}) \\ \Downarrow & & \Uparrow & & \Uparrow & & \Downarrow \\ \Psi(\mathbf{r}^{N_e}) & \Longrightarrow & \Psi_0(\mathbf{r}^{N_e}) & & \psi_{i=1,N_e}(\mathbf{r}) & \Longleftarrow & \psi_i(\mathbf{r}) \end{array}$$

both the uniqueness of the density n_0 associated with any potential (v or v_{eff}). The

Kohn-Sham (KS) approach links the real system - associated with v - to a fictitious system - associated with v_{eff} - whose ground-state has the same density.
This equivalent system permits a decoupling of the N_e-electrons equations and leads to a usable expression for the kinetic energy. Assuming an expression for the exchange-correlation functional, the system is not numerically solvable. We are now going to tackle this last issue.

III.3 Mathematical representations of the exchange-correlation functional

In the previous sections, we have shown that we can compute all the properties of the electronic system by minimization of a certain functional. The definition of this functional is a key problem, and we have progressively isolated the quantum effects into the so-called exchange-correlation part. We will now endeavour to give a mathematical representation for this functional. It must be stressed out that, if the theory has been an exact computation so far, these exchange-correlation effects cannot be computed analytically and will introduce approximations. More precisely, we re going to present two possible parametrizations of this functional, the so-called LDA and GGA functionals.

The first idea is to construct a functional with the assumption that the electronic density is nearly homogeneous: the functional will only use the local density as a variable, neglecting by definition the possible gradient contributions. This approach is called the *Local Density Approximation*, or LDA. If we write $n^\uparrow$ and $n^\downarrow$ the densities associated with up and down spin states, we can write:

$$E_{xc}^{LDA}[n] = \int n(\mathbf{r})\epsilon_{xc}^{hom}(n^\uparrow(\mathbf{r}), n^\downarrow(\mathbf{r}))d\mathbf{r} \tag{3.41}$$

where ϵ_{xc}^{hom} is the energy of an homogeneous electron gas at density $n^\uparrow, n^\downarrow$.
In the case of the non-polarized homogeneous electron gas, the exchange and correlation parts may be separated, and the exchange contribution computed analytically [**?**]:

$$\epsilon_x^{hom}(n_0) = -\frac{3}{4}\left(\frac{3}{\pi}\right)^{1/3} n_0^{1/3} \tag{3.42}$$

The correlation contribution is not as easy to pull out, and must be estimated numerically. Monte-Carlo schemes [**?**] led to a good numerical knowledge of this energy, and Perdew and Yang proposed in 1992 an analytic parametrization of this functional which is now widely used - the so-called PW correlation functional. We do not give the details of the - complex - parametrization here, but the reader can refer to the original paper [**?**]. Once it is given, we can deduce the potential from (3.39):

$$v_{xc}^{LDA}(\mathbf{r}) = \frac{\delta E_{xc}^{LDA}}{\delta n(\mathbf{r})} = \left[\epsilon_{xc}^{hom} + n\frac{\partial \epsilon_{xc}^{hom}}{\partial n}\right]_{\mathbf{r}} \tag{3.43}$$

If the LDA has shown some good results for some metallic properties such as bulk modulus or lattice constants, in some situations - especially in the case of dense plasmas - we must correctly model the immediate neighbourhood of the nucleus, where the potential as well as the electronic density vary quickly. In this case, a description

taking the gradients into account is better, and is called *Generalized-Gradient Approximation* (GGA). The functional is constructed as:

$$\begin{aligned} E_{xc}^{GGA}[n] &= \int n(\mathbf{r})\epsilon_{xc}(n^{\uparrow}(\mathbf{r}), n^{\downarrow}(\mathbf{r}), |\nabla n^{\uparrow}(\mathbf{r})|, |\nabla n^{\downarrow}(\mathbf{r})|, \dots)d\mathbf{r} \\ &= \int n(\mathbf{r})\epsilon_x^{hom}(n) f_{xc}(n^{\uparrow}(\mathbf{r}), n^{\downarrow}(\mathbf{r}), |\nabla n^{\uparrow}(\mathbf{r})|, |\nabla n^{\downarrow}(\mathbf{r})|, \dots)d\mathbf{r} \end{aligned} \tag{3.44}$$

In this case, f_{xc} is dimensionless and has still to be parametrized. One of the most widely used parametrizations was given by Perdew, Burke and Ernzerhof in 1996 and is called the PBE parametrization [**?**]. This is the parametrization that we used in our work. The equation (3.39) now leads to:

$$v_{xc}^{GGA}(\mathbf{r}) = \frac{\delta E_{xc}^{GGA}}{\delta n(\mathbf{r})} = \left[\epsilon_{xc} + n\frac{\partial \epsilon_{xc}}{\partial n} - \nabla \cdot \left(n\frac{\partial \epsilon_{xc}}{\partial \nabla n}\right)\right]_{\mathbf{r}} \tag{3.45}$$

III.4 Finite-temperature DFT

In the previous sections, we have only considered finding the ground-state properties of the system. If the thermal energy $k_B T$ is small compared to the typical energies of the equivalent Kohn-Sham system, this may be a sufficient approximation, but this is no always the case. In this section, we are going to discuss the extension of the theory to finite-temperature.

In the case of finite-temperature systems, the suitable ensemble describing a quantum system is the grand-canonical ensemble. The energy levels are excited following a Thomas-Fermi distribution, and we try to find the grand potential - function of the temperature and chemical potential μ:

$$\Xi(T, \mu, V) = \frac{1}{N!}\mathrm{Tr}\left[e^{-\beta(\hat{\mathcal{H}}_{e\{\mathbf{R}_\alpha\}} - \mu N)}\right] \tag{3.46}$$

and the quantity which plays an equivalent role with the energy in the ground-state case is the grand potential:

$$\Omega(T, \mu, V) = -k_B T \ln \Xi(T, \mu, V) \tag{3.47}$$

In a 1965 paper [**?**], Mermin used arguments similar to those of Hohenberg and Kohn, and showed that the grand potential is a functional of the density:

$$\Omega[n] = \int n(\mathbf{r})(v(\mathbf{r}) - \mu)d\mathbf{r} + \frac{1}{2}\iint \frac{n(\mathbf{r})n(\mathbf{r}')}{|\mathbf{r} - \mathbf{r}'|}d\mathbf{r}d\mathbf{r}' + F[n] \tag{3.48}$$

with $F[n]$ a functional containing both kinetic, exchange-correlation and entropic effects. Following the Kohn Sham formulation, it can be written:

$$F[n] = \mathcal{T}_s[n] - TS_s[n] + F_{xc}[n] \tag{3.49}$$

with $\mathcal{T}_s$ and S_s being respectively the kinetic energy and entropy of the ideal electron gas, and F_{xc} being the free energy of exchange-correlation, once again the core difficulty. The minimization may be undertaken as previously, leading to:

$$\begin{cases} \left(-\frac{1}{2}\Delta + v_{eff}(\mathbf{r})\right)\psi_i(\mathbf{r}) = \epsilon_i \psi_i(r) \\ v_{eff}(\mathbf{r}) = v(\mathbf{r}) + \int \frac{n(\mathbf{r}')}{|\mathbf{r} - \mathbf{r}'|}d\mathbf{r}' + v_{xc}(\mathbf{r}) \\ n(\mathbf{r}) = \sum_i^{\infty} f_i |\psi_i(\mathbf{r})|^2 \end{cases} \tag{3.50}$$

Although this system is very similar to (3.40), two major differences must be underlined:

- the exchange-correlation potential is now defined as

$$v_{xc}(\mathbf{r}) = \frac{\delta F_{xc}}{\delta n(\mathbf{r})} \tag{3.51}$$

- the density is now implying an infinite sum over the possible orbitals weighted by the Fermi-Dirac factor

$$f_i = \frac{1}{1 + e^{\beta(\epsilon_i - \mu)}} \tag{3.52}$$

  The infinite sum may seem numerically unreachable, yet in practical calculations there is always an energy level starting from which the orbitals show a zero weight, and the sum can be truncated from this level.

Since the orbitals allow us to compute the ideal gas parts:

$$\mathcal{T}_s = \sum_i^{\infty} f_i \langle \psi_i | -\frac{1}{2}\Delta | \psi_i \rangle \tag{3.53}$$

$$\text{and} S_s = -k_B \sum_i^{\infty} [f_i \ln f_i + (1 - f_i)\ln(1 - f_i)] \tag{3.54}$$

We can then use the explicit functionals in (3.48) and the previous equations to compute Ω once the density is found.

It may seem that F_{xc} cannot be chosen the same way as the previous E_{xc}, since this last functional does not include the entropic contribution. Some functionals which take into account these contributions have been proposed, e.g. by F. Perrot and M. Dharma-Wardana in 1984 [**?**]. In practical uses, however, the GGA-PBE functional leads to remarkably correct results even at finite temperature, and it is the one we will use in our work.

IV Numerical use of the DFT

IV.1 Numerical procedure

The fastest way to compute the correct ground-state or grand potential density is to use a self-consistent procedure. The idea is to compute v_{eff} from a trial density $n(\mathbf{r})$, and to solve the Kohn-Sham system to find a new density; the loop is repeated until $n(\mathbf{r})$ does not change from one iteration to the next. The whole procedure is illustrated on Figure (3.1).

In the ABINIT package [**?** **?**], the criterion for stopping the convergence may be more complex than just a criterion on the density: for example, the user can impose the loop to continue until the forces derived from the density, or their gradients, are converged.

IV.2 Solving the Kohn-Sham equation into the reciprocal space

Let us now consider in more details how the Kohn-Sham equations may be solved. The complicated one is, of course,

$$\left(-\frac{1}{2}\Delta + v_{eff}(\mathbf{r})\right)\psi_i(\mathbf{r}) = \epsilon_i \psi_i(\mathbf{r}) \tag{3.55}$$

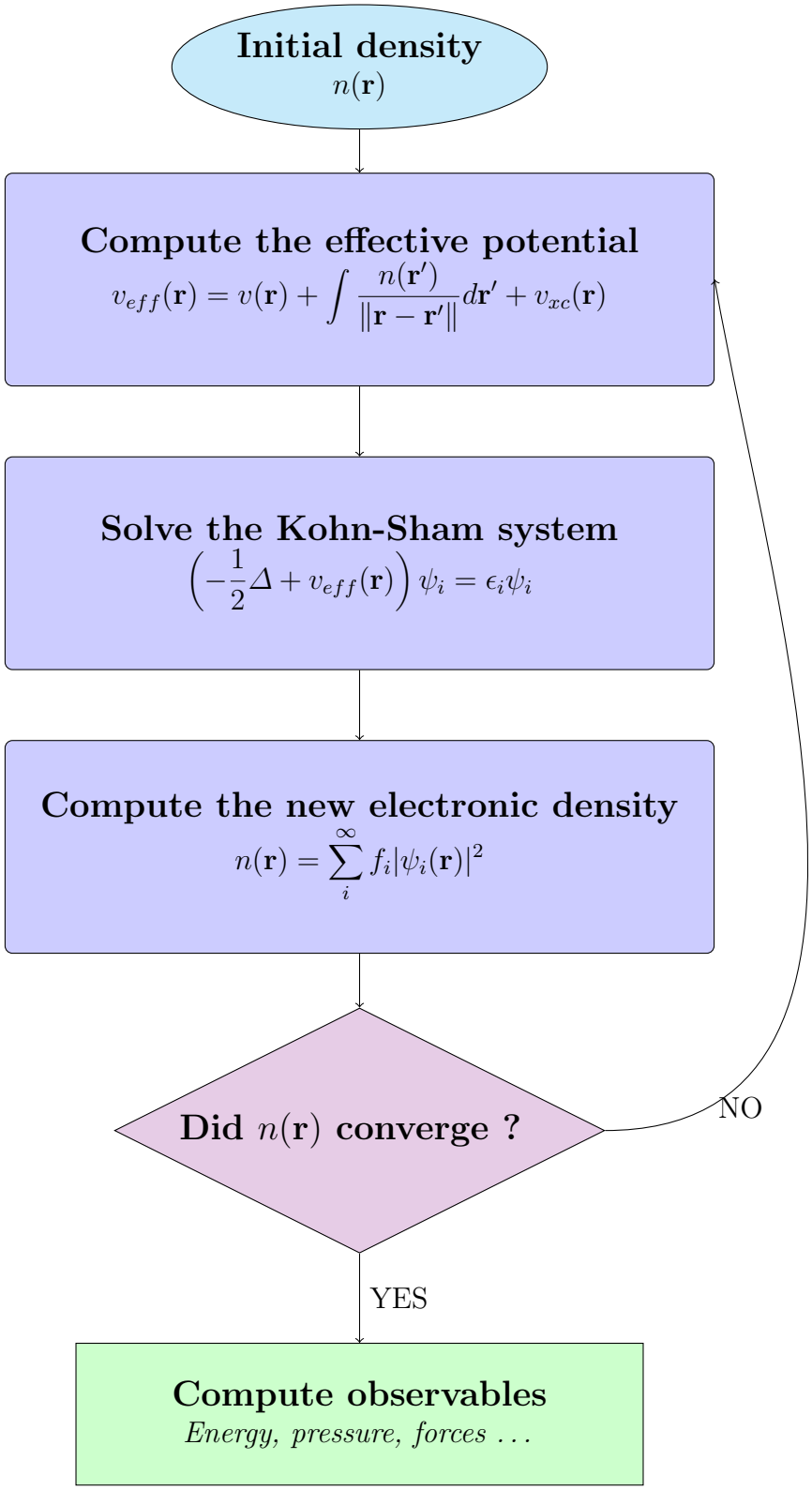

Figure 3.1: Numerical procedure used to find the electronic density for a given position of the nucleus, and hence a given $v(\mathbf{r})$. The loop is repeated until the density has converged to a given convergence parameter, and then the output quantities are computed.

Since it is an eigenvalues equation, it introduces a question we have left aside up to now: such a problem needs specified boundary conditions in order to be correctly formulated.

The question of the boundary conditions is central, but our choice will be guided by a practical limitation: while a crystal naturally leads to periodic boundaries, simulating a macroscopic liquid system is out of reach, even with modern computers. In typical DFT simulations, we will limit our systems to a few hundred ions in order to keep the computing time reasonable. The solution for computing macroscopic quantities is to artificially extend such a small system by fixing periodic boundary conditions. The simulated volume is only the primitive cell, or the so-called supercell. The influence of the periodic replicas of the ions are taken into account with various methods, one of which is detailed in Appendix A, and the electronic Kohn-Sham orbitals have periodic boundaries imposed. Of course, the specific properties of the system are expected not to depend on the choice of the boundary conditions. Finally, simulating a solid with such a replication method seems to be trivially correct, and we expect it to be sufficiently representative for liquid simulations if the supercell is large enough.

Since we have imposed this periodicity, we can use the Bloch theorem [**?**] to write the eigenfunctions ψ_i as the product of a wavelike part and a periodic part [**?**]:

$$\psi_i^{\mathbf{k}}(\mathbf{r}) = e^{i\mathbf{k}\cdot\mathbf{r}}\phi_i(\mathbf{r}) \tag{3.56}$$

The ϕ_i function shows the same periodicity as the primitive cell. If we write $\mathbf{G}$ the reciprocal lattice vectors - defined by the condition $\mathbf{G}\cdot\mathbf{l} = 2\pi m, m \in \mathbb{N}$ with $\mathbf{l}$ a vector of the Bravais lattice - we can expand ϕ_i as a set of plane waves:

$$\phi_i(\mathbf{r}) = \sum_{\mathbf{G}} c_{i,\mathbf{G}} e^{i\mathbf{G}\cdot\mathbf{r}} \tag{3.57}$$

Combining (3.56) and (3.57), and limiting the choice of the $\mathbf{k}$ points to the first Brillouin zone [**?**], the Kohn-Sham orbitals can be rewritten:

$$\psi_i^{\mathbf{k}}(\mathbf{r}) = \sum_{\mathbf{G}} c_{i,\mathbf{k}+\mathbf{G}} e^{i(\mathbf{k}+\mathbf{G})\cdot\mathbf{r}} \tag{3.58}$$

Finally, one can insert this equation into the Kohn-Sham equation (3.55) and integrate over $\mathbf{r}$ to find the reciprocal space formulation of this equation:

$$\sum_{\mathbf{G}'} \left[-\frac{1}{2}|\mathbf{k}+\mathbf{G}|^2 \delta_{\mathbf{G},\mathbf{G}'} + \hat{v}_{eff}(\mathbf{G}-\mathbf{G}') \right] c_{i,\mathbf{k}+\mathbf{G}'} = \epsilon_i c_{i,\mathbf{k}+\mathbf{G}} \tag{3.59}$$

where $\delta_{a,b}$ is the Kronecker symbol and $\hat{v}_{eff}$ is the Fourier transform of v_{eff}. Finally, solving this equation is a matrix inversion for each $\mathbf{k}$ point, the matrix having the number of $\mathbf{G}$ points elements.

The infinite number of electrons in the solid (taking the periodicity into account) should be accounted for with an infinite number of $\mathbf{k}$ points, defined along a discrete grid. For each $\mathbf{k}$ point, we are supposed to solve the whole set of orbitals $\psi_i^{\mathbf{k}}$, or at least a set large enough to account for all occupied states. However, the orbitals at two close $\mathbf{k}$ points will be very similar, and it is possible to limit ourselves to a single $\mathbf{k}$ point wavefunction to represent all the wave functions around this point in $\mathbf{k}$ space. Some optimal $\mathbf{k}$ points grids have been designed, such as the widely used Monkhorst and Pack grid [**?**]. Of course, it is necessary to test numerically the convergence of the thermodynamic quantities with respect to the number of $\mathbf{k}$ points; in the case of dense plasma physics, a computation at the unique $\Gamma = (0,0,0)$ point is generally sufficient

to have a convergence better than 2%. If it may seem a big error, we have to recall that the errors implied in the choice of the functional are often around 5%, and cannot be as well controlled as this convergence problem.

On the other hand, each $\mathbf{k}$ point still implies an infinite sum over the reciprocal lattice vectors $\mathbf{G}$, or equivalently the inversion of an infinite matrix. However, the cœfficients $c_{i,\mathbf{k}+\mathbf{G}}$ associated with lower kinetic energies $\frac{1}{2}|\mathbf{k}+\mathbf{G}|^2$ are generally the larger ones, implying that the large $\mathbf{G}$ will not contribute substantially to the orbital and that the sum can be truncated. In practice, numerical codes introduce a cutoff energy which will control the summation: we only keep the $\mathbf{G}$ vectors which satisfy $\frac{1}{2}|\mathbf{k}+\mathbf{G}|^2 < E_{cut}$. The E_{cut} energy is then another convergence parameter that must be checked, and is generally the most critical one. As this is a Fourier representation, one can intuitively understand that the regions where the density or the potential vary rapidly are the ones that will impose a lower bound on E_{cut}. These regions are obviously the ones around the nucleus, because of the rapid variation of the Coulomb potential around zero. We are going to show in the next section that there is a method to replace the nucleus potential with a smoother one in order to decrease E_{cut}.

IV.3 Replacing the ions with pseudo-potentials

As we stated before, the potential around the nucleus tends towards infinity, and quantum mechanics show that the deeper the potential well, the higher the frequency of the wavefunction. On the other hand, the electrons near the nucleus are close to the isolated atom wave function for a solid at normal density. These wave functions are rapidly varying, implying a large $\mathbf{k}$ points base. Many solutions have been attempted to replace the real Coulomb potential with an effective, smoother pseudo-potential around each ion. The key difficulty is to create a pseudo-potential which can be used in many contexts (single atom, molecule, crystals, plasmas...). Among the possible methods, we can cite the *othogonalized plane wave* [**?** **?** **?**] or the norm-conserving pseudo-potentials [**?**]. Each of these methods is briefly reviewed and discussed in [**?**]. We are going to present an efficient method with no loss of information: the *Projector augmented wave* (PAW).

The PAW formalism

This methods was developped by P. Blöchl in 1994 [**?** **?** **?**]. We are going to construct the transformation from the real Kohn-Sham orbitals to less stiff pseudized orbitals. Let us denote $|\psi_n\rangle$ a Kohn-Sham orbital - the subscript n containing both the $\mathbf{k}$ point, the spin state and other relevant quantum numbers - and $|\tilde{\psi}_n\rangle$ the corresponding pseudized wavefunction. They are related by a transformation $\mathcal{P}$:

$$|\psi_n\rangle = \mathcal{P}|\tilde{\psi}_n\rangle \tag{3.60}$$

First of all, the Kohn-Sham equations are modified into :

$$\mathcal{P}^\dagger \hat{\mathcal{H}}_{KS} \mathcal{P}|\tilde{\psi}_n\rangle = \epsilon_n \mathcal{P}^\dagger \mathcal{P}|\tilde{\psi}_n\rangle \tag{3.61}$$

Let us now define $\mathcal{P}$. Since the wavefunction oscillates near the nucleus, we can define a set of auxiliary operators $\mathcal{P}_{\mathbf{R}_\alpha}$, which are non-null only inside a $S_{\mathbf{R}_\alpha}$ sphere centered around the nucleus at $\mathbf{R}_\alpha$ and with a radius r_{PAW}. The complete transformation $\mathcal{P}$ is then expressed as:

$$\mathcal{P} = \mathbb{I} + \sum_{\alpha=1}^{N_n} \mathcal{P}_{\mathbf{R}_\alpha} \tag{3.62}$$

$\mathbb{I}$ being the identity operator. Supposing the radius r_{PAW} short enough to avoid any intersection between the $S_{\mathbf{R}_\alpha}$ spheres, we just have to define $\mathcal{P}_{\mathbf{R}_\alpha}$ for one ion.

Let us consider one fixed ion α and project $|\psi_n\rangle$ and $|\tilde{\psi}_n\rangle$ over two wavefunctions bases:

$$|\psi_n\rangle = \sum_\nu c^\alpha_{n,\nu}|\phi^\alpha_\nu\rangle \quad \text{and} \quad |\tilde{\psi}_n\rangle \sum_\nu \tilde{c}^\alpha_{n,\nu}|\tilde{\phi}^\alpha_\nu\rangle \tag{3.63}$$

The $\{|\phi^\alpha_\nu\rangle\}$ basis is naturally chosen to be the solutions of Schrödinger's equation of the isolated atom α. The $\{|\tilde{\phi}^\alpha_\nu\rangle\}$ can be chosen more freely inside the $S_{\mathbf{R}_\alpha}$ sphere, but we impose the equality of each basis function outside the sphere:

$$\phi^\alpha_\nu(\mathbf{r}-\mathbf{R}_\alpha) = \tilde{\phi}^\alpha_\nu(\mathbf{r}-\mathbf{R}_\alpha) \quad \text{if} \quad |\mathbf{r}-\mathbf{R}_\alpha| > r_{PAW} \tag{3.64}$$

Once these bases are chosen, the local transformation is defined:

$$|\phi^\alpha_\nu\rangle = (\mathbb{I}+\mathcal{P}_\alpha)|\tilde{\phi}^\alpha_\nu\rangle \tag{3.65}$$

$$\mathcal{P}_\alpha|\tilde{\phi}^\alpha_\nu\rangle = |\phi^\alpha_\nu\rangle - |\tilde{\phi}^\alpha_\nu\rangle \tag{3.66}$$

and so, $\mathcal{P}$ if completely defined by the choice of the $\{|\tilde{\phi}^\alpha_\nu\rangle\}$ basis.

Let us specify more constraints on the choice of the $\{|\tilde{\phi}^\alpha_\nu\rangle\}$. We can see from (3.64), (3.65) and the fact that the spheres do not overlap that:

$$|\phi^\alpha_\nu\rangle = \mathcal{P}|\tilde{\phi}^\alpha_\nu\rangle \tag{3.67}$$

and consequently, inside the sphere $S_{\mathbf{R}_\alpha}$:

$$|\psi_n\rangle = \mathcal{P}|\tilde{\psi}_n\rangle = \sum_\nu \tilde{c}^\alpha_{n,\nu}\mathcal{P}|\tilde{\phi}^\alpha_\nu\rangle = \sum_\nu \tilde{c}^\alpha_{n,\nu}|\phi^\alpha_\nu\rangle \tag{3.68}$$

Since the projection on a basis is unique, we get $\tilde{c}^\alpha_{n,\nu} = c^\alpha_{n,\nu}$; in other words, $|\psi_n\rangle$ and $|\tilde{\psi}_n\rangle$ have the same spectrum on their respective bases. As we wanted $\mathcal{P}$ to be a linear transformation, this implies finally the existence of a projectors set $\{|\tilde{p}^\alpha_\nu\rangle\}$ such as:

$$c^\alpha_{n,\nu} = \langle\tilde{p}^\alpha_\nu|\tilde{\psi}_n\rangle \tag{3.69}$$

These projectors will explicitly define the transformation for the numerical computation. Outside the $S_{\mathbf{R}_\alpha}$ sphere, there is no constraint on the projector and it can be chosen arbitrarily without loss of generality: it is then chosen to be null. The non-overlapping condition also implies that inside the PAW sphere, the decomposition can be rewritten:

$$|\tilde{\psi}_n\rangle = \sum_\nu |\tilde{\phi}^\alpha_\nu\rangle\langle\tilde{p}^\alpha_\nu|\tilde{\psi}_n\rangle \tag{3.70}$$

leading to a closure property:

$$\sum_\nu |\tilde{\psi}^\alpha_\nu\rangle\langle\tilde{p}^\alpha_\nu| = \mathbb{I} \tag{3.71}$$

and an orthonormality property:

$$\langle\tilde{p}^\alpha_\nu|\tilde{\phi}^\alpha_\mu\rangle = \delta_{\nu,\mu} \tag{3.72}$$

These constraints on the projectors are quite light. Blöchl provides in his papers the most general construction possible for the projectors. Finally, we can express the total

transformation as well as the real Kohn-Sham orbitals in terms of the projectors and local bases:

$$\mathcal{P} = \mathbb{I} + \sum_{\alpha=1}^{N_n} \sum_{\nu} \left(|\phi_\nu^\alpha\rangle - |\tilde{\phi}_\nu^\alpha\rangle \right) \langle \tilde{p}_\nu^\alpha | \tag{3.73}$$

$$\psi_n(\mathbf{r}) = \tilde{\psi}_n(\mathbf{r}) + \left(|\phi_\nu^\alpha\rangle - |\tilde{\phi}_\nu^\alpha\rangle \right) \langle \tilde{p}_\nu^\alpha | \tilde{\psi}_n \rangle \tag{3.74}$$

$\tilde{\psi}_n(\mathbf{r})$ being the solution of (3.61).

Since the transformation only depends on the considered ion α and not on the global system, it is possible to define the transformation for each element once and for all. In fact, as the transformation also depends on r_{PAW}, a given pseudo-potential is only usable in a certain density range - the upper limit being set by the condition of non-overlapping PAW spheres.

Let us summarize what the pseudo-potential is for a given element:

- a $\{\phi_\nu^\alpha\}$ basis associated with the Coulomb Hamiltonian of the nucleus; it is generally chosen as the classical atomic orbitals of the considered element
- a $\{\tilde{\phi}_\nu^\alpha\}$ basis of pseudo wavefunctions, designed to be as smooth as possible given the constraint of r_{PAW}
- a $\{\tilde{p}_\nu^\alpha\}$ set of projectors satisfying the closure and orthonormality properties

In this work, we will generate our pseudo-potentials using the ATOMPAW code [**?**]; an example of such generation is given for the 2s orbital of carbon on Figure (3.2).

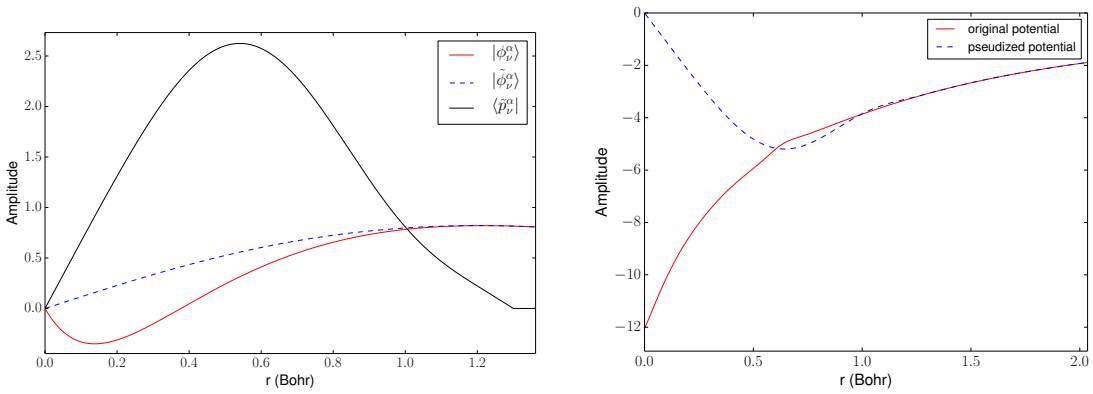

(a) Orbitals and projectors

(b) Original and regularized potentials

Figure 3.2: Regularization of the orbitals and the potential using the PAW method. The pseudized orbital and the regularized potential are clearly smoother than the originals

Let us also say that it is possible to consider the core electrons as fixed in the pseudo-potential if the studied conditions are not dense enough to ionize these orbitals. This frozen-core approximation leads to a reduction of the number of Kohn-Sham orbitals, which is another time gain.

V The Orbital-Free approach

We will end this chapter with a few words about the Orbital-Free approach. This method is mainly based on the Thomas-Fermi theory, since the idea is still to write

down the free energy of the system as a simple functional of the density, and reduce the computing time by avoiding the Kohn-Sham equivalent system. This approach was first used by Pearson and Smargiassi in the early 90s [**?** **?**], and is still used (see, e.g., [**?**]).

The first idea of Thomas and Fermi have been improved by changing the kinetic functional [**?**] or adding exchange-correlation functional [**?** **?**], like in the DFT application. For the same computational reasons, the nuclear potential is regularized with a pseudopotential.

VI Conclusion

We have seen that highly coupled plasmas need advanced simulation techniques in order to correctly take into account the quantum electron motion in a molecular dynamics scheme. The Born-Oppenheimer approximation lets us separate the dynamics of the nucleus - still described by the Newtonian equations - and of the electrons. Although Schrödinger's equation is really not solved, it is possible to compute the electronic density and to extract pressure, energy, and the produced electric field. The basic method is resource-consuming, but many improvements have been designed to reduce the computation time.

The DFT method is successful whenever the quantum nature of the electrons plays a crucial role in the physics of the system. In our work, we are going to apply it to the case of warm dense matter, but it is also widely used in condensed matter physics - for the study of conducting metals, for instance. The only requirement is that the ions can still be correctly described with Newtonian dynamics. When the density of the system is so extreme that this condition is not met, the electronic system behaves as a perfect gas, and it does not embody a numerical difficulty anymore. However, the ions become more difficult to simulate, and we are going to show this in the next chapter.

Part II

Planetary interiors: models and construction of equations of state for “ ices ”

Chapter 4

How to build a planetary interior model

Contents

I The equations of a self-gravitating model 48

I.1 The relevant timescales 48

I.2 A naive approach: one-dimensional models 49

I.3 The theory of planetary figures 51

II A quick overview of existing models for giant planets . . 55

II.1 The basic assumptions of a gaseous planet model 55

II.2 The importance of the equation of state 56

III Conclusion 57

It seems obvious that the ideal - and most direct - way to obtain information on the interior structure of a planet is through seismic studies. However, the only planet for which we have access to reliable seismic data is the Earth. In the absence of such data, our knowledge of planetary interior structure is bound to the elaboration of physically plausible models from which surface data can be extracted and compared to measurements.

In this chapter, we present the basics of a structure theory for self-gravitating objects. The first section can be applied to planets and stars, as well as to other objects, given the correct equation of state (EOS). The second part is dedicated to presenting the currently proposed planetary models. It is important to bear in mind that we only discuss the structure of the planet in this section, not the evolution of the planet with time.

I The equations of a self-gravitating model

I.1 The relevant timescales

What we develop here is a problem of compressible fluid mechanics; it requires to obtain the fields for the density $\rho(\mathbf{r},t)$, the temperature $T(\mathbf{r},t)$, the pressure $P(\mathbf{r},t)$ and the velocity $\mathbf{v}(\mathbf{r},t)$. The relevant equations will intuitively be the conservation of mass, the conservation of momentum, the conservation of energy, the equation of state and the transport cœfficients associated with the material of the object. However, it seems intuitive that a planet or a star presents a mean static structure which evolves "slowly", with "quick" fluctuations that can be neglected. In order to quantify this idea, we will follow [**?**] and define rough timescales for our object.

Let us consider an object with a mean density $\bar{\rho}$, mass M and radius R; its central pressure is roughly given by

$$P_c \simeq \frac{GM}{R^4}, \tag{4.1}$$

where G is the gravitational constant, and the speed of sound can be estimated as

$$c_s \simeq \sqrt{\frac{P_c}{\bar{\rho}}} \simeq \sqrt{\frac{GM}{R}} \tag{4.2}$$

We then define the dynamical timescale as the time for an acoustic wave to propagate through the object:

$$\tau_{dyn} \simeq \frac{R}{c_s} \simeq \sqrt{\frac{R^3}{GM}} \tag{4.3}$$

This dynamic timescale is also called *free fall time*, since it can be obtained as the time of a gravitational collapse if the pressure forces which balance the object are cancelled. For Jupiter or our sun, τ_{dyn} is of approximately half an hour.

The Kelvin-Helmholtz timescale is defined roughly as the time it takes for an object in quasi-static equilibrium to radiate its energy:

$$\tau_{KH} \simeq \frac{E}{L} \tag{4.4}$$

where E is the internal energy and L the luminosity of the object. The Virial theorem (see, e.g., [**?**]) shows in the case of a planet or a star that the internal energy and the

gravitational energy are commensurable, so that we can write:

$$\tau_{KH} \simeq \frac{GM^2}{RL} \tag{4.5}$$

Using the observed value for Jupiter, τ_{KH} is of the order of 10^{11} years. Thus, as expected, the hydrostatic approximation is validated since $\tau_{KH} \gg \tau_{dyn}$, and it is possible to compute only the mean structure with a static theory.

For the sake of completeness, let us present a third timescale, which is relevant only for stars: by definition, a star maintains its equilibrium by balancing the gravitational acceleration with the pressure exerted by nuclear reactions; this leads to the definition of another timescale, the nuclear timescale:

$$\tau_{nucl} \simeq \frac{E_{nucl}}{L} \tag{4.6}$$

Since the nuclear energy budget dominates the gravitational one while a star stays on the main sequence, the nuclear timescale will be way higher than the Kelvin-Helmholtz, leading to further simplifications in star evolution models.

Finally, we will formulate a theory for the quasi-static structure of a planet at a given time, based on the hydrostatic approximation. This immediately sets the - mean - velocity field to zero, and the conservation of mass is only the mass flux nullity.

I.2 A naive approach: one-dimensional models

In first approximation, a planet is spherical, so that we can express the diverse equations as function of the radius only. We write the conservation of momentum as the Navier-Stokes equation:

$$\rho \left(\frac{\partial}{\partial t} + \mathbf{v} \cdot \nabla \right) \mathbf{v} = -\nabla P - \rho \nabla V \tag{4.7}$$

with the nullity of the velocity field and V being the potential of the external forces, which can be rewritten as the sum of the gravitational and others external parts:

$$\frac{dP}{dr} = -\rho \frac{Gm(r)}{r^2} - \rho \frac{dV_{ext}}{dr} \tag{4.8}$$

where

$$m(r) = \int_0^r 4\pi r'^2 \rho(r') dr' \tag{4.9}$$

is the total mass at r. In this simple one-dimensional picture, V_{ext} is null. In order to complete the set of equations, we have to provide two relationships between P, T and ρ along the profile of the planet. The first one is obviously the equation of state of the considered material. The second one is the point where some hypothesis must be made on the mechanism which mainly transports the energy at r:

- if the energy is transported through diffusion and/or radiation, the energy flux is proportional to the temperature gradient [1]. The proper treatment is not presented here, but it is available in [**?**] or [**?**]. In this case, the temperature field defines the thermal gradient:

$$\nabla_T = \frac{d \ln T}{d \ln P} \tag{4.10}$$

[1] The proportionality cœfficient depends on T

is expressed as a function of T, P, ρ. At very high densities, this may be approximated as an isothermal profile since the thermal contribution to the pressure becomes negligible against the compression effects.

- if the temperature is too inhomogeneous, the diffusion and radiation cannot transport the luminosity and convective transport sets in. A proper study of the convective motion is a highly three-dimensional problem, which cannot be treated correctly in a one-dimensional formulation. However, it is possible to extract an one-dimensional stability criterion against convection from a stability analysis (see, e.g., [**?**]) in the formalism of the so-called mixing length theory. We will use here the Swcharzschild Härm criterion [**?**], which states that the medium is stable against convective motion if

$$\nabla_{ad} > \nabla_T \tag{4.11}$$

where the so-called adiabatic gradient is defined by:

$$\nabla_{ad} = \left.\frac{\partial \ln T}{\partial \ln P}\right|_S \tag{4.12}$$

and depends only on the equation of state. When the convection is the energy transport phenomenon, it is sufficiently efficient to impose this profile in the layer so that $\nabla_T = \nabla_{ad}$, and the profile of the planet is an isentropic one. It is important to notice that this approach does not include rotational or magnetic influence, which are known to have significant effects and have been integrated in some models [**?**].

Finally, we must define the boundary conditions of the model. The central values being hard to estimate, we must define them as surface values, which can be measured on planets we observe. The set of boundary conditions that is usually used is the surface temperature, the surface pressure and the total mass and radius of the planet. Let us notice that the surface thermodynamics are not trivial to define: the surface of the planet may be defined by its atmospheric pressure - which is purely conventional - but the corresponding surface temperature must be consistent with the observed luminosity. In the case of the solar system's planets, this is possible since measurement missions such as *Galileo* and *Cassini* give us the atmospheric $T-P$ profile. For faraway objects, the atmosphere must be modelled, which is out of the scope of this work; the reader can find a review in [**?**].

Finally, the system one has to solve to obtain the one-dimensional structure is:

$$\begin{cases} P(R) = P_0 & (4.13) \\ T(R) = T_0 & (4.14) \\ m(R) = M & (4.15) \\ \dfrac{dP}{dr} = -\rho\dfrac{Gm(r)}{r^2} - \rho\dfrac{dV_{ext}}{dr} & (4.16) \\ \dfrac{dm}{dr} = 4\pi r^2 \rho(r) & (4.17) \\ T(r) = T(\rho(r), P(r)) & (4.18) \\ \begin{cases} S(r) = S(T_0, P_0) & \text{in the case of a convective layer} \\ \nabla_T(r) = \nabla_{diff}(T, P, \rho) & \text{in the case of a diffusive layer} \\ T(r) = T_0 & \text{in the case of a quasi-isothermal layer} \end{cases} & (4.19) \end{cases}$$

given that 4.18 and 4.19 do not introduce new unknowns since the equation of state is supposedly known.

We have given the core idea of planetary modelling in this section, using the simplicity of the one-dimensional approach. However, a simple phenomenon has been neglected here, which would require more work: the self rotation of the planet. In order to see if this is an acceptable approximation, let us roughly compare the inertial rotational energy with the gravitational one:

$$m_{rot} = \frac{E_{rot}}{E_g} \simeq \frac{MR^2\omega^2/2}{GM^2/R} \simeq \frac{\omega^2 R^3}{GM} \tag{4.20}$$

In the case of the Earth $m_{rot} \sim 0.3\%$, and for the Sun $m_{rot} \sim 0.002\%$, so the one-dimensional description is sufficient; but for rapid spinners such as Jupiter ($m_{rot} \sim 9\%$) or Saturn ($m_{rot} \sim 15\%$), this effect is clearly crucial - Uranus and Neptune show a parameter of $2-3\%$, so that the effect is non-negligible as well. In the following section, we will show how to integrate this effect into a one-dimensional description.

I.3 The theory of planetary figures

We are now going to present the basic idea of the commonly used method to integrate the rotational contribution in the above formalism, which has been first used by Clairault [**?**] and proved correct later by Lyapunov [**?**]. A more extensive discussion of this method can be found in [**? ?**].

Basic idea

Let us consider a rotating quasi-spherical body with a rotation ω, leading to a V_{ext} rotational potential. As a consequence, the radial symmetry is lost but the axial North/South symmetry remains. However, we explained how a given profile $P(\rho)$ is obtained from (4.18) and (4.19). In consequence, the isodensity surfaces are the same as the isobaric ones, which are also the same as the equipotentials due to the hydrostatic balance; these surfaces are hereafter called *level surfaces*. Since we are considering a small perturbating potential, the level surfaces remain close to the spheres and may be expanded in terms of ellipsoids. The basic idea of the theory of planetary figures is then to reformulate the one-dimensional problem stated in the previous section in terms of a level variable l instead of r, given the relationship between l and (r, θ), which includes the rotational effect.

If we assume a solid body rotation and place ourselves in the frame of the rotating planet, the hydrostatic equilibrium can be rewritten:

$$\nabla P(\rho) = -\rho\nabla\left(-V_G(r,\theta) - \frac{1}{2}\omega^2 r^2 \sin^2\theta\right) \tag{4.21}$$

and the gravitational potential $V_G(r, \theta)$ must be recomputed carefully. We then describe the level surfaces in terms of a level parameter - for instance r_{eq} the equatorial radius of a given isobaric surface, or $\bar{r}$ the mean volumic radius[2] of a surface - and expand the level surfaces on either the Legendre polynomials:

$$r(r_{eq},\theta) = r_{eq}\left(1 + \sum_n l_{2n}(r_{eq}) P_{2n}(\cos\theta)\right) \tag{4.22}$$

[2]defined from the volume contained at level surface: $V(\bar{r}) = 4\pi\bar{r}^3/3$

or on the form of distorted ellipsoids. The aim is now to find a set of equations at each order for the l_{2n} set. In the case of Jovian planets, the expansion is needed up to the 3rd order, which can written as:

$$r(\bar{r},\theta) = r_{eq}(\bar{r})\left[1 - e(\bar{r})\cos^2\theta - \left(\frac{3e(\bar{r})^2}{8} + k(\bar{r})\right)\sin^2(2\theta) + \left(\frac{e(\bar{r})^3}{2} + h(\bar{r})\right)\sin^2\theta(5\sin^4\theta - 6\sin^2\theta + 1)\right] \quad (4.23)$$

where e, k, h are respectively 1st, 2nd and 3rd order perturbations, for which equations must be found by rewriting the hydrostatic equilibrium and the mass integral on this basis. In our planetary code, we used this formulation, so that it is the one we are going to present here; however, both distorted ellipsoids and Legendre polynomials are usable and the link between them can be found in [**? ?**].

The figures equation system

It can be shown that the gravitational potential for an axially symmetric mass distribution is expressed in terms of the even mass integrals:

$$V_G(\mathbf{r}) = -\frac{G}{r}\sum_{n=0}^{\infty}\left(\frac{D_{2n}(r)}{r^{2n}} + \bar{D}_{2n}(r)r^{2n+1}\right)P_{2n}(\cos\theta) \quad (4.24)$$

where P_n are the usual Legendre polynomials, and

$$D_n(\mathbf{r}) = 2\int_{r'<r}\rho(\mathbf{r}')(r')^n P_n(\cos\theta)d^3\mathbf{r}' \quad (4.25)$$

$$\bar{D}_n(\mathbf{r}) = 2\int_{r'>r}\rho(\mathbf{r}')(r')^{-n-1} P_n(\cos\theta)d^3\mathbf{r}' \quad (4.26)$$

Let us rewrite our system of equations as an adimensional one, using the mean radius $\bar{r}$ as level parameter:

$$\beta = \bar{r}/\bar{R} \quad (4.27)$$

$$\delta(\beta) = \rho(\bar{r})/\bar{\rho} \quad (4.28)$$

$$\Pi(\delta) = P(\bar{r})/\frac{GM\bar{\rho}}{\bar{R}} \quad (4.29)$$

$$S_n(\beta) = \frac{3D_n(\bar{r})}{4\pi\bar{\rho}\bar{R}^{n+3}\beta^{n+3}} \quad (4.30)$$

$$\bar{S}_n(\beta) = \frac{3\bar{D}_n(\bar{r})}{4\pi\bar{\rho}\bar{R}^{2-n}\beta^{2-n}} \quad (4.31)$$

where $\bar{R}$ is the mean volumic radius of the whole planet. The reduced mass integrals are then expressed as:

$$S_n(\beta) = \frac{1}{\beta^{n+3}}\int_0^{\beta}\delta(z)d[z^{n+3}\phi_n(z)] \quad \text{and} \quad S_n(\beta) = \beta^{n-2}\int_{\beta}^{1}\delta(z)d[z^{2-n}\bar{\phi}_n(z)] \quad (4.32)$$

with

$$\phi_0 = 1 \tag{4.33}$$
$$\phi_2 = -\frac{2}{5}\left(e + \frac{1}{6}e^2 + \frac{4}{7}k + \frac{2}{9}e^3 - \frac{1}{7}h + \frac{4}{3}ek\right) \tag{4.34}$$
$$\phi_4 = \frac{12}{35}\left(e^2 + \frac{8}{9}k + \frac{1}{3}e^3 + \frac{16}{33}h + \frac{40}{297}ek\right) \tag{4.35}$$
$$\phi_6 = -\frac{8}{21}\left(e^3 + \frac{30}{143}h + \frac{192}{143}ek\right) \tag{4.36}$$
$$\bar{\phi}_0 = \frac{3}{2}\left(1 - \frac{4}{45}e^2 - \frac{244}{2835}e^3 - \frac{32}{315}ek\right) \tag{4.37}$$
$$\bar{\phi}_2 = -\frac{2}{5}\left(e + \frac{9}{14}e^2 + \frac{4}{7}k + \frac{8}{21}e^3 - \frac{1}{7}h + \frac{4}{7}ek\right) \tag{4.38}$$
$$\bar{\phi}_4 = \frac{32}{105}\left(k + \frac{6}{11}h + \frac{14}{33}ek\right) \tag{4.39}$$
$$\bar{\phi}_6 = -\frac{80}{1001}\left(h - 4ek\right) \tag{4.40}$$

The hydrostatic equilibrium (4.16) then becomes:

$$\frac{1}{\delta}\frac{d\Pi}{d\beta} = \frac{d}{d\beta}[\beta^2 \hat{V}_0] \tag{4.41}$$
$$\{\hat{V}_n(\beta) = 0\}_{n=2,4,6} \tag{4.42}$$

where

$$\begin{aligned}\hat{V}_0 = &\left(1 + \frac{8}{45}e^2 + \frac{64}{315}ek + \frac{584}{2835}e^3\right) S_0 + \frac{2}{5}\left(e + \frac{13}{14}e^2 + \frac{4}{7}k\right) S_2 \\ &+ \bar{S}_0 - \frac{4}{15}\left(e + \frac{19}{42}e^2 + \frac{4}{7}k\right) \bar{S}_2 + \frac{1}{3}m_{rot}\left(1 + \frac{14}{15}e + \frac{2}{63}e^2 + \frac{16}{105}k\right)\end{aligned} \tag{4.43}$$
$$\begin{aligned}\hat{V}_2 = &\left(\frac{2}{3}e + \frac{31}{63}e^2 + \frac{76}{189}e^3 + \frac{88}{315}ek - \frac{2}{21}h + \frac{8}{21}k\right) S_0 \\ &+ \left(1 + \frac{4}{7}e + \frac{10}{7}e^2 - \frac{16}{35}k\right) S_2 + \frac{20}{21}eS_4 + \left(1 - \frac{8}{21}e + \frac{32}{105}k\right) \bar{S}_2 \\ &- \frac{16}{21}e\bar{S}_4 - \frac{1}{3}m_{rot}\left(1 + \frac{20}{21}e + \frac{38}{63}e^2 + \frac{16}{15}k\right)\end{aligned} \tag{4.44}$$
$$\begin{aligned}\hat{V}_4 = &\left(\frac{4}{35}e^2 - \frac{172}{1155}e^3 - \frac{32}{35}k - \frac{192}{385}h - \frac{416}{1155}ek\right) S_0 \\ &+ \left(\frac{36}{35}e + \frac{402}{385}e^2 - \frac{48}{385}k\right) S_2 + \left(1 + \frac{200}{231}e\right) S_4 \\ &+ \left(-\frac{24}{35}e - \frac{4}{55}e^2 + \frac{32}{385}k\right) \bar{S}_2 + \left(1 - \frac{160}{231}e\right) \bar{S}_4 \\ &+ m_{rot}\left(\frac{8}{35}e + \frac{76}{231}e^2 + \frac{32}{55}k\right)\end{aligned} \tag{4.45}$$
$$\begin{aligned}\hat{V}_6 = &\left(\frac{8}{231}e^3 - \frac{128}{231}ek + \frac{80}{231}h\right) S_0 + \left(\frac{12}{77}e^2 - \frac{96}{77}k\right) S_2 + \frac{50}{33}eS_4 + S_6 \\ &+ \left(\frac{32}{77}e^2 + \frac{64}{77}k\right) \bar{S}_2 - \frac{40}{33}e\bar{S}_4 + \bar{S}_6 + m_{rot}\left(-\frac{32}{231}e^2 - \frac{64}{231}k\right)\end{aligned} \tag{4.46}$$

This system of equations can be solved numerically with a self-convergent procedure:

- starting from a linear density profile and $m_{rot}, e, k, h = 0$, the mass integrals $S_0, \bar{S}_0$ are computed and injected into the hydrostatic equilibrium to extract the

corresponding $\Pi(\beta)$, which is reverted into $\delta(\beta)$ with the $P(\rho)$ thermodynamic profile (isentrope, isothermal, diffusive). The procedure is then repeated until convergence of δ and Π is reached

- m_{rot} is set to its value and e is estimated from the nullity of $\hat{V}_2$; we then compute the system up to $n = 2$ with the same converging procedure
- the second-order and third-order terms are introduced the same way each time convergence is reached for the previous one

Measurable quantities: the gravitational moments

One of the main pros of these models is the capacity to extract the surface gravitational field, which is also measured by space programs such as *Pioneer* and *Voyager*, leading to experimental measurements such as presented on Table (4.1).

	Jupiter	**Saturn**	**Uranus**	**Neptune**
$M \times 10^{-29}$[g]	18.986112(15)	5.684640(30)	0.8683205(34)	1.0243542(31)
$R_{eq} \times 10^{-9}$[cm]	7.1492(4)	6.0268(4)	2.5559(4)	2.4766(15)
$R_{pol} \times 10^{-9}$[cm]	6.6854(10)	5.4364(10)	2.4973(20)	2.4342(30)
$\bar{R} \times 10^{-9}$[cm]	6.9894(6)	5.8210(6)	2.5364(10)	2.4625(20)
$\bar{\rho}$[g·cm^{-3}]	1.3275(4)	0.6880(2)	1.2704(15)	1.6377(40)
$J_2 \times 10^2$	1.4697(1)	1.6332(10)	0.35160(32)	0.3539(10)
$J_4 \times 10^4$	-5.84(5)	-9.19(40)	-0.354(41)	-0.28(22)
$J_6 \times 10^4$	0.31(20)	1.04(50)	...	...
$P_\omega \times 10^{-4}$[s]	3.57297(41)	3.83577(47)	6.206(4)	5.800(20)
m_{rot}	0.08923(5)	0.15491(10)	0.02951(5)	0.02609(23)

Table 4.1: Numbers taken from [**?**] and references therein. The numbers in parentheses are the uncertainty in the last digits of the given value.

Of particular interest is the measurement of the gravitational moments, which are defined by the expansion on the Legendre polynomials:

$$J_{2n} = -\frac{1}{M R_{eq}^{2n}} \iiint \rho(r,\theta) P_{2n}(\cos\theta) d\mathbf{r} \tag{4.47}$$

and quantify the departure from sphericity of the planet. Using these measurements, it is possible to construct (and reject) models of the deep interior composition. In terms of the generalized ellipsoids functions, these moments can be written as:

$$\begin{aligned} J_2 =& \frac{2}{3}e - \frac{m_{rot}}{3} - \frac{e^2}{3} + \frac{2}{21}em_{rot} + \frac{8}{21}k - \frac{11}{147}e^2 m_{rot} - \frac{16}{105}km_{rot} \\ &+ \frac{40}{147}ek - \frac{2}{21}h \end{aligned} \tag{4.48}$$

$$J_4 = -\frac{4}{5}e^2 - \frac{32}{35}k + \frac{4}{7}em_{rot} + \frac{4}{5}e^3 - \frac{3616}{2695}ek - \frac{22}{49}e^2 m_{rot} + \frac{208}{385}km_{rot} - \frac{192}{385}h \tag{4.49}$$

$$J_6 = \frac{8}{7}e^3 + \frac{128}{77}ek - \frac{20}{21}e^2 m_{rot} - \frac{160}{231}km_{rot} + \frac{80}{231}h \tag{4.50}$$

II A quick overview of existing models for giant planets

II.1 The basic assumptions of a gaseous planet model

Planetary models must be consistent with planetary formation models, surface measurements and our knowledge of physics. The general idea is that a planet such as Jupiter is composed of a mixture of hydrogen, helium and heavier elements such as "ices" - i.e., a mixture of water, ammonia and methane under high-pressure conditions - and "rocks" - iron or silicates. The distribution of these elements along a planet profile is opened to hypothesis, but the actual models tend to spatially separate the hydrogen/helium mixture from heavier elements by supposing concentric shells. The number and composition of the shells can be adjusted in order to match the surface observations.

The most common models, on which we will focus here, all suppose that the planet is divided into homogeneous layers of different compositions, and these compositions can be used as free parameters to adjust the model to the observed planets.

The first one is a standard two-layer model first proposed by Hubbard and Horedt [**?**] and is represented as model (1) on Figure (4.1). It has been reused and modified with a few adjustments in many studies concerning both Jovian planets - for which we have a significant parameters constraint - [**?** **?**], and exoplanets - for which the gravitational moments are unknown - [**?** **?**]. The planet is divided into an outer hydrogen-helium envelope with helium mass fraction Y, and a central core of mass M_c, which is itself made of rocks (in a proportion α) and ices; the rocks and ices may be separated into an inner core and an outer core in some versions of the model. The planet rotates as a solid body.

Other models, introduced in [**?**] and referred as model (2), suppose that the molecular-metallic transition of hydrogen could be a discontinuous transition, leading to a separation of the hydrogen/helium part into two separate layers along different isentropic profiles. This phase separation also allows for helium enrichment in the inner envelope, so that helium abundance in this region can either be another free parameter, or set to ensure protostellar abundance as the mean helium fraction throughout the planet. This phase separation was justified by the widely used Saumon-Chabrier-Van Horn equation of state for hydrogen [**?**], which was build on analytical techniques, and predicted this transition to be of the first order. These models have been used in studies such as [**?** **?**].

A third class of models (3) has recently been proposed by Militzer *et.al* [**?**]. The assumption is that the molecular-metallic transition for hydrogen is continuous, as suggested by *ab initio* equations of state for hydrogen [**?** **?**], so that the envelope cannot be separated into an outer and inner envelope; the envelope is still assumed to be homogeneous due to convection, so that there is no possibility to adjust the gravitational harmonics with the composition of each layer. In order to give another physically plausible free parameter in this model, they introduced differential rotation in the planet instead of a solid-body rotation.

In all of these models, the metallicity of the envelope is possibly taken into account through an effective helium over-abundance [**?** **?**]; it is also possible to use a simple equation of state as SESAME [**?**] or ANEOS [**?**] and an additive volume law (see, e.g., [**?**] for a discussion) to account for these elements in the envelope [**?** **?** **?** **?**].

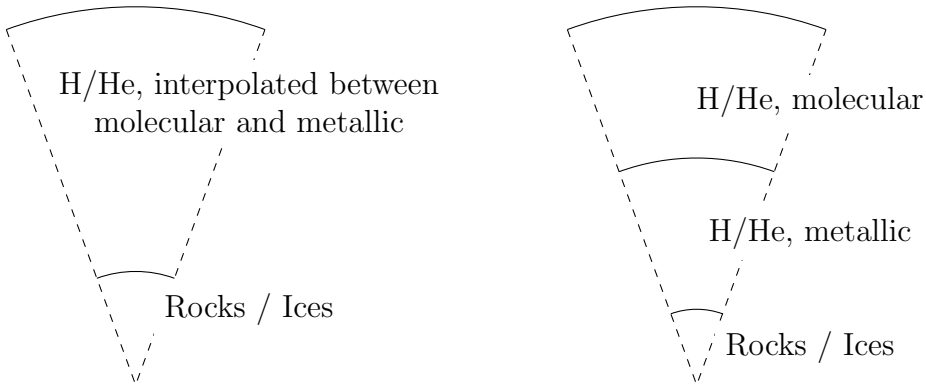

(a) Two-layer models (1, 3)

(b) Three-layer models (2)

Figure 4.1: Basic view of models of planetary interiors

II.2 The importance of the equation of state

The importance of the equation of state (EOS) have been studied, e.g., by Saumon and Guillot [**?**], Nettelmann *et.al* [**?**] and Fortney and Nettelmann [**?**] for Jupiter and Saturn, and Baraffe, Chabrier and Barmann [**?**] for exoplanets.

The conclusion is that each EOS leads to a complete family of interior models that match the constraints. Figure (4.2a) shows three-layer models composition - mass of the core and envelope metallicity - which reproduce the observed constraints within a 2σ error. It is interesting to notice that different EOS for the hydrogen-helium mixture lead to very different models (see [**?**] for details on the used EOS). However, even with a given EOS, very small uncertainties lead to drastic uncertainties in the computed planet, as can be seen on Figure (4.2b).

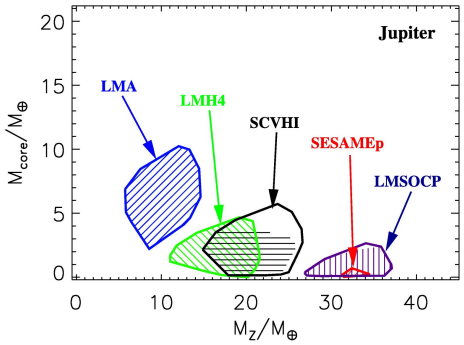

(a) Mass of the core and heavy elements in acceptable models of Jupiter interiors using different equations of state. These models lead to gravitational moments equal to Jupiter's within 2σ uncertainties.

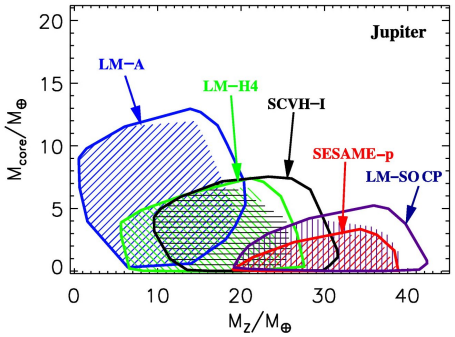

(b) Same as Figure (4.2a), with an arbitrary modification of 2% in the H/He isentrope.

Figure 4.2: Influence of the H/He equation of state on the planetary profile, taken from [**?**]

If this shows the importance of the hydrogen / helium EOS in the case of Jupiter, the other materials are less important to determine its structure; however, the ices and rocks' EOS may be of significant importance in the case of the icy giants Uranus and Neptune, and for some exoplanets. The importance of these EOS have been tested in [**?**], with very simple models of massive exoplanets with no core and all heavy elements distributed in a single layer of hydrogen and helium. They tested the most well-known EOS at this date, namely the SESAME and ANEOS databases. As can be seen on Figure (4.3), the choice of the EOS can have a relatively important impact on the predicted central pressure and density, leading to a clear need for reliable EOS.

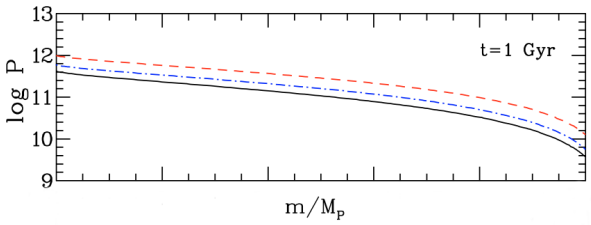

Figure 4.3: Effect of the EOS on the inner profile as a function of fractional mass for a planet of $20M_\oplus$ with a mass fraction $Z = 50\%$ of heavy elements distributed over the entire planet. The heavy elements are described with an equivalent helium mass (solid line), SESAME water EOS (dash-dotted line) or ANEOS water EOS (dashed line).

For this work, I wrote a code that uses the theory of figures to compute simple static 3-layer models, with an easy way to test various equations of states.

III Conclusion

We have shown how current planetary models are built and what formalism is used in order to take into account the rotation of Jovian planets. The measurements of the gravitational moments of neighbouring planets allow us to constrain our models and infer the deep interior structure of these bodies. However, the knowledge of an accurate equation of state for every material and their mixtures is necessary to have a quantitatively reliable model. Depending on the type of planet, a given equation of state's accuracy can be crucial to determine its structure; and even if we did not focus on it here, its evolution is affected as well by the choice of the equation of state.

In the next chapters, we are going to focus on the construction of usable EOS for ices from *ab initio* methods.

Chapter 5

An equation of state for water in planetary interiors

Contents

I Water EOS and planetary interiors 60

I.1 The available equations of state 60

I.2 The phase diagram of water 60

II Building our equation of state 62

II.1 Creating the pseudopotentials 62

II.2 Ab initio simulations 63

II.3 Extension to very high densities 65

III A numerical fit 67

III.1 Translational part 67

III.2 Plasma and superionic phases excess energy 67

III.3 Low-density regime 68

III.4 Interpolation and further adjustments 68

III.5 Comparison with previous packages 69

IV Testing the equation of state: comparison with water shock experiments 70

IV.1 Principal Hugoniot curve 71

IV.2 Reshocked Hugoniot curve 72

IV.3 Precompressed Hugoniot curves 73

V Conclusion 73

As we have shown in the previous section, the accurate knowledge of the equation of state (EOS) is crucial for a planetary model to be reliable. Among the expected materials are "ices", which are in fact a mixture of water, ammonia and methane. Although the mixture's properties are still to be examined, the case of water is different since it has been extensively studied. The relevant pressure conditions for the solar icy giants Uranus and Neptune show a particular phase transition, which have first been predicted by Cavazzoni *et.al* in 1999 [**?**], and will be presented here.

In this work we will extend the knowledge of a water EOS to very high pressures, which are only relevant for super Jupiter extrasolar planets such as the extremely dense $2M0746 + 20b$ [**?**], which weigh 30 Jupiter masses for a radius equal to 0.97 times Jupiter's. We will discuss the stability of the - simplified - phase diagram relevant for Jovian and extrasolar planets. With the help of Alexander Potekhin [1], we provided an analytic fit of our tabulated EOS. We finally show some very simple planetary models computed with this EOS.

I Water EOS and planetary interiors

I.1 The available equations of state

The first EOS used in the context of planetary interiors were perturbated polytropes fitting shock experiments results. An example of such a simple EOS was used in [**?**]:

$$P = \rho^{3.71926} \exp(-2.75591 - 0.271321\rho + 7.00925 \times 10^{-3}\rho^2) \tag{5.1}$$

As experimental data grew, finer fits could be made, and the semi-theoretic EOS ANEOS [**?**] and SESAME [**?**] became available and widely used. These EOS were constructed from analytic models (Thomas-Fermi for electronic contribution, Mie-Grüneisen EOS for the cold curve, Debye model for nuclear contributions ...) with fitting parameters adjusted to match the experimental data. These equations have been used extensively in planetary models over the past years [**? ? ? ?**] and continuously updated with new, more reliable experimental data.

With growing computational power, it became possible to directly compute a tabulated EOS from first-principles simulations. The first extensive study of this kind was published by Martin French in 2009 [**?**], in which he tabulated an EOS up to 100Mbar, 24000K, corresponding to Jupiter's core conditions. He then improved this tabulated data with a simple quantum model for molecular contribution [**?**] and this EOS was assessed by experimental shock data [**?**]. This EOS was also completed in low-density range [**?**] and low-temperature range [**?**]. More recently, a very robust EOS - including Gibbs free energy computation - has been published by Soubiran [**?**], but it only covers Uranus and Neptune interiors.

This work aims at extending French's work to higher pressures and temperature, in order to have a usable EOS for a very large range of thermodynamic conditions, from Jovian planets atmospheres to super Jupiter cores.

I.2 The phase diagram of water

If the phase diagram of water at low-pressure conditions is known to show a wide variety of crystal phases, the warm dense matter regime - which is relevant for planetary

[1] Iofee Institute, St-Petersburg, Russia

interiors - is less complicated. It mostly exhibits a molecular fluid phase, a pressure-ionized fluid regime, two solid phases - ices VII and X - and a unique phase, the so-called superionic (SI) phase.

The superionic phase

As first predicted from numerical simulations by Cavazzoni in 1999 [**?**], the superionic phase of water has the following properties:

- the oxygen ions are fixed on lattice sites. It is generally admitted that it should be a BCC lattice, since the SI phase is obtained by heating ice VII or X - which exhibit a BCC structure for oxygen ions - above 2000 K; however, a study by Wilson [**?**] suggested that the oxygen lattice may adopt a FCC configuration under certain thermodynamic conditions

- the hydrogen ions diffuse among the interstitial lattices

The oxygen lattice and hydrogen isodensity surfaces are represented on Figure (5.1) for both BCC and FCC configurations.

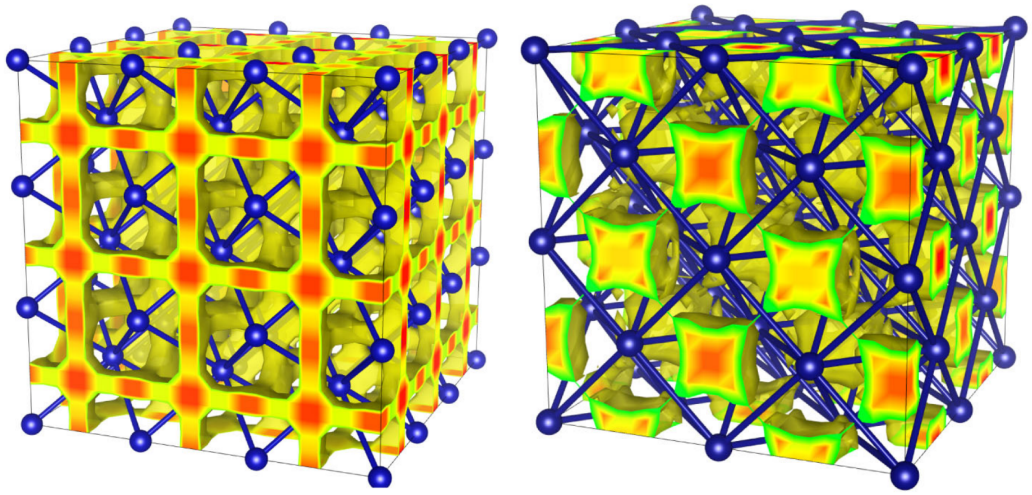

(a) BCC lattice (b) FCC lattice

Figure 5.1: Isosurfaces of constant hydrogen density in a SI phase. Taken from [**?**]

This phase is located in the relevant region for Uranus and Neptune interiors. These planets have been intriguing since the *Voyager 2* mission reported an unusual non-dipolar and non-axisymmetric magnetic field structure for both of them. Since the SI phase conducts electricity through both electronic and protonic transport [**?** **?**], it is a key ingredient to these planets' dynamos. It has been recently shown by Redmer [**?**] that an acceptable model of Uranus or Neptune with regard to the gravitational moments is compatible with the constraints raising from dynamo simulations [**?** **?**], ensuring the importance of this phase in planetary science.

II Building our equation of state

II.1 Creating the pseudopotentials

The pseudopotentials were generated with the ATOMPAW code [**?**]. These pseudopotentials use GGA-PBE exchange-correlation functional, and in order to explore very high-density regimes, very short cutoff radii have been used: 0.6 bohr for oxygen pseudopotentials and 0.4 bohr for hydrogen pseudopotentials. The original and pseudized wavefunctions $1s$ and $2s$ for the oxygen pseudopotential are displayed on Figure (5.2).

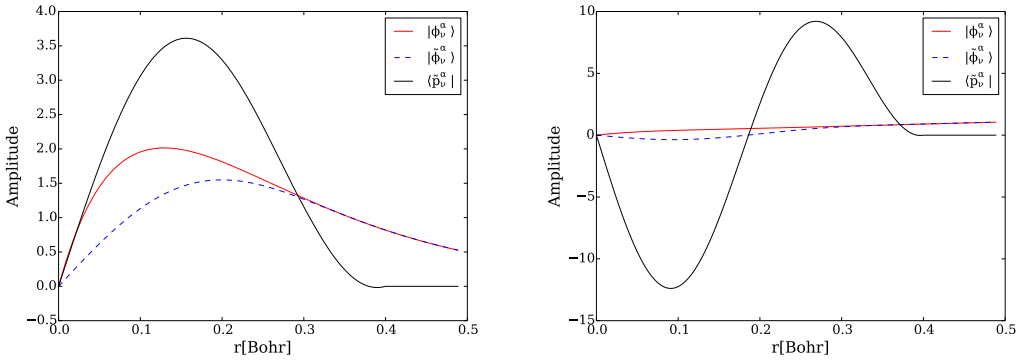

(a) $1s$ orbital (b) $2s$ orbital

Figure 5.2: Pseudopotential wavefunctions, pseudized wavefunctions and projectors

They have been tested against Jollet's pseudopotentials [**?**] that reproduce the all-electron calculations; the test cold curves of pure FCC lattices are displayed in Figure (5.3), and the equilibrium lattice parameter and bulk modulus extracted for comparison. These pseudopotentials will be used throughout the following discussion.

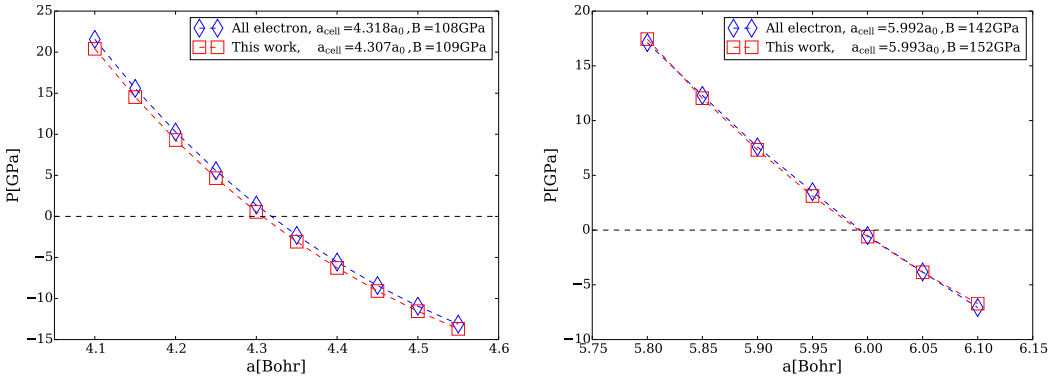

(a) Hydrogen (b) Oxygen

Figure 5.3: Pseudopotential cold curves

II.2 Ab initio simulations

Method

The computations were carried using the ABINIT [**?** **?**] package for densities from 7 to 50 g.cm^{-3}. Convergence tests confirm results from French et al. [**?**] for k-points, so that we use computations at the Γ point ; the cutoff energy is pseudopotential-dependant, and our tests lead to a very high cutoff energy 100 Ha, in relation with the stiffness of our pseudopotentials. The simulations were run for at least 800 timesteps each, with a timestep of $5a.u = 0.12fs$. The temperature of the box was controlled by velocity scaling [**?**], so that we sampled the isokinetic ensemble.

The phase of water (solid, liquid or superionic) has been determined using a combination of two tools:

- the mean-square displacement of the species (Lindemann criterion); an example can be seen on Figure (5.4) for water at various temperatures along the $\rho = 20$g·cm^{-3} isochore. It is quite clear with this representation whether the atoms diffuse or not, and in consequence it can be used to identify the SI phase or the fluid phase. It is important to note that this diagnostic tool relies on the precise definition of the SI phase.

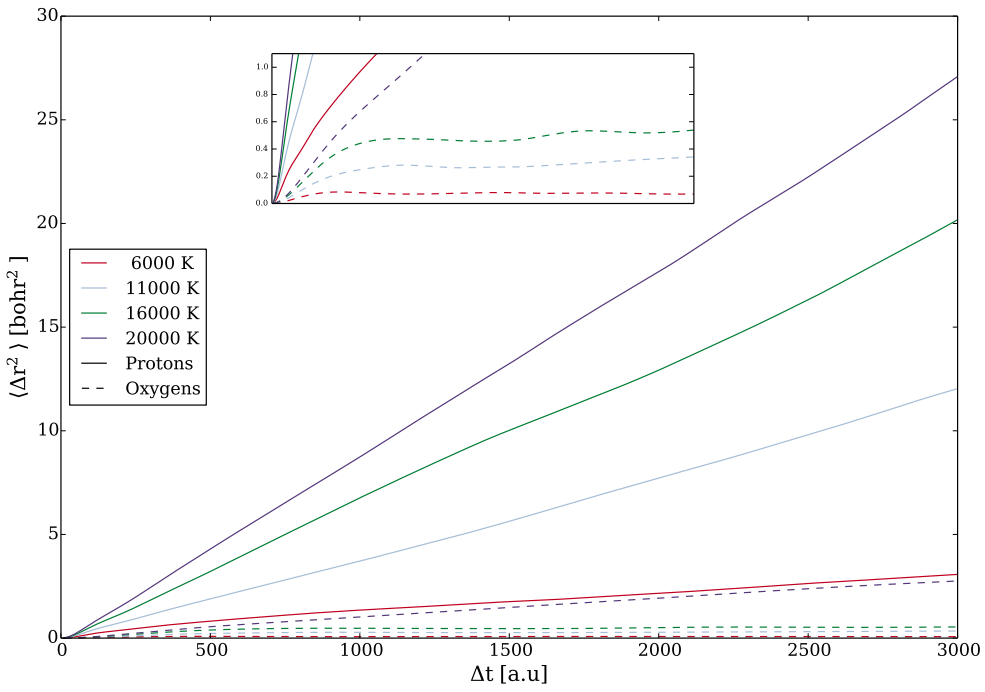

Figure 5.4: Mean-square displacements for both hydrogen and oxygen atoms along the $\rho = 20$ g·cm^{-3} isochore. Insert: zoom on the oxygen lattice parts.

- a visual recognition of a solid or fluid behavior by projection on a plane; although less quantitative than other methods, it leads to a practical visual definition of the phase; the general idea can be seen in Figure (5.5). In these representations, the protons are clearly seen diffusing while the oxygen lattice melts between 16000 and 20000 K at 20 g.cm^{-3}.

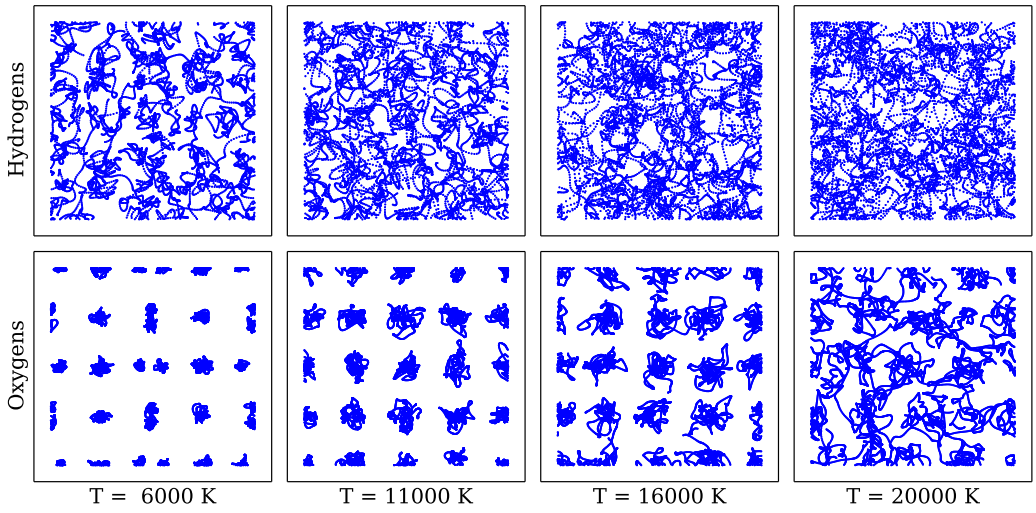

Figure 5.5: Trajectories visualizations for both hydrogen and oxygen atoms along the $\rho = 20$ g·cm^{-3} isochore.

In addition, an examination of the pair-distribution functions confirms that the SI lattices are correctly identified and stay the same throughout the simulation, as can be seen in Figure (5.6). It also shows that the fluid state near the transition already has a short-range order for oxygen atoms.

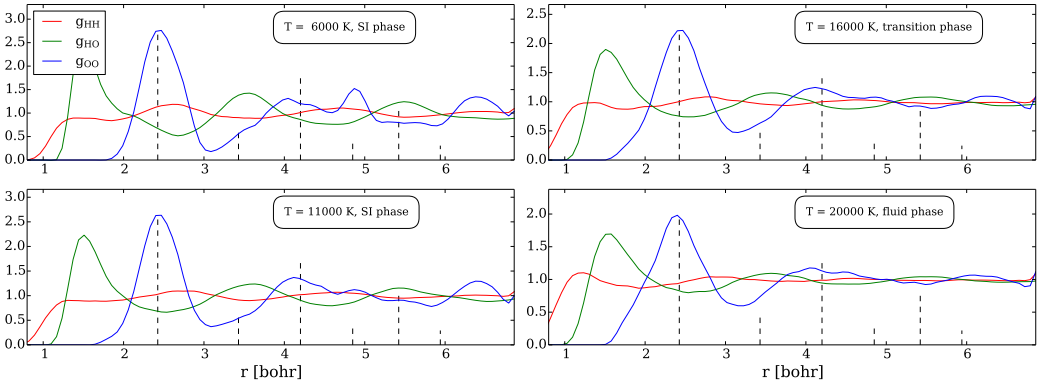

Figure 5.6: Pair distribution functions along the $\rho = 20$ g·cm^{-3} isochore. The dotted bars are the ideal FCC lattice pdf peaks.

Following Wilson *et.al* [**?**], we tried both FCC and BCC oxygen lattices for the SI phase on a few simulation points. The lattice is expected to be marginally deformed if the stable phase is one and the simulation cell only allows the other due to periodicity at boundary limits. Our simulation box contains 54 water molecules when we try a BCC lattice and 32 water molecules when we try FCC lattice - except when we perform convergence tests at 64 molecules. It appears quite clearly from trajectory representation that the FCC phase is generally more stable, as predicted by Wilson *et.al* (see Figure (5.7)). However, the thermodynamic quantities are only loosely dependent on the structure (see the first table of [**?**] online supplementary material, or Table (5.1) in our interest domain), and the differences in pressure or energy lie in a 2% uncertainty, which is still less than the uncertainty introduced by the choice of the functional and the pseudopotentials themselves.

Finally, we choose our simulation size depending on the convergence requirement in

ρ	T	P_{BCC}	P_{FCC}	$\frac{\Delta P}{P_{BCC}}$	U_{BCC}	U_{FCC}	$\frac{\Delta U}{U_{BCC}}$
15	6000	89.15(15)	90.28(21)	1.3%	-668.62(6)	-668.10(8)	0.08%
20	6000	166.80(20)	168.27(27)	0.9%	-656.27(6)	-655.61(6)	0.10%
25	6000	267.63(30)	269.54(32)	0.7%	-643.35(6)	-642.59(7)	0.12%
15	20000	95.30(32)	96.42(44)	1.2%	-664.51(15)	-664.18(20)	0.05%
30	20000	401.46(58)	404.90(77)	0.8%	-625.79(14)	-625.11(20)	0.11%

Table 5.1: Comparison of thermodynamic quantities for the BCC or FCC superionic structure. The uncertainties on the last digit are given in parenthesis. Densities are given in g·cm^{-3}, temperatures in K, pressures in Mbar and energies in eV/atom.

order to save computer time. When the density is lower than 15 g·cm^{-3}, 32 molecules do not lead to a sufficient size convergence at the Γ point, so that either 64 molecules or more k-points are needed: in that case, we use 54-molecules simulations. Above 15 g·cm^{-3}, a 32-molecules box at the Γ point is sufficient, and we use these parameters in our calculations.

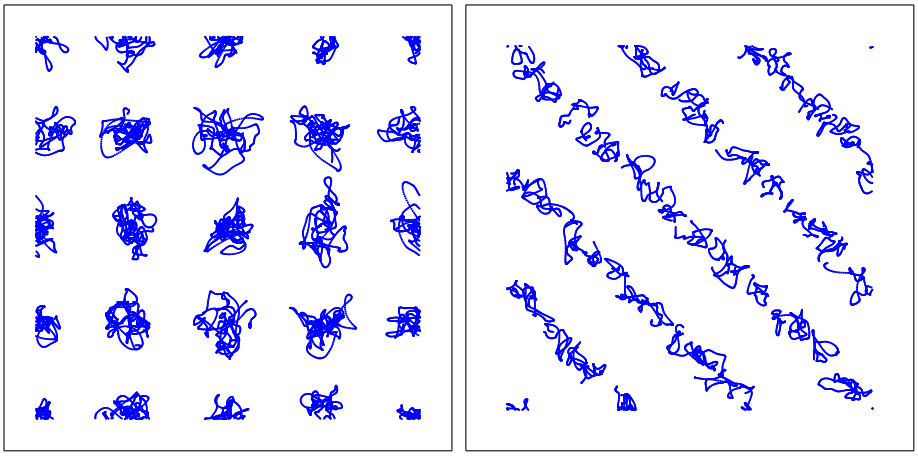

Figure 5.7: Comparison of trajectories of the oxygen atoms in the case of an attempted FCC lattice (left picture, 32 atoms) or BCC lattice (right picture, 54 atoms) at $\rho = 20$ g.cm^{-3} and $T = 11000$ K. It can be seen that the FCC lattice seems more stable than the BCC one.

Results

The EOS table from our computations is given in Appendix C. We extended the knowledge of the Ab initio EOS for water to the realm of moderately heavy Super Jupiter planets, as can be seen in Figure (5.8).

However, simple models of heavier Super Jupiter planets (with SESAME or ANEOS EOS), taken from Baraffe *et.al* [**?**] lead to very high densities inside the core, up to 110 g.cm^{-3}. In consequence, we need to extend the calculations to higher densities, even if we are limited by the pseudopotentials' cutoff radii.

II.3 Extension to very high densities

The pseudpotentials are only usable as long as they do not overlap each other, which leads to a strong limitation on density. Even with our homemade ultra short pseu-

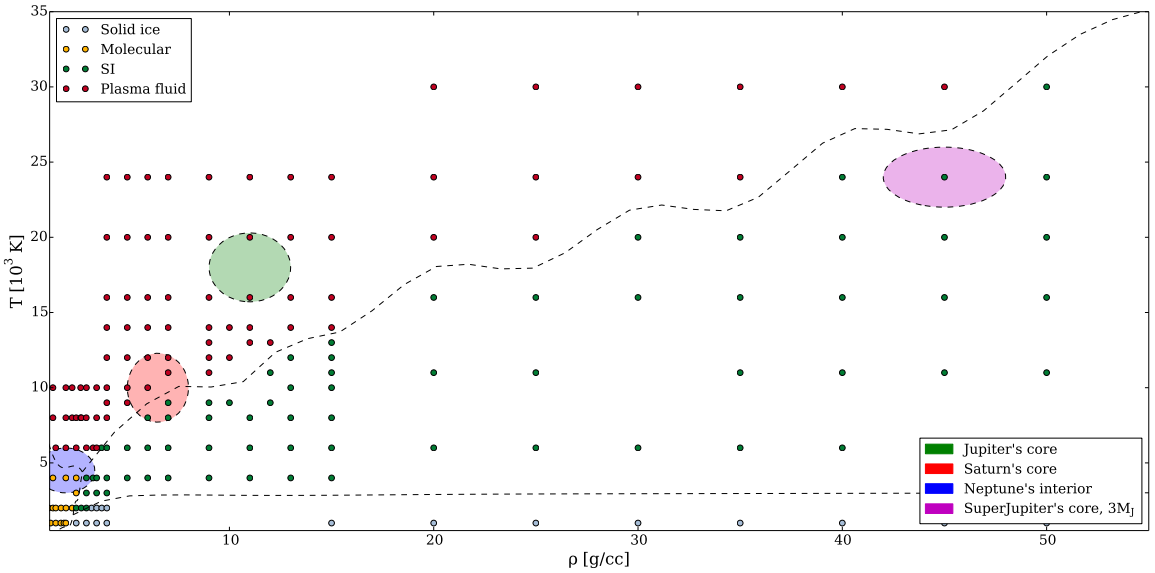

Figure 5.8: Available EOS points in the (ρ, T) plane by combining French *et.al* [**?**] and this work. Each dot represents a DFT numerical simulation.

dopotentials, the highest correctly sampled density was 50g/cc. We tried to reach the Thomas-Fermi limit by switching to another approach, the Orbital-Free Molecular Dynamics (OFMD) approach. We used a Perdew-Zunger [**?**] functional and checked that the OFMD results were consistent with the DFT between 35 and 50 g/cc, so that we could switch the method while increasing the density. The result of this test can be seen in Figure (5.9).

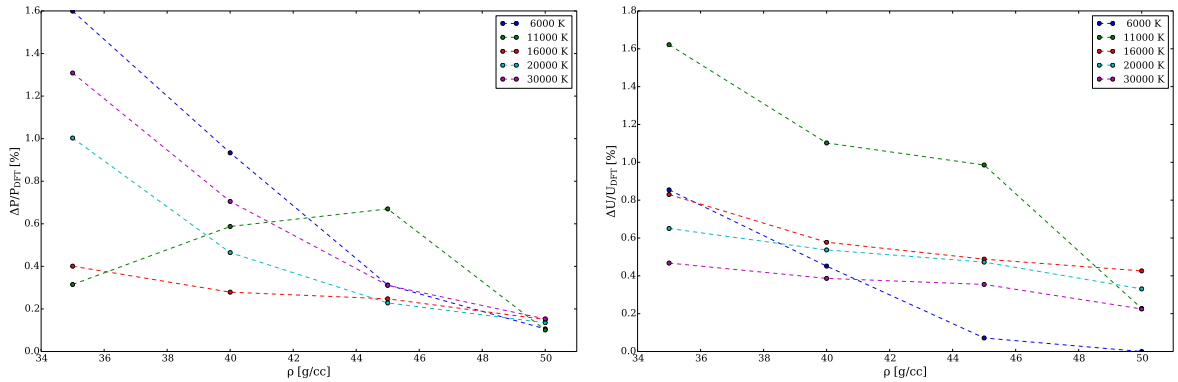

(a) Relative pressure difference between DFT and TF

(b) Relative energy difference between DFT and TF

Figure 5.9: Transition to an OFMD approach.

In conclusion, we can use the OFMD approach to extend our numerical results at even higher pressures. The EOS table from our OFMD computations can be found in Appendix C. We are going to see that reaching $\rho \sim 100$ g.cm^{-3} is sufficient to reach the analytic One Component Plasma (OCP) limit.

III A numerical fit

With the help of Alexander Potekhin, we tried to design a practical numerical fit for planetary models. We do not provide a different fit for different fluid phases, since we wanted primarily to provide a numerical, thermodynamically consistent fit for practical purposes. The fit is designed to reproduce the following data:

- at very low density and temperatures, the experimental tables from Wagner & Pruss [**?**]
- in all relevant range, the combination Ab Initio tables constructed from French [**?**], Soubiran [**?**] and this numerical work

We will use the classical plasma parameters Γ and r_s, as defined in Chapter 1.

III.1 Translational part

In all the phases, the kinetic contribution to the free energy will be taken as the molecular one:

$$F^{id} = N_{\mathrm{H_2O}} k_B T [\ln(n_{\mathrm{H_2O}} \lambda_{\mathrm{H_2O}}^3) - 1] \tag{5.2}$$

where

$$\lambda_{\mathrm{H_2O}} = \left[\frac{2\pi\hbar^2}{m_{\mathrm{H_2O}} k_B T} \right]^{1/2} \tag{5.3}$$

is the molecular thermal wavelength.

III.2 Plasma and superionic phases excess energy

Alexander Potekhin constructed an analytical parametrization of the Helmholtz free energy of water in the plasma phase at temperature 10^3 K $- 10^5$ K and mass density ρ between a few g.cm^{-3} and 100 g.cm^{-3} by expressing it as the free energy of electrons with an effective electron density:

$$F_{pl}^{ex}(N_i, T, V) = F_e(N_*, T, V) \tag{5.4}$$

where N_i is the total number of ions and $n_* = N_*/V$ the effective electron density. Here F_e is the free energy of an ideal Fermi gas:

$$F_e(N_e, T, V) = \mu_e N_e - P_{id}^{(e)} V \tag{5.5}$$

where in the nonrelativistic case,

$$P_{id}^{(e)} = \frac{8}{3\sqrt{\pi}} \frac{T}{\lambda_e^3} I_{3/2}(\mu_e/T) \tag{5.6}$$

$\lambda_e = (2\pi\hbar^2/m_e T)^{1/2}$ being the electron thermal de Broglie wavelength, T being measured in energy units.

$$\mu_e/T = X_{1/2}(n_e \lambda_e^3 \sqrt{\pi}/4) \tag{5.7}$$

$$I_\nu(X) = \int_0^\infty \frac{x^\nu dx}{\exp(x - X) + 1} \tag{5.8}$$

is the standard Fermi integral, and $X_\nu(I)$ is the inverse function.

The effective electron density is written $n_* = n_i Z_*$, with:

$$Z_* = \frac{10}{3}\left(1 + \frac{2.35 r_s}{1 + 0.09/(rs\sqrt{\Gamma_e})} + \frac{5.96 r_s^{3.78}}{(1 + 17/\Gamma_e)^{3/2}}\right)^{-1} \tag{5.9}$$

This formula is constructed in order to recover $Z_* = \frac{10}{3}$ at high density, so that the excess free energy will be represented by the excess energy of the degenerate electron gas. This is consistent with the physical idea of pressure ionization and the fact that the electronic properties dominate in this regime. Since we are not seeking fine effects such as a phase transition, we do not include the excess ionic contribution in the free energy.

III.3 Low-density regime

In the moderate-density liquid regime ($\rho \lesssim 1$ g.cm^{-3} and 300 K $\lesssim T \lesssim$ 2000 K), the excess free energy of liquid water is written as:

$$F_{liq}^{ex} = \frac{N_{\mathrm{H_2O}}^2}{V}(b_{vdw} k_B T - a_{vdw}) + \frac{2}{3} N_{\mathrm{H_2O}} k_B T (b_{vdw} n_{\mathrm{H_2O}})^{3/2} \left[1 + \left(\frac{a_1}{k_B T}\right)^{a_2}\right] \tag{5.10}$$

where $a_{vdw} = 2.357 a_0^3$ Ha and $b_{vdw} = 340.8 a_0^3$ Ha are the tabulated Van der Waals constants for molecular water [**?**], $N_{\mathrm{H_2O}} = N_i/3$ is the total number of water molecules. The term with fitting parameters $a_1 = 0.00123797$ Ha and $a_2 = 2.384$ adjust the pressure behavior at densities ~ 1 g.cm^{-3}.

III.4 Interpolation and further adjustments

Our continuous interpolation between the liquid and plasma regimes reads:

$$F^{ex}(\rho, T) = w(\rho, T) F_{liq}^{ex} + [1 - w(\rho, t)] F_{pl}^{ex} \tag{5.11}$$

where

$$w(\rho, T) = \frac{1}{1 + (c_1 \rho + c_2 T)^4} \tag{5.12}$$

with $c_1 = 0.4$ cm^{3}g^{-1} and $c_2 = 90$ Ha^{-1}.

With the free energy $F^{id} + F^{ex}$ described above, the derivative with respect to the volume fits the tabulated pressures P; however, the energy still reveals a difference from the data, which can be corrected with the following form:

$$\frac{U_T}{N_i} = \frac{2 b_1 \tau - b_2 \tau^2}{1 + \tau^2} - b_3 + \frac{2.5 k_B T}{1 + (0.019\tau)^{5/2}} \tag{5.13}$$

where $b_1 = 0.0069$ Ha, $b_2 = 0.0031$ Ha, $b_3 = 0.00558$ Ha, and $\tau = T/T_c$, where $T_c = 647$ K is the critical temperature. The corresponding free energy contribution is

$$\frac{F_T}{N_i} = -b_1 \tau \ln(1 + \tau^{-2}) + b_2 \tau \arctan \tau + b_3 + k_B T \ln[1 + (0.019\tau)^{-5/2}] \tag{5.14}$$

The approximations to the pressure and internal energy, described above, allow one to add a term $-TS_0$ to the free energy, where S_0 is a constant entropy shift. The value $S_0/N_i = 4.9 k_B$ provides the best fit (within 10%) with the results presented by Soubiran & Militzer [**?**].

Finally, the fit is represented in Figure (5.10) for the pressure, Figure (5.11) for the energy and Figure (5.12) for the Helmholtz free energy. The comparison with the OFMD calculations is displayed in Figure (5.13), showing that we reached the degenerate electron gas limit and that the fit can be used at higher densities without further numerical guiding.

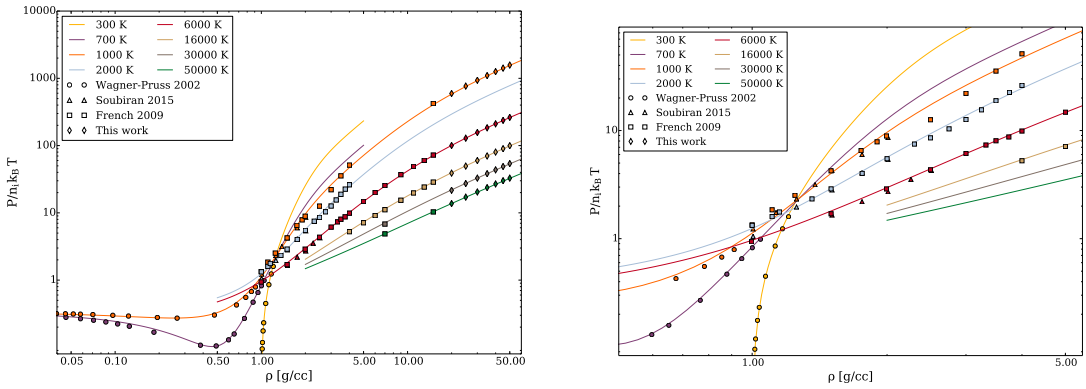

(a) Over a large density range (b) Zoom on the central region

Figure 5.10: Pressure isotherms for our fit and numerical data.

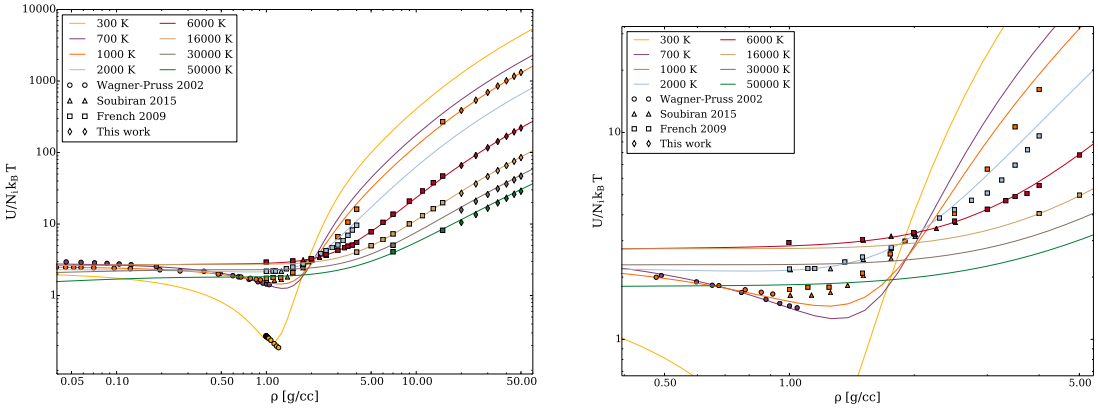

(a) Over a large density range (b) Zoom on the central region

Figure 5.11: Energy isotherms for our fit and numerical data. The energy reference has been shifted by 4.78 eV/nucleus to correspond to Wagner & Pruss.

III.5 Comparison with previous packages

In order to visualize our new EOS for water, we can display a few isotherms compared with the ANEOS package.

It is clear in Figure (5.14) that our new fit is a significant improvement over the previous EOSs available for planetary interior modeling. It appears that the ANEOS EOS overestimates the pressure and the energies at high densities.

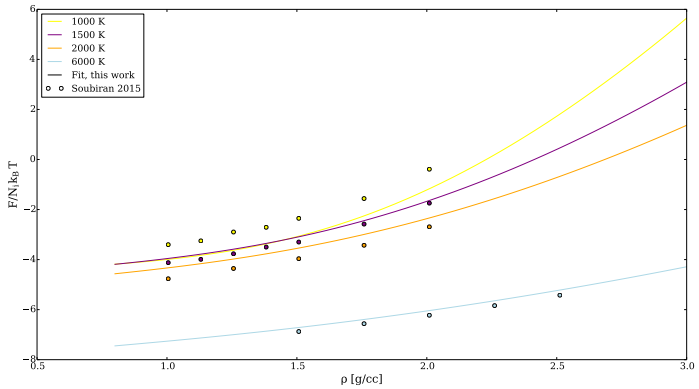

Figure 5.12: Free energy isotherms for our fit compared to numerical data from Soubiran. The same energy shift applies as in Figure (5.11).

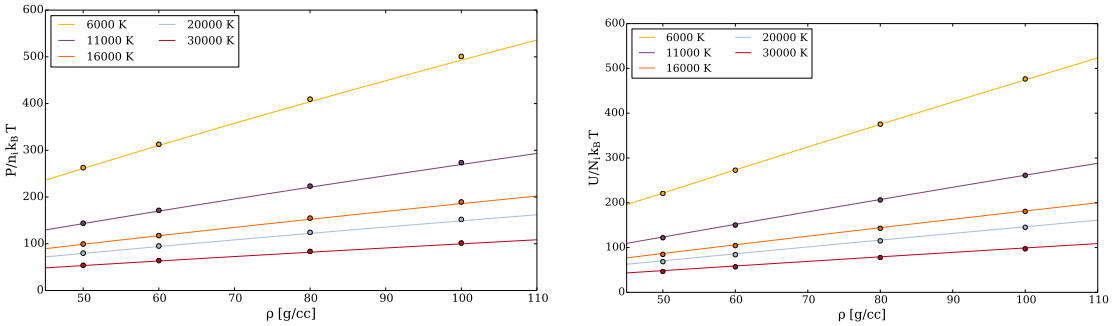

(a) Pressure (b) Energy

Figure 5.13: Comparison between the fit and our OFMD calculations in the very high density region

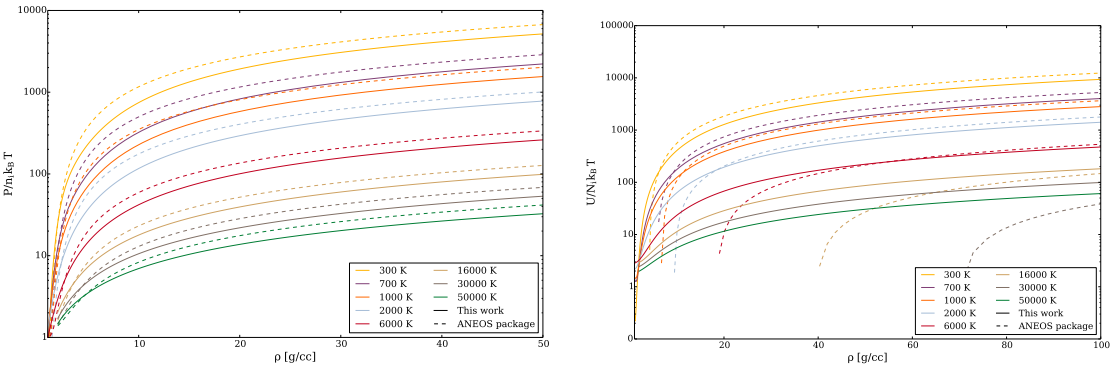

(a) Pressure (b) Energy

Figure 5.14: Comparison between the fit and the ANEOS package.

IV Testing the equation of state: comparison with water shock experiments

A good experimental test for a numerical equation of state is the Hugoniot curve computing: indeed, shock experiments are the most efficient ones when the aim is to reach high pressures. The basic ideas and underlying physical equations are presented in Appendix B. In the case of water, many experiments have been conducted, and we

are going to confront our fitted EOS to them. It is important to notice that our EOS is, in the pressure range of experimental data, based on the work by French *et.al* in 2009: in consequence, any discrepancy between his and our prediction is introduced by the fitting formula.

IV.1 Principal Hugoniot curve

The most widely available shock curve is the principal Hugoniot curve, that is to say the Hugoniot starting at usual pressure and temperature conditions. The measurements have been performed with a wide range of experimental setups, like light gas-guns flyer impactor shock [**?**], laser-driven shocks [**? ?**] or magnetically accelerated flyer-plate shock [**?**].

The predicted Hugoniot is compared to these data points and to other predictions - ANEOS [**?**], SESAME [**?**] and the Hugoniot directly computed by French *et.al* [**?**] - in Figure (5.15). It can be seen that our fit corresponds to the latest data by Knudson *et.al* in 2012 and Kimura *et.al* in 2015, as well as the lower-pressure data from earlier work. The Celliers *et.al* (2004) data shows a significantly higher compressibility and is more consistent with the SESAME model database. Our fitting formula seems correct in this region of the (ρ, T) plane, and perfectly reproduces the data from Knudson [**?**]. However, since our fit is design to reproduce the French DFT dataset in this region, it does not give any new insight to know which experimental data between Knudson and Celliers is the most reliable one. On the other hand, since both Knudson and Kimura are coherent with French and our fit, it indicates that the Celliers results may need a reinterpretation; the discrepancy could stem from the aluminium standard used in their impedance-matching technique, since they used the SESAME data.

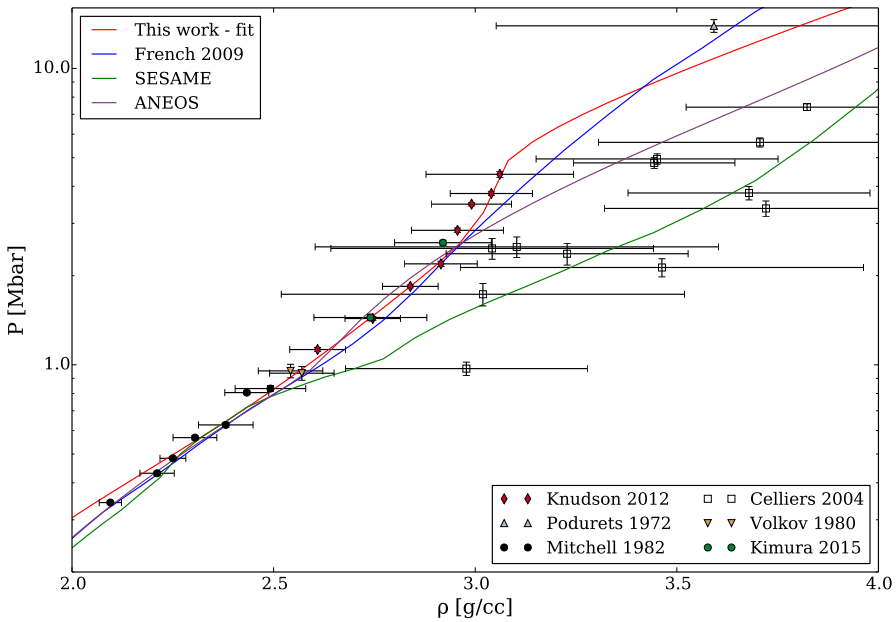

Figure 5.15: Comparison of our fit with experimental data and other theoretical work along the principal Hugoniot curve. The data are taken from refs [**? ? ? ? ? ?**]

IV.2 Reshocked Hugoniot curve

In a 2012 experimental paper, Knudson *et.al* 2012 [**?**] reshocked the water from a first state to a higher-pressure state. The shock wave reached the rear quartz window of the setup and was reflected back into the water to high pressure states up to 7 Mbar. In such a case, the achievable loci after reshock on a given material - in our case, quartz - can be computed from a theoretical EOS and compared to experiments. This case is presented in Figure (5.16). It can be seen that the fitting formula is less efficient in this thermodynamic region.

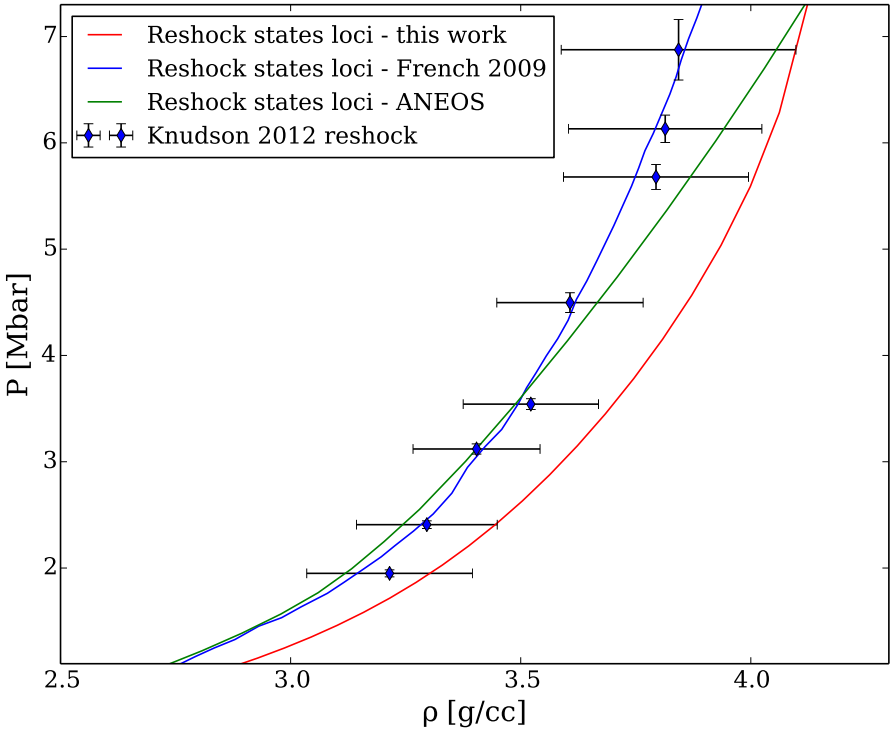

Figure 5.16: Prediction of reshock states loci for a reshock experiment.

IV.3 Precompressed Hugoniot curves

In order to achieved colder points, it is possible to statically precompress the sample to higher pressures - typically 0.5 to 1 GPa - before shocking it. The corresponding Hugoniot curves are found at significantly lower pressures and temperatures for the same densities. For water, two main papers have been published - by Lee in 2006 [**?**] and Kimura in 2015 [**?**]. Their results and the prediction from our numerical fit is in Figure (5.17).

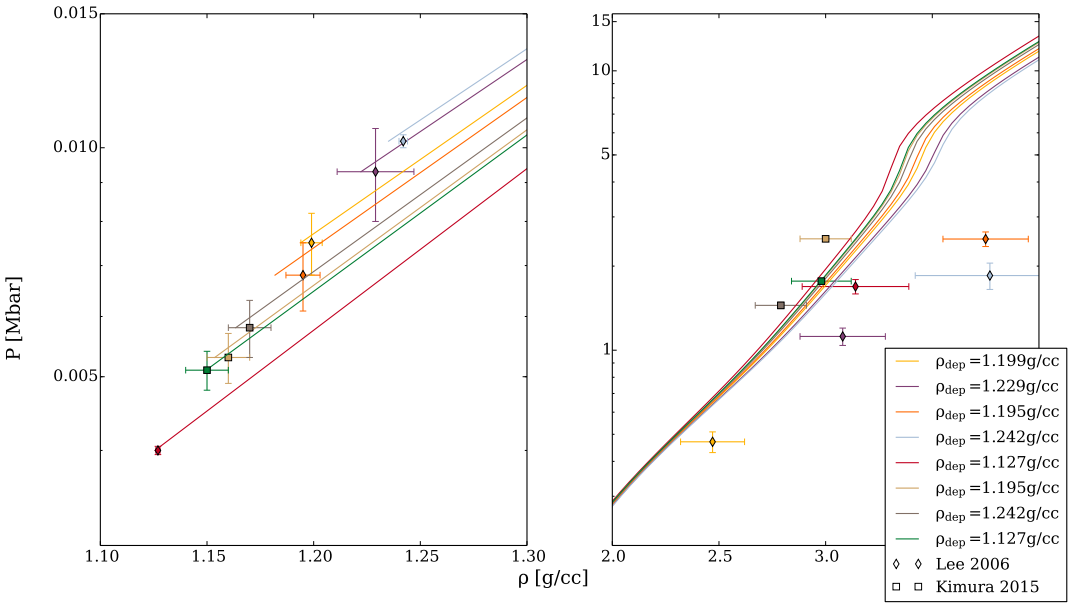

Figure 5.17: Precompressed shock experiments.

It can be seen that our fit is in better agreement with Kimura than with Lee, whose data is more compressible. Since there is no clear consensus on this region of the (ρ, T) plane experimental data, our fit is in sufficiently correct agreement with this kind of experiment.

V Conclusion

We have extended the available EOS for water at very high densities, in order to provide a more reliable EOS at very high pressures for extrasolar planetary models. We then used our numerical extension of the tabulated EOS to design a free energy fit based on the degenerate electron gas limit. This fit provides an estimate of the specific entropy, which can otherwise only been accessed via very costly computations. In the region of interest for the solar icy giants, the derived free energy is consistent with the only previous work in the literature. It can be supplemented with the solid phases fit from [**?**] and the very low density chemical model from [**?**].

A limit of our analytical fit is the treatement of both the fluid and superionic phases with a single fitting formula. This was justified in our approach since the transition seems to lead to few modifications in the thermodynamic properties - or, at least, these modifications were still greater than the uncertainties imposed by the choice of DFT calculations. In contrary, a two-phases fit would be necessary if one wanted to compute

properly the superionic-fluid transition line, or to estimate the conductivity and other transport properties in icy water.

However, proper models for planetary interiors need not an equation of state for pure water, but for "ices" - a mixture of water, ammonia and methane. In the next chapter, we are going to provide numerical EOS for both ammonia and methane.

Chapter 6

Ammonia and methane: the other components of planetary "ices"

Contents

I Ammonia 77

I.1 Known phase diagram and EOS 77

I.2 Method of construction for our equation of state 78

I.3 High-density equation of state 79

II Methane 82

II.1 Previous work 82

II.2 The polymeric phase 82

II.3 Methods for our calculations 82

II.4 High-density phase diagram 83

III Conclusion 86

As we have seen previously, water is a well-studied component of Jovian planets. The case of the other "ices" components is less well-known. If ammonia also shows a superionic (SI) phase - predicted by Cavazzoni *et.al* in the same work as for water [**?**], its boundaries are less well-known and the precise EOS remains to be computed.

In this section, we will only provide DFT calculations for relevant planetary interiors.

I Ammonia

I.1 Known phase diagram and EOS

The phase diagram of ammonia under 2500 K is well known from both static compression experiments - with Raman spectroscopy, infrared absorption or X-rays diffraction as analysis tools - and DFT simulations. We can gather the recent work from Ninet *et.al* [**?** **?** **?**], Ojwang [**?**] and Bethkenhagen [**?**] to create a quite accurate picture of this low-temperature phase diagram. It can be seen in Figure (6.1) that there is no clear consensus about the exact location of the phase boundaries, but the implied phases are correctly known and the transition curves rather well identified. A noticeable point is that the superionic (SI) phase is now admitted to start at as cold as 700 K, colder than the first estimate by Cavazzoni around 1200 K, and colder than the water SI phase ($\sim$ 1500 K).

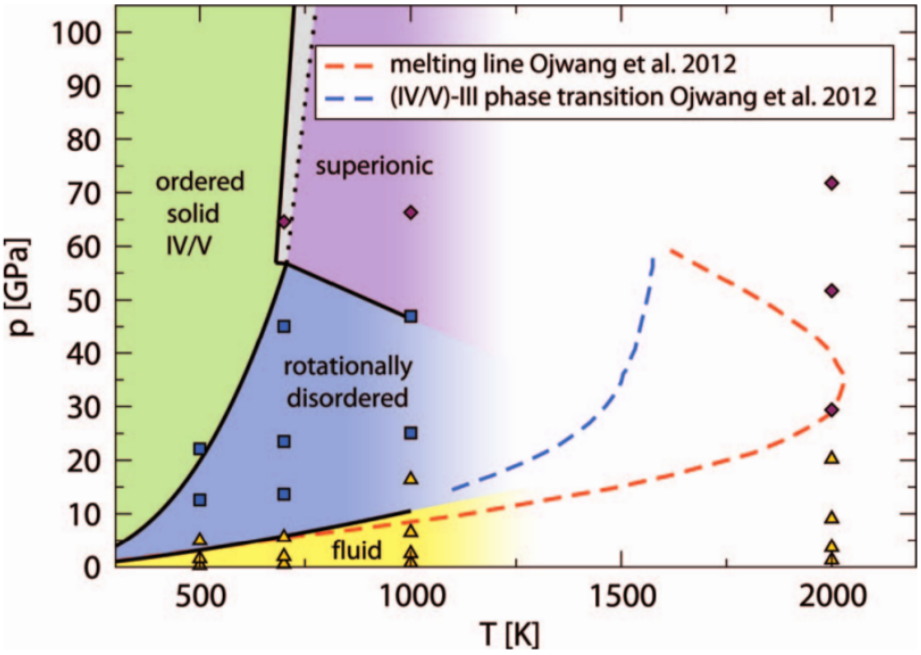

Figure 6.1: Phase diagram taken from [**?**]. The colored areas represent the boundaries by Ninet *et.al* , the dashed lines are the boundaries by Ojwang and each colored dot represents a simulation point from Bethkenhagen.

However, higher temperatures are less well known. Apart from the numerical work by Bethkenhagen, there are few available tabulated EOS in the warm dense matter region. At very high densities, the usual ices from the SESAME [**?**] and ANEOS [**?**] packages are the only option.

We tried to extend the knowledge of the ammonia EOS up to 15 g·cm^{-3}, in a manner comparable with the work performed by French on water. We used once again

the ABINIT [**?** **?**] package.

I.2 Method of construction for our equation of state

Used pseudopotentials

We again created the pseudopotentials using the ATOMPAW code [**?**] with GGA-PBE exchange-correlation functional. The hydrogen pseudopotential was the same one we used for water calculations. The nitrogen has been designed with a more smooth radius of 1 bohr. We also tested it by comparing cold curves to the ones obtained with Jollet's pseudopotentials [**?**]. The two first wavefunctions as well as the test is displayed in Figure (6.2)

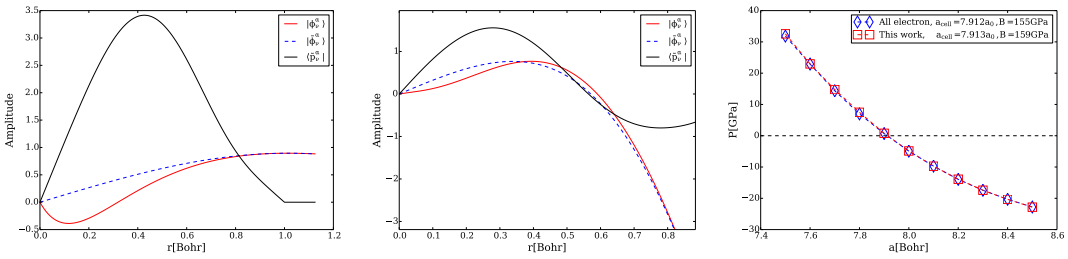

(a) 1s orbital (b) 2s orbital (c) Cold curve test

Figure 6.2: Nitrogen pseudopotential

Convergence tests

We give more details about the convergence tests here. Our convergence in terms of cell size and k-points differs from Bethkenhagen. We tried various possible crystal lattices. We give the example of the point at 3000 K, 3 g·cm^{-3} in Table (6.1). It can be seen that 32 molecules are not enough to ensure convergence at better than 1.5%, even at the Baldareschi point. In consequence, we chose to conduct our simulations with 54 ammonia molecules. As for water, we are more interested in providing a tabulated EOS for planetary interior calculations than establishing the correct SI lattice. Moreover, the thermodynamic quantities show little variation depending on the lattice, so that we use the lattice that corresponds to our convergence requirements.

K-point	# molecules	E (eV/nucleus)	P (GPa)	Phase stability
Γ	32	-78.225 ± 0.036	259.1 ± 4.8	unstable
Baldareschi	32	-78.255 ± 0.025	256.6 ± 3.7	FCC SI
Γ	54	-78.242 ± 0.019	249.2 ± 2.9	BCC SI
Baldareschi	54	-78.282 ± 0.039	250.1 ± 3.5	BCC SI
Baldareschi	64	-78.279 ± 0.017	250.6 ± 1.5	FCC SI
Γ	108	-78.266 ± 0.012	248.6 ± 2.1	FCC SI
Baldareschi	108	-78.245 ± 0.004	250.2 ± 1.2	FCC SI

Table 6.1: Numerical value for ammonia EOS from DFT calculations. Densities are given in g·cm^{-3}, temperatures in K, pressures in GPa and energies in eV/atom.

Analysis method

As for water, we used mean square displacement and visual representation of the trajectories to identify the system's phase.

We find that the SI phase stays stable at higher temperatures than predicted by Bethkenhagen. It can be seen from the trajectory plots in Figure (6.3) as well as the pair distribution function in Figure (6.4) that ammonia is still stable at 5000 K, whereas Bethkenhagen found the transition between 3000 and 4000 K.

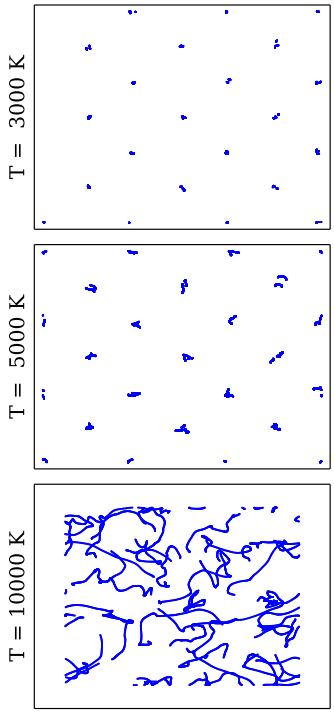

Figure 6.3: Trajectories of nitrogen atoms

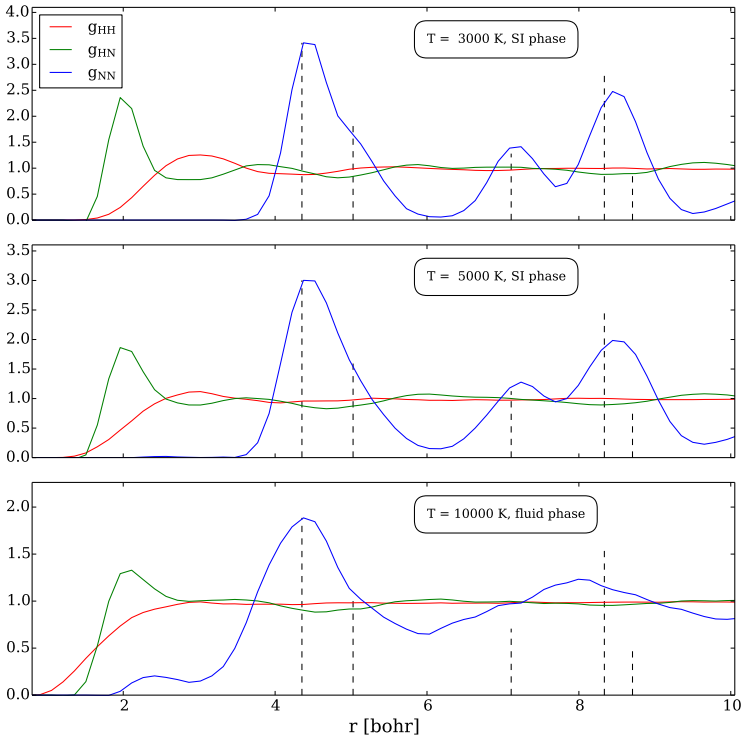

Figure 6.4: Evolution of the PDF with temperature at $\rho = 3$ g·cm^{-3}

I.3 High-density equation of state

We show our EOS in the (P, ρ) and (U, ρ) planes on Figure (6.6) and Figure (6.7), compared to the ANEOS package results for ice [**?**]. Our numerical table is available in Appendix C.

We can show a qualitatively similar behavior between our work and the ANEOS package at high densities, however these two EOS are not quantitatively equivalent, and moreover the low-density region shows a big discrepancy. The difference between ANEOS and our energy calculations also increases with temperature. However, we can see from the computations at $2 - 3$g/cc that our DFT calculations are in complete agreement with Betkenhgen both pressure and energy-wise. We conclude that the previously used ANEOS package is not very reliable, particularly in the typical range of Uranus or Neptun models.

Finally, we present the new phase diagram on Figure (6.8), including Bethkenhagen's simulation (shown by crosses) and with our transition line between the SI and plasma phases.

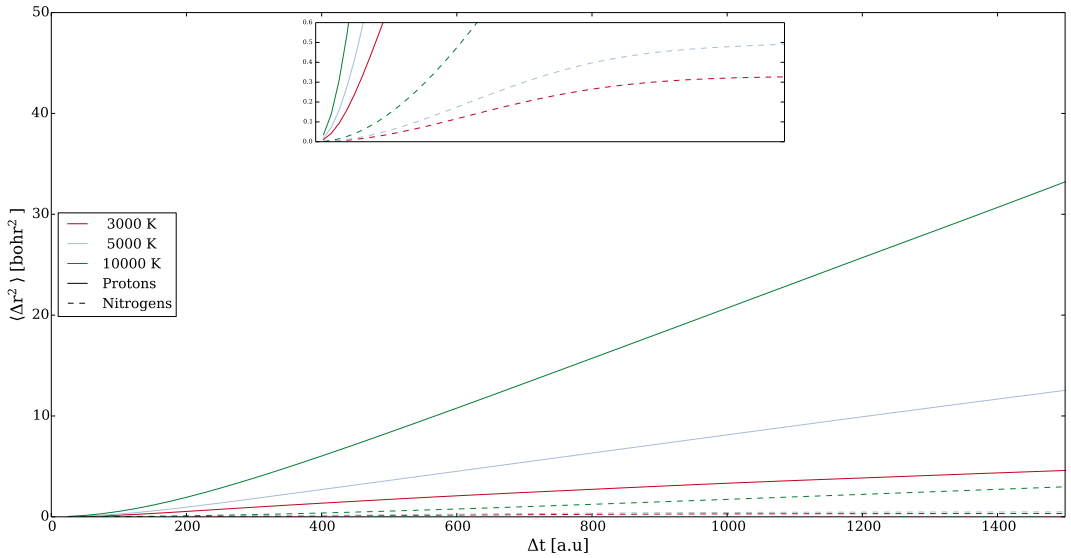

Figure 6.5: Mean-square displacements along the $\rho = 3$g/cc isochore. It can be seen that the superionic phase extends up to 5000 K.

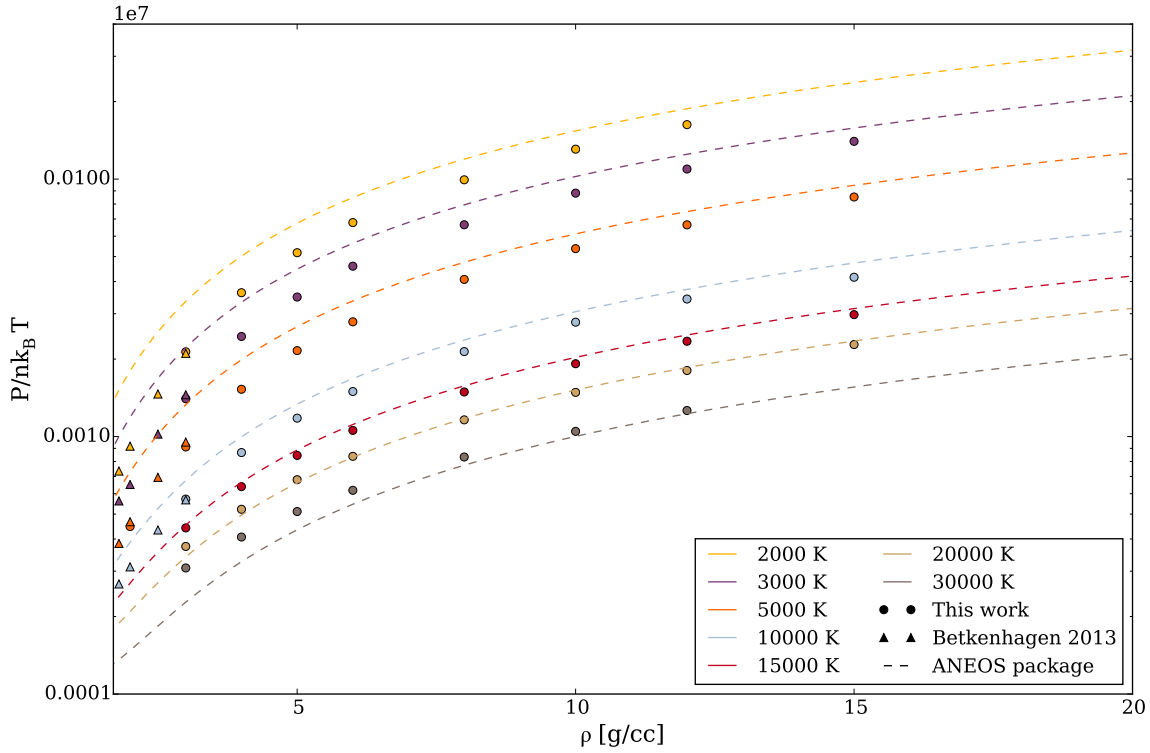

Figure 6.6: Extended (P, ρ) diagram for ammonia, gathering our results and the data from Bethkenhagen *et.al* [**?**]. Also shown is the computations from the ANEOS package [**?**].

We do not present Hugoniot curves calculations, since our calculations start at $2-3$g/cc, while available experimental publications compress ammoniac up to $1,8$g/cc (see for example [**?** **?**]).

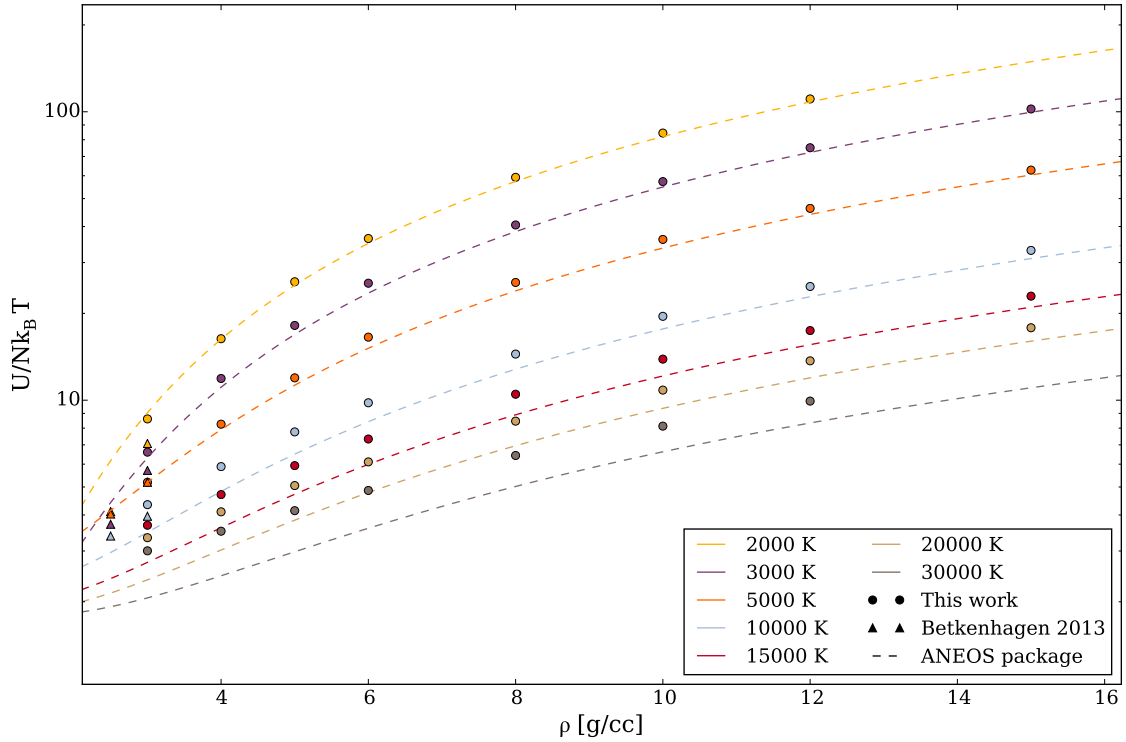

Figure 6.7: Extended (U, ρ) diagram for ammonia, gathering our results and the data from Bethkenhagen *et.al* [**?**]. Also shown is the computations from the ANEOS package [**?**].

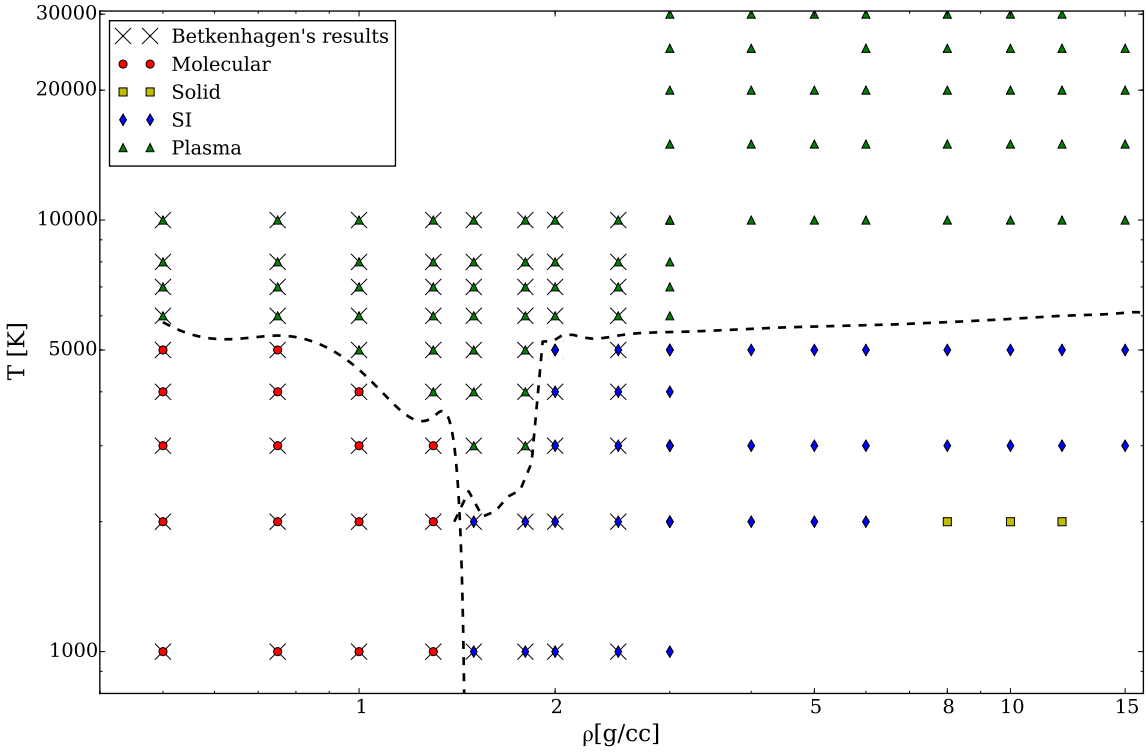

Figure 6.8: Extended phase diagram for ammonia, gathering our results and the data from Bethkenhagen *et.al* [**?**]. We kept our data in the discrepancy zone.

II Methane

II.1 Previous work

The main investigation about methane in planetary science has been conducted by Sherman *et.al* in 2012 [**?**]. Their main finding is that a polymeric phase, in which the carbon atoms arrange themselves into long chains, appears at moderately high density and temperature. The hydrogen atoms are expelled from the carbon chains in this state, preventing the formation of a superionic phase.
We did not have enough time in this work to investigate properly this result, since we would have needed to develop a new analysis tool for carbon chains. We only extended the pressure-temperature domain and analyzed the phase by comparing our probability density function to the ones provided by Sherman *et.al* .

II.2 The polymeric phase

We present here the results from [**?**] about the polymeric phase. All the figures in this section are taken from this paper.

In this polymeric regime, methane molecules dissociate to form long chains with a short lifespan. The authors characterized the polymers by numbering clusters of carbons, defined as chains of carbon atoms closer from each other than a chosen distance (chosen to be 3.40 Bohr radius in this paper). It can be seen on Figure (6.9) that, inside the polymeric phase region, most carbon atoms are in such clusters. The snapshots on Figure (6.11) highlight the dissociation and formation of polymeric chains during the simulation. Finally, the behavior of the pair-distribution function reflects this polymeric state, as can be seen on Figure (6.10) : the characteristic C–H liaison peak decreases while entering the polymeric state, and the C–C peak increases, as can be expected given the dissociation of methane and the formation of polymers.

II.3 Methods for our calculations

Used pseudopotentials

We created and tested a pseudopotential for carbon with the same procedure as in I.2. It has been designed with a 0.95 bohr PAW radius and GGA-PBE functional. The two first wavefunctions as well as the test are displayed in Figure (6.12)

Convergence parameters

We made these computations at the Γ point with an energy cutoff of 50Ha and 32 methane molecules. The timestep for molecular dynamics is chosen to be $0,12$fm. We found that these convergence parameters lead to pressure convergence at better than 1%.

Identifying the polymeric state

We did not have enough time to develop a cluster analysis tool in our simulations, such as in [**?**]. However, we can use the pair-correlation functions to identify a similar behavior, and the presence of the polymeric phase will be deduced from this only criterion. As can be seen on Figure (6.13), we find the same behavior as [**?**], with the

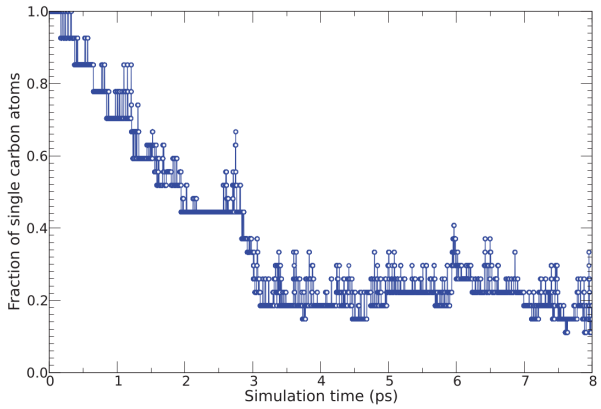

Figure 6.9: Evolution of fraction of single carbon atoms during the MD simulation at 4000K and 1.2g·cm^{-3} . The decrease measures how many methane molecules polymerize to form long carbon chains, which is illustrated in Figure (6.11). Taken from [**?**]

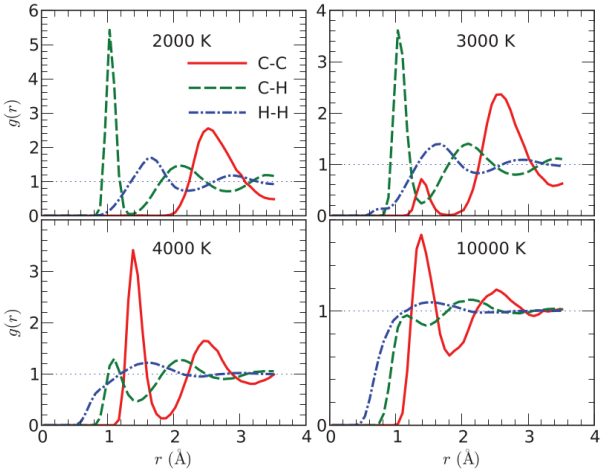

Figure 6.10: Pair correlation functions, $g(r)$, between different nuclei as a function of temperature at a density of 2.0g·cm^{-3}. The intramolecular C–H and H–H peaks disappear as CH_4 molecules dissociate with increasing temperature, while the intensity of the C–C peak rises with increased polymerization and then drops again as a plasma state is reached at 10 000 K. Taken from [**?**]

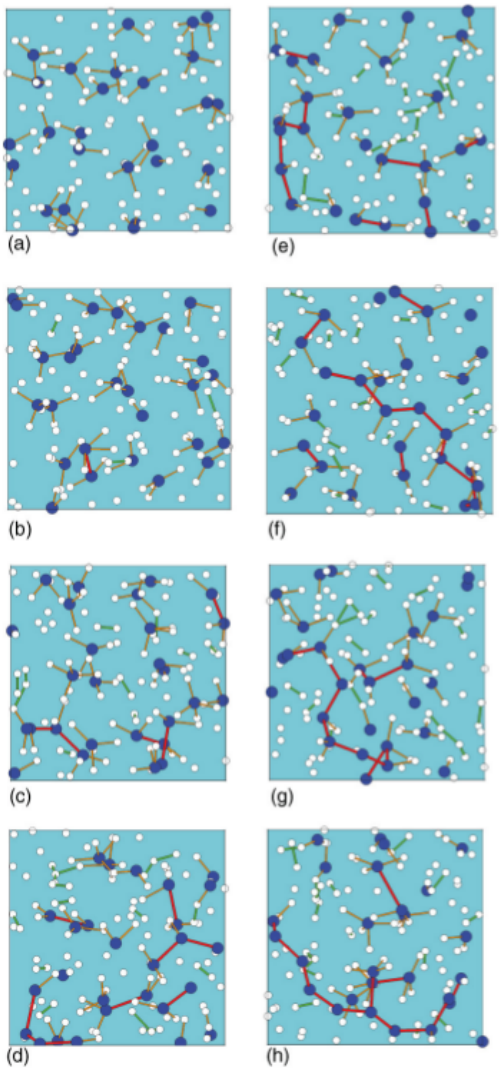

Figure 6.11: Series of snapshots from MD simulations at 4000K and 1.2g·cm^{-3}. The large and small spheres depict the carbon and hydrogen atoms, respectively. The C–C, C–H, and H–H bonds are illustrated by dark thick lines, thin lines, and thick light lines, respectively. Taken from [**?**]

typical intramolecular C–H peak decreasing while going through the polymeric, then fluid plasma phase.

II.4 High-density phase diagram

We present the results of our computations in the (P, ρ) and (U, ρ) planes on Figure (6.14) and Figure (6.15), compared to the ANEOS package results for ice [**?**]. The numerical EOS table extracted from our simulations is available in Appendix C.

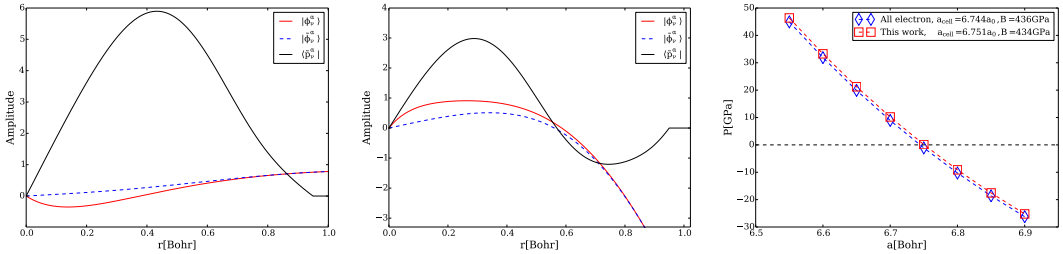

(a) 1s orbital (b) 2s orbital (c) Cold curve test

Figure 6.12: Carbon pseudopotential

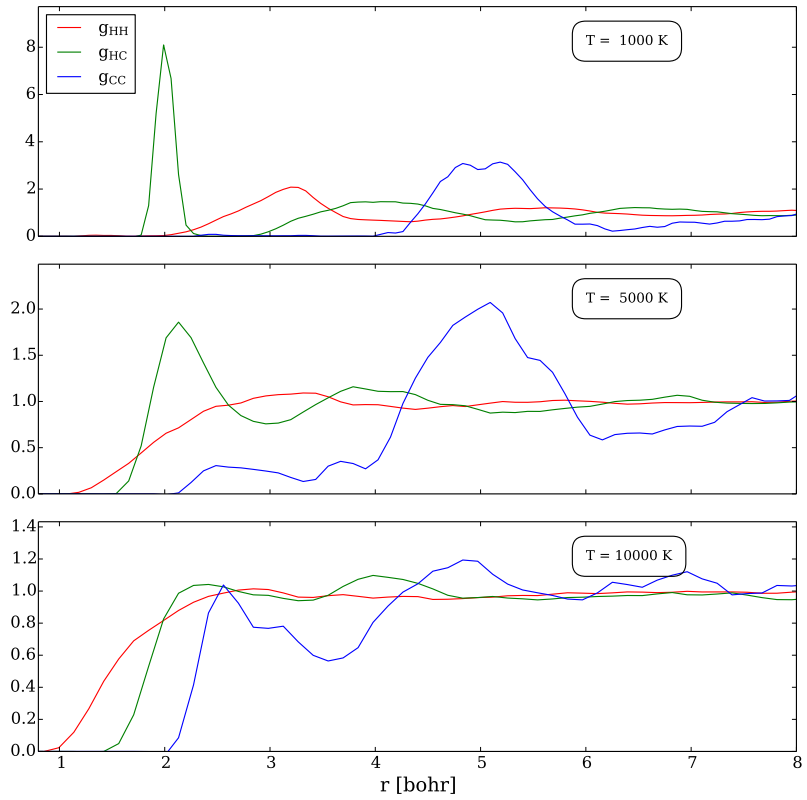

Figure 6.13: Pair-distribution function along the 2 g/cc isochore

In this case, our data is in strong disagreement with the ANEOS package, and in very good agreement both pressure and energy-wise with previous DFT calculations. We can conclude that our EOS is probably a good estimate for a high-density regime extension, and that the ANEOS package is too simple for nowadays applications.

As previously stated, we identified the various phases (especially the polymeric state) on the sole pair-distribution function shape. Relying on this only criterion, we find that the polymeric phase extends at higher density ; the computed phase diagram for WDM methane can be found on Figure (6.16).

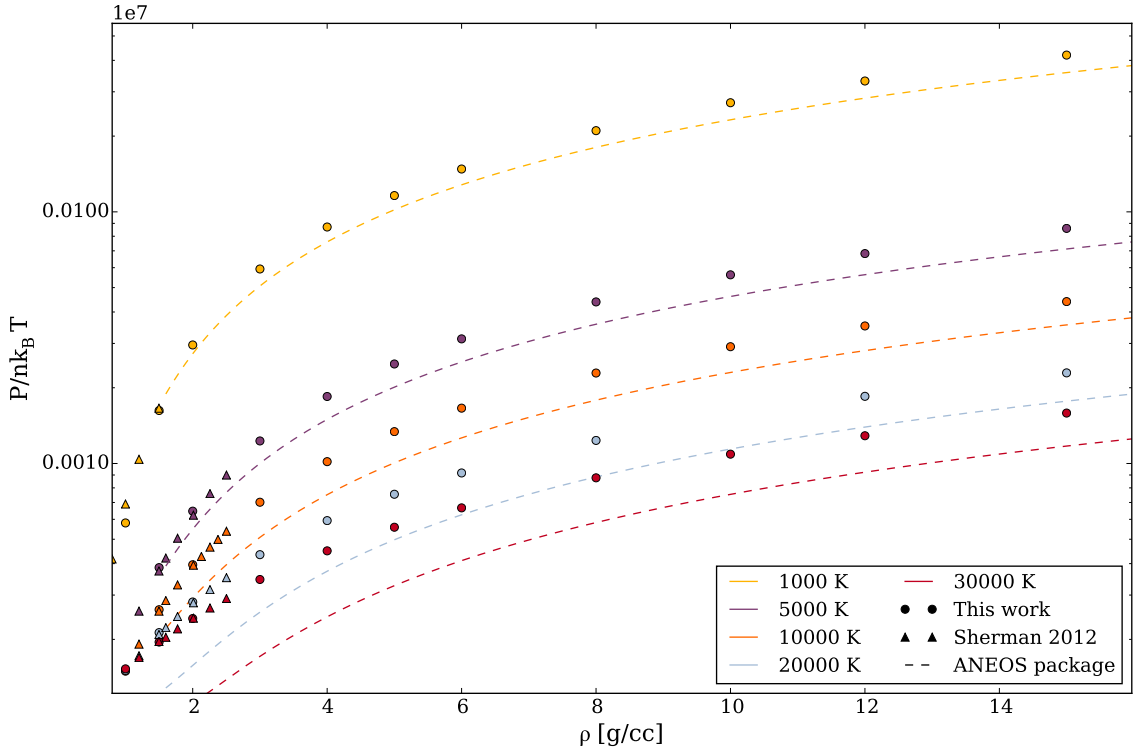

Figure 6.14: Extended (P, ρ) diagram for methane, gathering our results and the data from Sherman *et.al* [**?**]. Also shown is the computations from the ANEOS package [**?**].

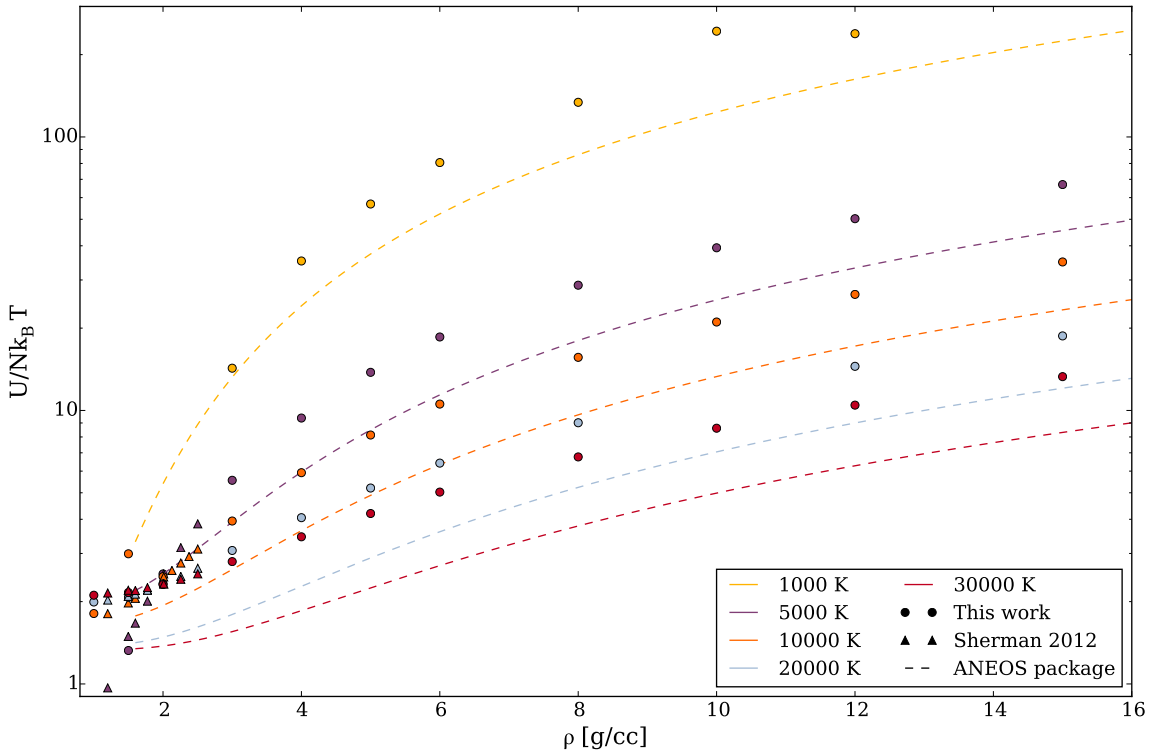

Figure 6.15: Extended (U, ρ) diagram for methane, gathering our results and the data from Sherman *et.al* [**?**]. Also shown is the computations from the ANEOS package [**?**].

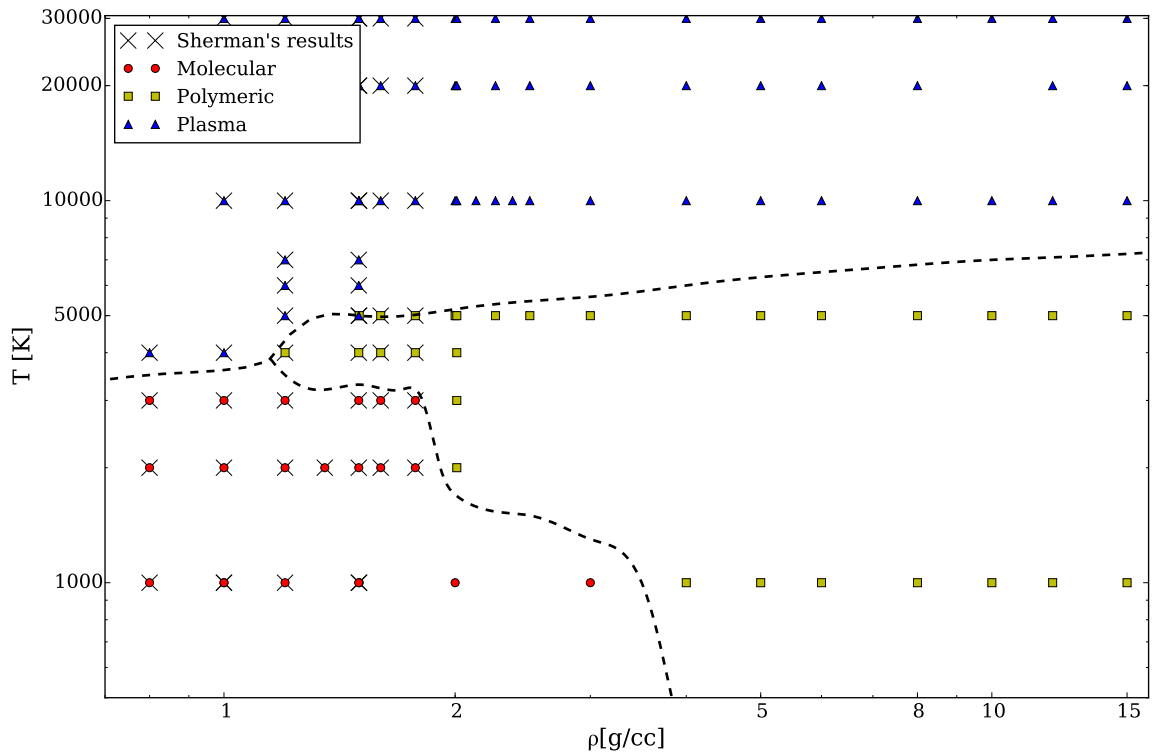

Figure 6.16: Phase diagram for methane, gathering our data and the work by Sherman *et.al* [**?**]

III Conclusion

In this chapter, we extended the knowledge of the phase diagram for ammonia and methane at higher densities than in previous literature, up to Jupiter-like conditions.

We confirmed the existence of the superionic phase for ammonia, and its extension at high densities. In these calculations, we showed that the ANEOS package was not confirmed by DFT calculations. Although the calculations we performed did not reach the Thomas-Fermi limit, it seems reasonable that the water-ammonia mixture can be, in a first attempt of description, be described by pure water, or the ideal mixing law.

On the other hand, methane shows a very different behavior. The superionic phase has not been observed, but instead a polymeric phase appears in roughly the same region ; however, its microscopic properties will probably turn out to be radically different from the superionic water or ammonia, particularly if we consider the conductivity.

It is clear from this work that the correct system to be studied for planetary models is the water-methane-ammonia mixture instead of any of them separately. The mixture may present highly complex phase behavior in the icy giant's regime, since many phases are present for each pure components. If some hugoniot experiments on "synthetic Uranus" have already been conducted [**?** **?**], a theoretical ab initio computation for such a system may be too consuming for present calculation capabilities. In the near future, it will be possible to use the ideal mixing law as a first mean of computing this mixture's thermodynamical properties.

Part III

Phase diagrams for White Dwarf Stars

Chapter 7

A brief overview of white dwarfs and their cooling

Contents

I Introduction: white dwarfs and implications 91

I.1 Definition and orders of magnitude 91

I.2 Surveying the white dwarfs 92

II Cooling theory of white dwarfs 94

II.1 Basic assumptions 94

II.2 The equations of cooling white dwarfs 95

II.3 Quantum effects in very dense white dwarfs 96

III Conclusion 96

White dwarfs are the most common stellar remnants in the observable universe, as they are issued from less-than-$6M_\odot$ stars. They also are the lighter "compact stars", which include other stellar remnants like neutron stars or black holes. Since they are not heated up by nuclear reaction anymore, they cool as they radiate their energy, and their luminosity can be related to their age, therefore estimating the age of the older objects in the galaxy.

In this chapter, we are going to review the basic physics of white dwarfs, and their cooling history. We will show how the knowledge of their crystallization process is crucial to correctly estimate their age, providing a motivation for studying this process. Specifically, white dwarfs mainly consist of a carbon-oxygen mixture, with trace elements such as neon, leading to an important knowledge of binary and ternary mixtures crystallization.

I Introduction: white dwarfs and implications

I.1 Definition and orders of magnitude

History and features

The first white dwarf (WD) was discovered in 1844 as the companion of Sirius. In 1915, Adams [**?**] found its spectrum to be a hot star spectrum, which led to the conclusion that this object of mass $0.75 - 0.95M_\odot$ had a radius comparable to Uranus's. The extreme density of this object, around $10^5 \text{g}\cdot\text{cm}^{-3}$ was not understandable at the time, since there was no known physical process that could produce a pressure large enough to balance the gravity field. The decisive hypothesis was found by Fowler in 1926 [**?**], who used the newly formulated Fermi-Dirac statistics [1] on degenerate electrons inside the star to explain its equilibrium. In 1931, Chandrasekhar [**?**] integrated relativistic effects and proved that a WD could not exist over a certain mass limit - the so-called *Chandrasekhar mass*, $\sim 1.4M_\odot$ - the pressure of the degenerate electron gas being insufficient to compensate for gravitational forces anymore.

WDs are remnants of under-$6M_\odot$ stars. After the star burned all the hydrogen and helium inside its core, it leaves the main sequence and follows a complex evolution, at the end of which the WD is left. WDs are mainly composed of a dense core of carbon and oxygen - with traces of neon of iron - and a thin hydrogen and helium envelope (see Figure (7.1)). An interesting feature is that, due to the degenerate electron gas' high thermal conductivity, the whole core is nearly isothermal - around 10^7K - and since the Fermi temperature corresponding to the WDs densities is around 10^9K, its pressure is roughly the Fermi gas pressure at zero temperature.

Internal profile and mass-radius relationship

Simple internal profiles and a mass-radius relationship can be obtained with the basic Chandrasekhar theory of WD (see, e.g., [**?**]), which only postulates that the pressure is given by the relativistic degenerate electron gas while the mass is given by the ions; the resulting profiles are shown on Figure (7.2).

For a typical WD, $M = 0.6M_\odot$ and $T = 5 \cdot 10^6$K, leading to a core at $r_s = 1.2 \cdot 10^{-2}, \theta = 1.17 \cdot 10^{-2}, x = 0.8$: the electrons are well degenerated ($\theta < 0.5$ in almost

[1] Formulated by Dirac in 1926 [**?**]

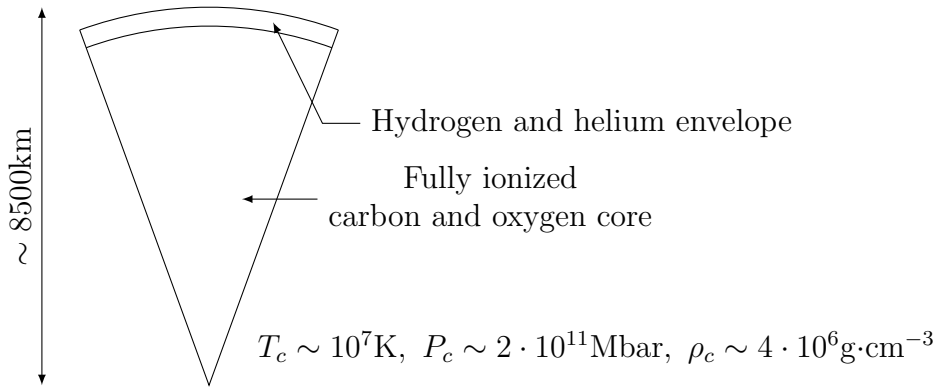

Figure 7.1: Structure of a typical WD: $M \sim 0.6 M_\odot$

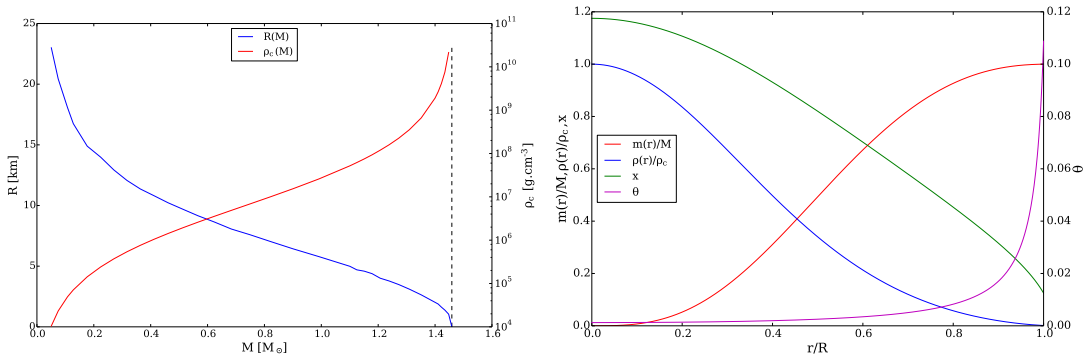

(a) Mass-radius relationship

(b) Profile for a $0.6 M_\odot$ WD at $5 \cdot 10^6$K

Figure 7.2: WD interiors described by the simple Chandrasekhar theory of WD.

the whole star) and relativistic effects must be taken into account in the equation of state ($x \lesssim 1$).

I.2 Surveying the white dwarfs

The mass distribution function

In order to understand formation scenarii, it is useful to estimate through surveys the mass distribution function of WDs - testing a formation scenario using a mass function can be found, e.g., in [**?**]. As can be seen in Figure (7.3), the most common WDs are not concerned by the Chandrasekhar mass limit, since their mass distribution is centered around $0.6 M_\odot$.

The luminosity function: white dwarfs and cosmochronology

Of even more interest is the luminosity function of WDs, that is to say, the mean number of WDs of a given luminosity in a given volume. A brief review of WDs surveys yield the shape on Figure (7.4).

The luminosity function is a key observable of WDs, not because it gives us insight on the repartition of these stars, but because it is directly related to their age distribution. Indeed, a WD is a star remnant: the major source of heating in a star - the nuclear reactions - do not play a role anymore, and the WD is a constantly cooling object. In consequence, the fainter the WD, the older it is. The end of the luminosity function seen in Figure (7.4) around $\log(L/L_\odot) \simeq -4.5$ can be interpreted as the

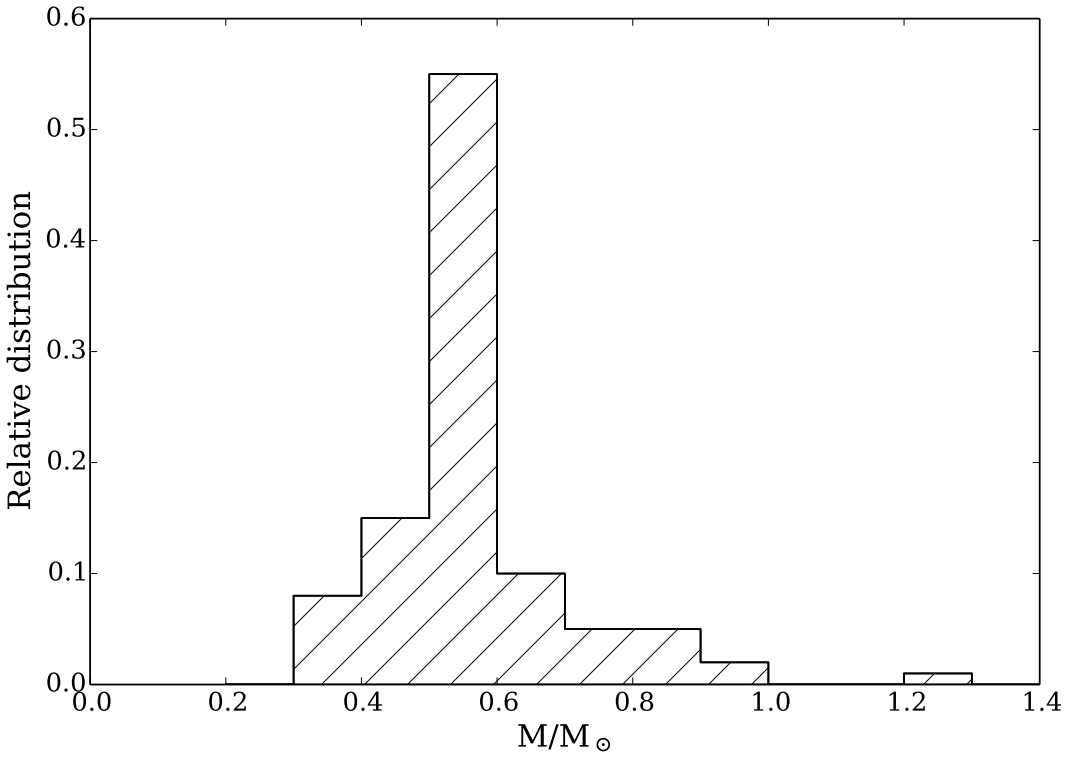

Figure 7.3: Mass distribution of WDS (from [**?**], but other surveys such as [**?**] yield similar results)

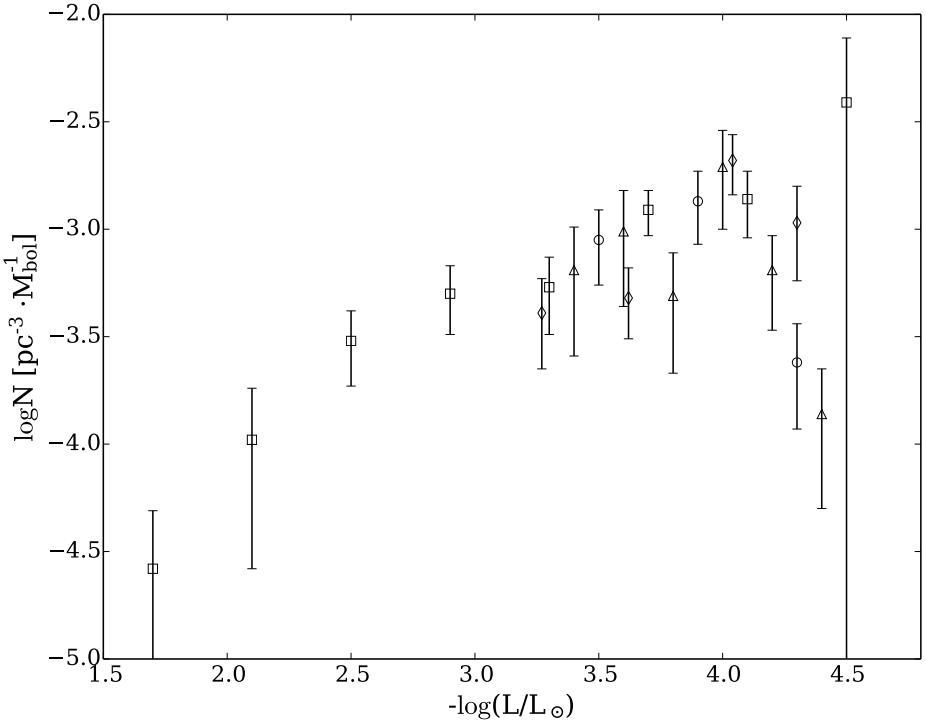

Figure 7.4: Luminosity function observations from [**?**] (circles), [**?**] (squares), [**?**] (triangles) and [**?**] (diamonds)

oldest WD. An accurate cooling theory of WDs then permits to estimate the age of

these older objects, and in consequence the age of the galaxy. This use of WDs as cosmochronometers was first suggested in 1959 by Schmidt [**?**], and concretely applied in 1987 by Winget *et.al* [**?**] for the first time. A review of WDs cosmochronology and its concrete applications can be found in [**?**]. One of the main difficulties of this approach is now to have a reliable cooling theory for white dwarfs, which will be introduced in the next section.

II Cooling theory of white dwarfs

II.1 Basic assumptions

The basic theory of WD cooling was proposed by Mestel in 1952 [**?**] and was based on four simple assumptions:

1. the temperature field is uniform throughout the core, due to the electron gas' high electrical conductivity;
2. only photons are considered in the energy loss, and the radiative transfer equation in the envelope is solved using the simple Kramers' opacity law [**?**];
3. the only energy source is the thermal internal energy;
4. since the heat capacity of the degenerate electron gas is small ($c_v/k_B = \pi/2\theta$), the heat capacity of the core is the one of the ions - assumed to be a perfect gas in this model.

This simple model leads to a luminosity function $N \sim L^{-5/7}$, which is plotted in Figure (7.5). It can be seen that it is in correct agreement with the calculation until the $\log(L/L_\odot) = 4.5$ cutoff, and these four basic ingredients are the core physics of WD cooling theory.

However, many aspects can be improved. The second point has been revisited both by taking the neutrinos' energy loss into account - the photon's luminosity becomes dominant only after 10^7 years of cooling - and by using more accurate envelope models opacity.

The two last hypotheses have been much revisited, and are the ones which interest us in this work. First of all, the gravitational energy of the WD has been taken into account. Second, the equation of state (EOS) of the perfect ionic gas has been replaced with more accurate EOS of the ion-electron mixture, the so-called One-Component-Plasma (OCP) EOS, which is composed of one type of ions immersed in a neutralizing homogeneous electronic background. Of course, polarization effects on the electron gas are not taken into account in this model, but due to the high degeneracy of the electron gas inside a WD, it is a reasonable first approximation which takes into account the Coulomb effects. The classical OCP has the interesting property to be entirely determined by the sole parameter Γ as defined in the Chapter 1.

The OCP has been studied extensively with both theoretical and numerical approaches [**?** **?** **?** **?** **?**], and has quickly been shown to undergo a solid-liquid phase transition at $\Gamma \sim 175$. This transition leads to a latent heat release which is responsible for a cooling delay. However, these cooling theories provided an estimated age of the galaxy of 7.5 to 11 Gyr, while the observation of globular clusters - which was used independently for the same purpose - lead to an estimation of 15 Gyr. Segretain and Chabrier suggested in 1994 [**?**] that the crystallization of the OCP was not as simple

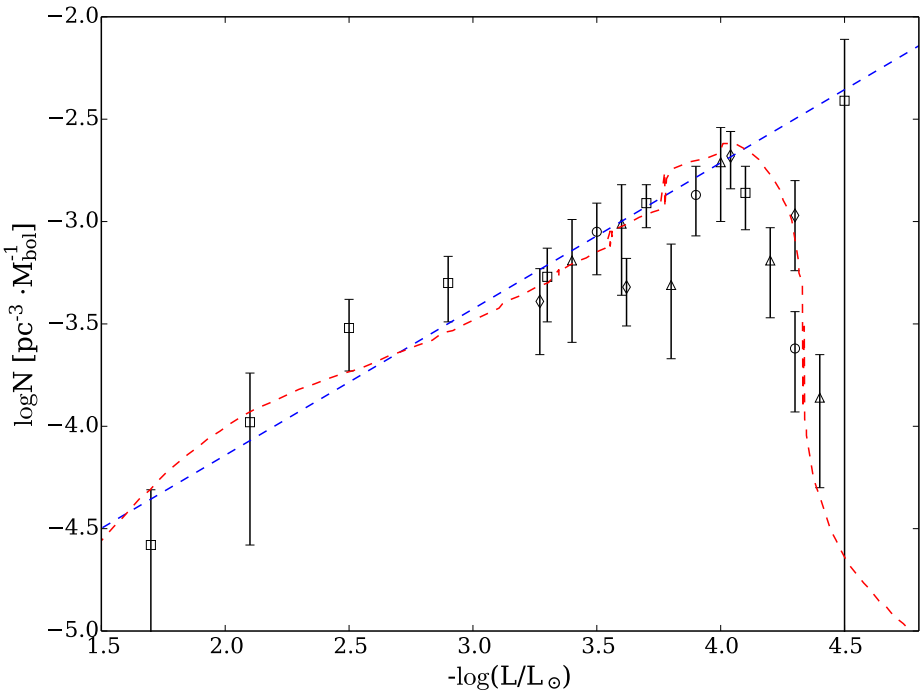

Figure 7.5: Luminosity function observations on Figure (7.4) compared to theoretical models: blue, Mestel theory; red, more elaborate approach with Coulomb effects and sedimentation (taken from [**?**])

in a WD, since they are composed of ionic *mixtures*, which can lead to a sedimentation process at the transition, and consequently to a complementary gravitational energy release.

II.2 The equations of cooling white dwarfs

Let us write the equations related to the upper assumptions. Writing L the luminosity, δq the heat gained by a shell of mass dm during δt, ϵ_ν the neutrino rate per unit mass, u the internal energy per unit mass and Ω the gravitational energy, an energy balance over a period δt gives:

$$L\delta t = -\int_0^M \delta q dm - \int_0^M \epsilon_\nu dm \delta t = -\int_0^M (\delta u + \delta\Omega) dm - \int_0^M \epsilon_\nu dm \delta t \tag{7.1}$$

One can detail du and add the hydrostatic equilibrium, leading to:

$$(L + L_\nu)\delta t = -\int_0^M \left\{ c_V \delta T + (T\frac{dP}{dT})_\rho \delta \frac{1}{\rho} \right\} dm \tag{7.2}$$

in the absence of crystallization, and

$$(L + L_\nu)\delta t = -\int_0^M \left\{ c_V \delta T + (T\frac{dP}{dT})_\rho \delta \frac{1}{\rho} \right\} dm - \int l dm - E_{\delta\rho/\rho} - \int [\sum_i (\mu_i dN_i)_l + \sum_i (\mu_i dN_i)_s]_{\rho,T} dm \tag{7.3}$$

where l is the latent heat, $E_{\delta\rho/\rho}$ is the gravitational release due to density discontinuity at the transition frontier, and the $\sum_i(\mu_i dN_i)$ terms represent the chemical energy from the separation of the two phases at the transition.

Let us just give a few numbers to quantify these effects. The energy given by the latent heat at crystallization of a WD is around:

$$E_c = l_{OCP}M \sim 1.4 \cdot 10^{39} J \tag{7.4}$$

and the sedimentation energy release as:

$$E_s \sim MG\frac{\delta\rho}{\rho}\bar{R} \sim 4 \cdot 10^{39} J \tag{7.5}$$

These effects are of the same order of magnitude. They lead to a supplemental cooling time:

$$\Delta\tau \sim \frac{E}{L} \sim 10^9 yr \tag{7.6}$$

for a WD at $\log(L/L_\odot) = -3.5$. These effects are hence crucial to have a correct estimate of the age of the galaxy. Since the sedimentation process is highly different when the binary mixture diagram changes, this diagram must been known with high accuracy, which will be discussed in the next chapter.

II.3 Quantum effects in very dense white dwarfs

As we explained in Chapter 1, a high density plasma can exhibit a quantum behavior for the ions if the density is too high or the temperature too low. In the case of a WD, the question arises: when in the cooling sequence does the crystallization kick in? Chabrier addressed the issue in 1992 [**?**] and showed that the quantum degeneracy parameter η was larger than one for a typical WD at classical crystallization point. Relying on a simple analytical model for the quantum OCP EOS, he showed in 1993 [**?**] that the quantum effects modified the cooling sequences of the WDs by adding a supplementary specific heat reservoir leading to a longer cooling time. If the effect was only a 5% augmentation of the cooling time in the case of $0.6M_\odot$ WDs, for the massive WDs at $1.3M_\odot$, the cooling time was lengthened by 30%!

In consequence, a more accurate EOS and phase diagram for the quantum OCP would be necessary to compute reliable cooling sequences. However, apart the pioneering analytical work of Hansen and Vieillefosse [**?**] and numerical work of Iyetomi *et.al* [**?**], the most up-to-date work is the numerical work produced by Jones & Ceperley in 1996 [**?**]. They made Path Integral Monte-Carlo computations, and provided an analytical fit for the free energy as well as a phase diagram. However, due to the computational power limitations in 1996, they only relied on small systems of 54 particles. With nowadays' possibilities, a further study of the quantum OCP and carbon-oxygen mixtures would be interesting.

III Conclusion

The luminosity function of WDs is a key ingredient for estimating the age of the galactic disk, as they are among the most ancient stellar objects. However, this determination of their age from the luminosity function requires an accurate knowledge of the cooling process. Many physical phenomena intervene in this cooling, such as the crystallization of the star and the associated sedimentation process.

In the next chapter, we are going to review and construct binary phase diagrams for WD cooling.

Chapter 8

Binary mixtures crystallizing in white dwarfs

Contents

I State of the art 100

I.1 Free-energy calculation diagrams 100

I.2 Direct molecular dynamics 100

II Our plasma mixture simulations 102

II.1 Pair potential between ions: the Yukawa plasma 102

II.2 Numerical strategy 104

III Results and discussion 105

IV Conclusion 109

We have seen in the previous chapter that the binary diagrams of the plasma mixtures are necessary to correctly estimate the effects of the sedimentation. In this chapter, we will review the existing diagrams and explain how we constructed our new numerical diagram from direct molecular dynamics simulations. We will then discuss our results and their implications.

We are going to focus on the effect of binary mixtures of carbon and oxygen, even if lower-abundance elements such as neon may have a substantial influence during the cooling process, as first show by Isern *et.al* in 1991 [**?**].

I State of the art

I.1 Free-energy calculation diagrams

We are going to review a series of diagrams computed from direct comparison of solid and liquid free energies. These free energies are generally obtained through Monte Carlo simulations, Density Functional Theory methods or Hypernetted Chain calculations.

The first diagram was computed by Stevenson in 1980 [**?**] from an analytical Helmholtz free energy model guided by Monte-Carlo simulations; a strong assumption of this model was that there was no order in the solid phase, leading to a coexistence of two pure solids instead of an alloy. The consequence was a eutectic diagram: the freezing temperature for the carbon-oxygen mixture was way below the pure component transition point.

During the late 1980's, another description of the Helmholtz free energy has been more widely used: the free energy of the ions is described as a functionnal of the nuclei density, the difference between the solid and fluid functionnals being second-order terms related to the pair-correlation function in the solid phase. This pair-correlation can be estimated either from hypernetted chain calculations [**?** **?**], Monte-Carlo simulations [**?**] or with the analytical Mean-Sphere Approximation [**?** **?**]. While most authors concentrated on carbon-oxygen mixtures, Segretain and Chabrier [**?**] and Ogata *et.al* [**?**] provided diagrams for arbitrary charge ratio mixtures. These works invalidate the previous eutectic point for the carbon-oxygen mixture, leading either to a spindle or azeotropic diagram (in which the solidus and liquidus meet). These diagrams can be seen on Figure (8.1).

More recently, very accurate parametrizations of the free energy in terms of Γ and charges have been proposed for ionic mixtures, including fine effects such as non-ideal mixing free energy (see, e.g., [**?**]). Medin *et.al* [**?**] used these parametrizations to derive a new "analytic" phase diagram for the carbon-oxygen mixture. It is also shown on Figure (8.1).

It can be seen here that there is no clear consensus about the spindle or azeotropic nature of this phase diagram. Moreover, we can see that the Segretain-Chabrier diagram shows higher melting and freezing temperatures at a given composition than the others, which can lead to substantially different cooling times (see, e.g., [**?**]).

I.2 Direct molecular dynamics

In 2010 and 2012, Horowitz, Hughto, Schneider *et.al* performed large-scale molecular dynamics (MD) of two- and three-component plasma equilibrium [**?** **?** **?**]. They did not use the exact OCP model, but a Yukawa pair interaction - see II.1 for details.

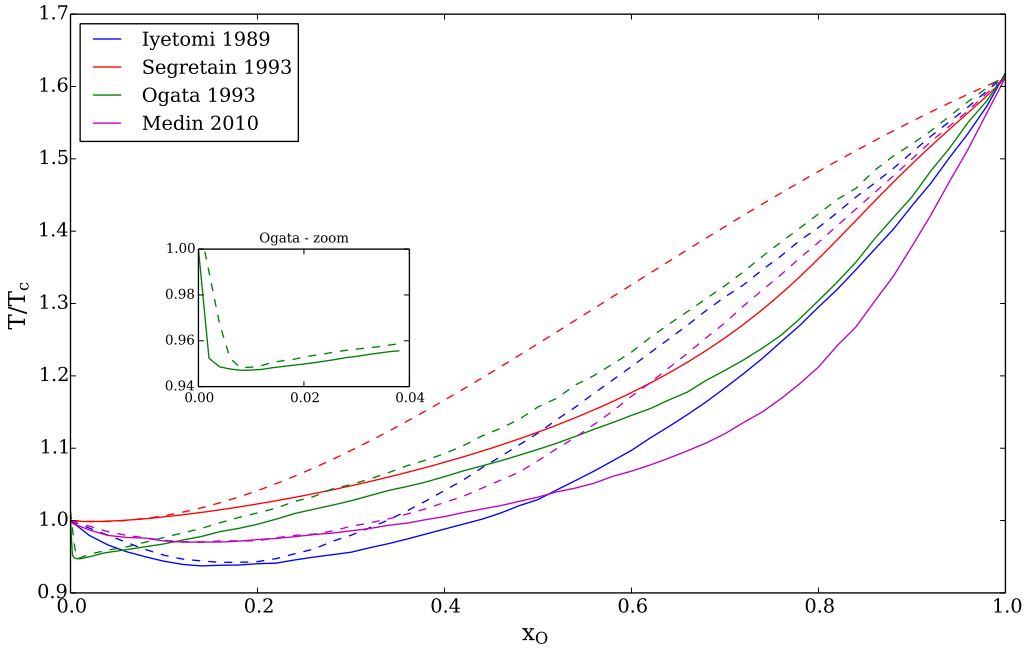

Figure 8.1: Major binary diagrams computed until 2010 for carbon/oxygen mixtures. The full lines are the solidus curves and the dashed lines are the liquidus curves.

The authors performed 27648 and 55296 ions simulations in which the system was made of coexisting liquid and solid phases, a temperature feedback control ensuring the coexistence along the whole simulation:

- each ion is identified as either solid-like or liquid-like through a local order parameter
- once each ion is labelled, the solid-liquid interface is found
- the velocities are rescaled in order to ensure that roughly half the ions are solid and half are liquid; this rescaling is slowly done (every 100 timesteps) in order to keep the temperature approximately constant.

The time step is chosen as a fraction of the ionic plasma frequency:

$$\bar{\omega}_P = \left[\frac{4\pi e^2 \langle Z \rangle^2 n_i}{\langle M \rangle}\right]^{1/2} \tag{8.1}$$

and the simulations runned for the long time of $2.8 \cdot 10^6/\bar{\omega}_P$.

The authors argue that the species have enough time to diffuse and equilibrate at their liquidus and solidus values in the liquid and solid fraction, respectively. Once the simulation is finished, they sort the ions as in a deep solid phase, deep liquid phase, or in the interface. They finally average the oxygen fraction in these three subsystems to find the liquidus and solidus oxygen fraction at the simulation temperature. As can be seen on Figure (8.2), their results seem to confirm the Medin diagram as being the most correct one to date.

In our work, we tried to question - and maybe confirm - these results since two aspects seemed debatable:

1. since diffusion inside a solid phase is a very long process, it is not clear whether the simulation time was sufficient or not for reaching the equilibrium state;

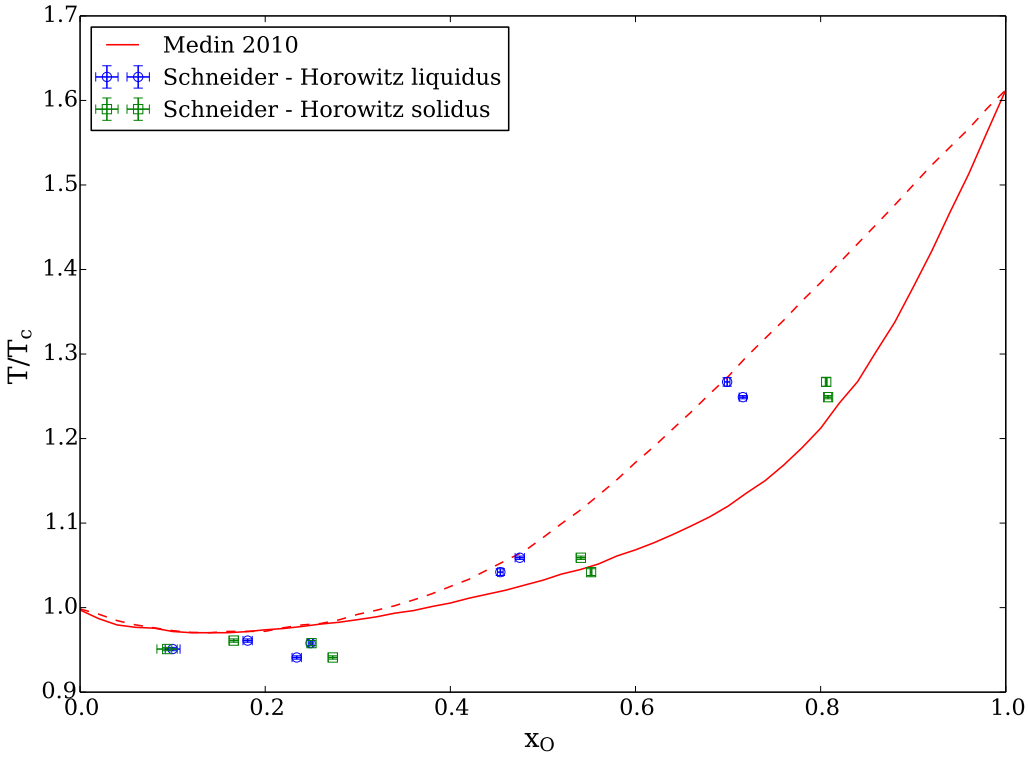

Figure 8.2: Schneider and Horowitz results compared to Medin 2010

2. their simulations were run for very high densities, corresponding to a density parameter $r_s \sim 10^{-4}$; these conditions are not supposed to be relevant for WD interiors, but for neutron stars. If the OCP properties only depend on Γ and not on the density parameter, it is not certain that the adopted Yukawa model is not subject to modifications when r_s is divided by 100.

We are now going to explain our methods and results for recomputing these diagrams from MD simulations.

II Our plasma mixture simulations

II.1 Pair potential between ions: the Yukawa plasma

In the OCP model, the electronic background is assumed to be rigid, and the ions interact through a Coulomb pair potential. A less crude model is the Thomas-Fermi approach, in which the induced electrons density is accounted for using a first order development around the chemical potential:

$$n_{ind}(\vec{r}) = n(\mu_0 + eV(\vec{r})) - n(\mu_0) \approx \left(\frac{\partial n}{\partial \mu}\right)_{\mu_0} eV(\vec{r}) \tag{8.2}$$

with μ_0 the Fermi level E_F and $V(\vec{r})$ the electric potential.
With this approximation, the effective potential created by a point-like ion of charge Z is described by the Poisson equation:

$$\Delta V(r) = -4\pi(Ze\delta(r) - en_{ind}(r)) \tag{8.3}$$

which can be solved in Fourier space, leading to a Yukawa potential:

$$\Delta V(r) = \frac{Ze}{r} e^{-r/\lambda} \tag{8.4}$$

with

$$\lambda^{-2} = 4\pi e^2 \left(\frac{\partial n}{\partial \mu}\right)_{E_F} \tag{8.5}$$

The density is linked to the Fermi wavevector by:

$$n = \frac{1}{3\pi^2} k_F^3 \tag{8.6}$$

but the link between the Fermi level E_F and the Fermi wavevector k_F depends on the relativistic nature of the electrons.

Before discussing the actual mathematical form of k_F, we can notice that taking this pair potential is not only more precise than the crude OCP, but also more numerically convenient. It introduces a natural typical length that can be used to determine an interaction cutoff and a consistent box size, which is not the case with the Coulomb pair potential. However, if the screening length remains large enough, it may still be problematic and require us to use the Ewald sums technique (see Appendix A) to take this into account.

Non relativistic case

The Fermi level and wavevector are related by:

$$E_F = \frac{\hbar^2 k_F^2}{2m} \tag{8.7}$$

so that

$$\left(\frac{\partial n}{\partial \mu}\right)_{E_F} = \frac{1}{3\pi^2} k_F^2 \frac{m}{\hbar^2 k_F} \tag{8.8}$$

which, with the interionic distance a_i and the interelectronic distance a_e, leads to:

$$\frac{\lambda}{a_i} = \left(\frac{4}{9\pi}\right)^{1/6} \frac{\hbar}{2e\langle Z\rangle^{1/3}} \sqrt{\frac{\pi}{m}} a_e^{-1/2} \underset{n\to\infty}{\longrightarrow} \infty \tag{8.9}$$

such that when the density increases, the mixture behaves more and more like the OCP model.

Relativistic case

The Fermi level and wavevector are now related by:

$$E_F^2 = \hbar^2 c^2 k_F^2 + m^2 c^4 \tag{8.10}$$

so that

$$\left(\frac{\partial n}{\partial \mu}\right)_{E_F} = \frac{1}{3\pi^2} k_F^2 \frac{1}{\hbar c} \left(1 + \frac{1}{x^2}\right)^{1/2} \tag{8.11}$$

with $x = \hbar k_F / mc$ the relativistic parameter. This leads finally to:

$$\frac{\lambda}{a_i} = \left(\frac{4}{9\pi}\right)^{1/3} \frac{1}{2\langle Z\rangle^{1/3}} \sqrt{\frac{\pi}{\alpha}} \left(1 + \frac{1}{x^2}\right)^{-1/4} \underset{n\to\infty}{\longrightarrow} cst \underset{pure\ carbon}{\approx} 3 \tag{8.12}$$

as the relativistic parameter increases with density (ultra relativistic limit). We can see here that the mixture will not exactly behave like the OCP as the density increases. On the other hand, this does not imply that the corresponding phase diagram is highly different, and that point may need further study.

The Yukawa OCP has been studied and its phase diagram computed by various means [**? ? ? ?**]. However, the question of the mixture has been little studied so far.

II.2 Numerical strategy

We adopted a two-phase approach (TPA) for our simulations: a solid and a liquid phase are thermalized separately at the desired temperature, then they are put in contact. After this, a MD simulation is computed until the most stable phase remains. In order to avoid metastable solid phases leading to false a conclusion, it is recommanded to test this approach with various usual solid phases. We can test every temperature, and construct the diagram with a collection of points. Our code has been tested against [**?**] for pressure and energy estimators, as well as phase transition boundary for one component.

However, the TPA is only simple for a one-component system. In the case of a binary mixture, the existence of a stability region where both liquid and solid phases are stable simultaneously raises the question of defining this state from our numerical simulations. The practical answer is that we observed a typical equilibrium time of around $1300/\bar{\omega}_P$ and up to $2000/\bar{\omega}_P$ when only one phase was stable, and that both were still stable after $2500/\bar{\omega}_P$ in other simulations. We adopted the coexistence of two phases after a simulation time of $2500/\bar{\omega}_P$ as a criterion for the thermodynamical coexistence of the two phases in the mixture; with this criterion, the obtained binary diagram is consistent with the previous literature.

However, the possibility that the system is trapped in a metastable phase coexistence cannot be excluded. Consequently, we may find the liquidus at a higher temperature than the real physical one, since we might wrongly identify a metastable mixture as a thermodynamically stable coexistence. The same reasoning leads to a solidus which may be found at a lower temperature than the real one, based on our stability criterion. The construction is illustrated in Figure (8.5): it is quite understandable that, if we identify as coexistence a metastable system, the resulting diagram is wider than the real one.

The final phase composition of the system was assessed with two tools:

- a visual representation of the trajectories
- the mean-square displacements in the last tenth of the simulation time for two well-identified regions of the system: one quarter of the box at the center of the initially liquid half of the box, and one quarter of the box at the center of the initially solid half of the box.

Since we use really short simulation lengths, the oxygen fractions computed in either the liquid or the solid phase, as done by Horowitz, cannot be used as a correct criterion. In our simulations, we observed an irregular pattern for this quantity.

We constructed two phase diagrams: one at $r_s = 1.4744 \cdot 10^{-4}$ and one at $r_s = 0.01$, corresponding respectively to the one constructed by Horowitz and a typical WD value. We evaluated the liquidus and solidus boundaries at eleven compositions evenly spaced between 0 and 1. We used a 2048-ions system, leading to a box size of $\sim 11 a_i$; according

to the limit result in (8.12), this is not a large enough system to only apply the minimum image convention, and we have used the Ewald sum technique (see Appendix A). We also tested our technique on a 4000-ions system; in this case, we needed a longer typical equilibration time of $3000/\bar{\omega}_P$ and we adopted the coexistence after a $5000/\bar{\omega}_P$ simulation as our criterion.

We give here a brief explanation on the uncertainties estimate. We narrowed the end of the spindle between two Γ values. Let us discuss a given x_O to explain: in the case of $x_O = 0.6$ at $r_s = 0.01$, the liquidus transition was found between $\Gamma = 213$ and $\Gamma = 215$, so that we adopt $\Gamma = 214 \pm 1$; the solidus transition of the same run is found at $\Gamma = 226 \pm 1$. This uncertainty on Γ leads to an uncertainty between 0.005 and $0.01 T_c$.

III Results and discussion

We present in Figure (8.4) and Figure (8.3) four simulations with a composition of $x_O = 0.6$ and $r_s = 0.01$ at various Γ values near the transition. It can be seen on these plots that the regions where the phases are stable are identifiable with our criterion. From these plots, the conclusion is that the liquidus is between $\Gamma = 213$ and 215, while the solidus is located between 225 and 227. From these simulations, we constructed the phase diagrams that can be seen on Figure (8.6). The pure carbon and pure oxygen freezing temperatures are obtained from similar simulations, and lead to a transition between $\Gamma = 177$ and $\Gamma = 179$ at $r_s = 1.4744 \cdot 10^{-4}$ - compatible with a transition at $\Gamma = 178.2$ as predicted in the equation (4) of [**?**] for the Yukawa OCP - and a transition between $\Gamma = 179$ and $\Gamma = 180$ at $r_s = 0.01$ - also compatible with a transition predicted by the equation (4) of [**?**] at $\Gamma = 179.7$.

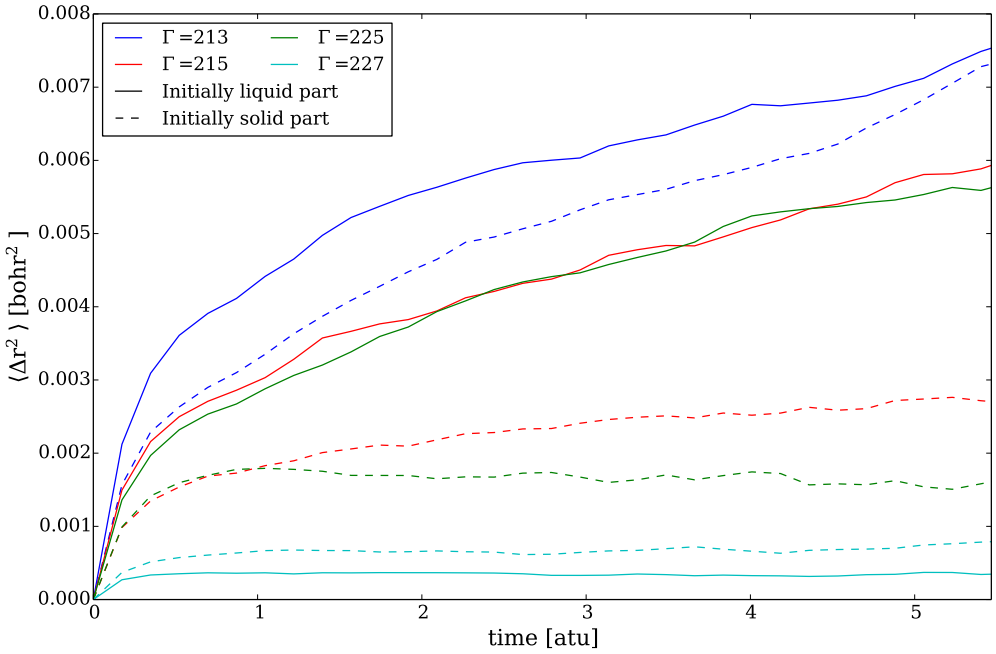

Figure 8.3: Mean-square displacements for $x_O = 0.6$ at various Γ values, computed with the last tenth of the simulations.

The corresponding simulation points for the $r_s = 1.4744 \cdot 10^{-4}$ and disordered solid phase (see below) case are shown on Figure (8.5).

Let us discuss the various data represented on Figure (8.6). The starting solid phases were BCC phases, according to the well-known result of BCC phase for the OCP. The mixture was created either by a regular or randomized substitution. On this figure, we present the results obtained in these two configurations for the $r_s = 1.4744 \cdot 10^{-4}$ case only. It can be seen that the two initial solid phases lead to similar results, except for the case $x = 0.5$ in which a perfectly ordered substitution leads to a drastic increase of the solid stability. This effect was not further investigated, but we suggest this stability stems from the high symmetry of such a system. It is however important to notice that this case is a limit model: real-life alloys generally show disordered clusters of pure carbon and oxygen. In consequence, we do not think of this computation as relevant for realistic applications. Consequently, this suggests the need to try more realistic solid phases as initial condition; we lacked time to conduct this study.

The results of our simulations can be seen in Figure (8.6). The first important result is that the diagram only marginally depends on the value of r_s, which validates the use of the previous work at $r_s = 1.4744 \cdot 10^{-4}$ for an application to WD cooling. Another immediate result of our diagram is the absence of azeotropic point.

In the $x > 0.5$ region, our solidus and liquidus qualitatively confirm the results from the recent literature. A more precise reading shows that these transition lines are thinner than the analytic work from Medin *et.al* , but still compatible with the work from Horowitz and Schneider.

The $x < 0.5$ shows a few differences from previous work. The solidus in this region is found at lower temperatures that in the works by both Medin and Horowitz. The liquidus is the same as in these works, leading to a globally thicker spindle in this region. The main difference is the absence of a clear azeotrope, which was found in their work roughly between $x = 0.1$ and $x = 0.3$. In our calculations, the wider spindle seems to prevent the apparition of such an azeotrope.

Let us insist once again on the limitation of our diagram: since we used the coexistence of the phases after an arbitrary time as criterion for stability, the system could be in a metastable state in the diphasic region, which we would consider at equilibrium. However, there is no physical reason for the metastability to be more important in the $x < 0.5$ region than in the $x > 0.5$ part of diagram. In consequence, if our results are coherent with the oxygen-rich part of the diagram, the differences in the carbon-rich part may not stem from our numerical strategy.

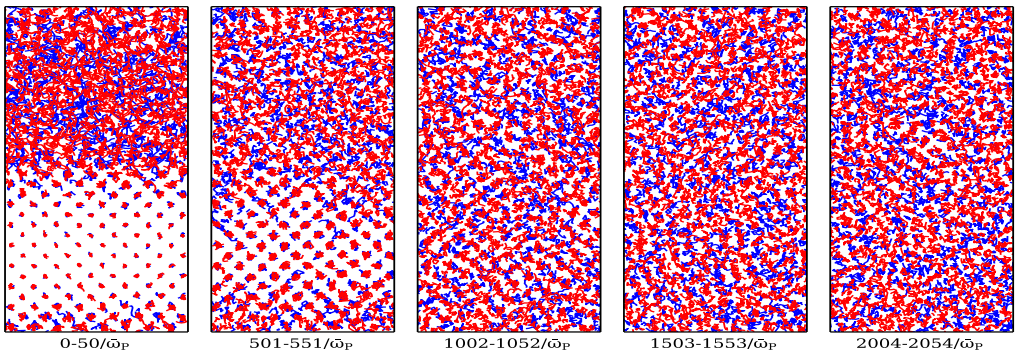

(a) $\Gamma = 213, t/tc = 1.135$

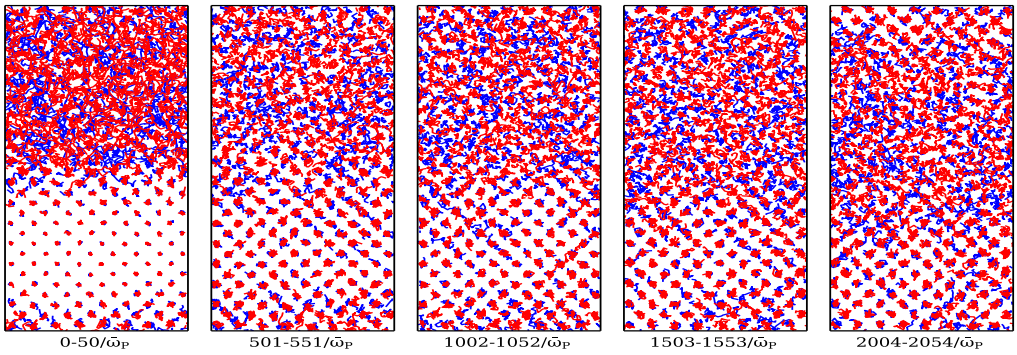

(b) $\Gamma = 215, t/tc = 1.124$

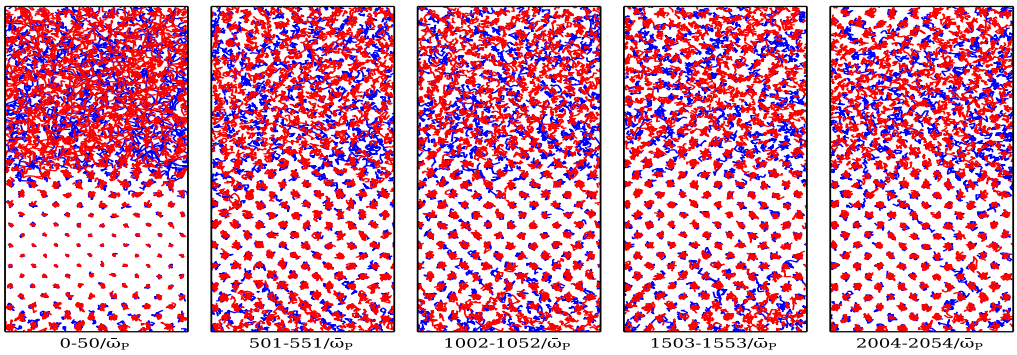

(c) $\Gamma = 225, t/tc = 1.074$

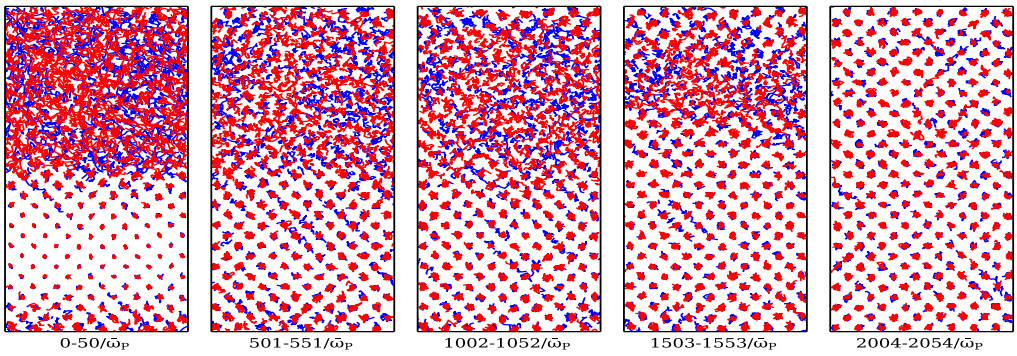

(d) $\Gamma = 227, t/tc = 1.065$

Figure 8.4: Evolution of the system in the $x - z$ plane at different Γ values for $r_s = 0.01$ and $x_O = 0.6$. The red trajectories are the oxygen atoms and the blue trajectories are the carbon atoms.

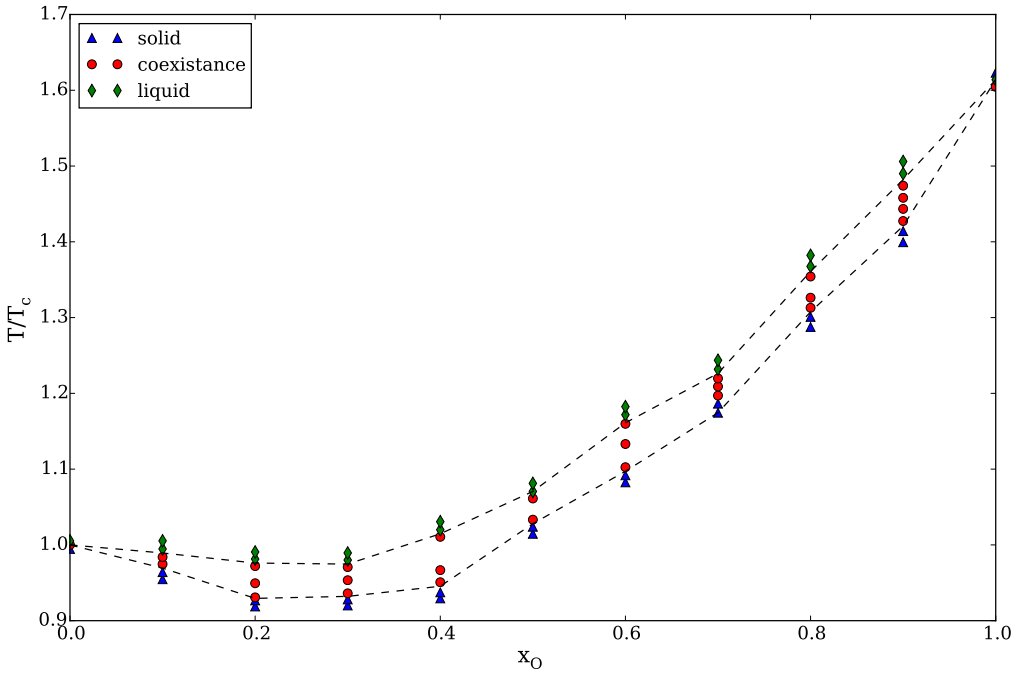

Figure 8.5: Simulation points obtained in the $r_s = 1.4744 \cdot 10^{-4}$ case with random substitutions. The construction of the binary diagram is shown here.

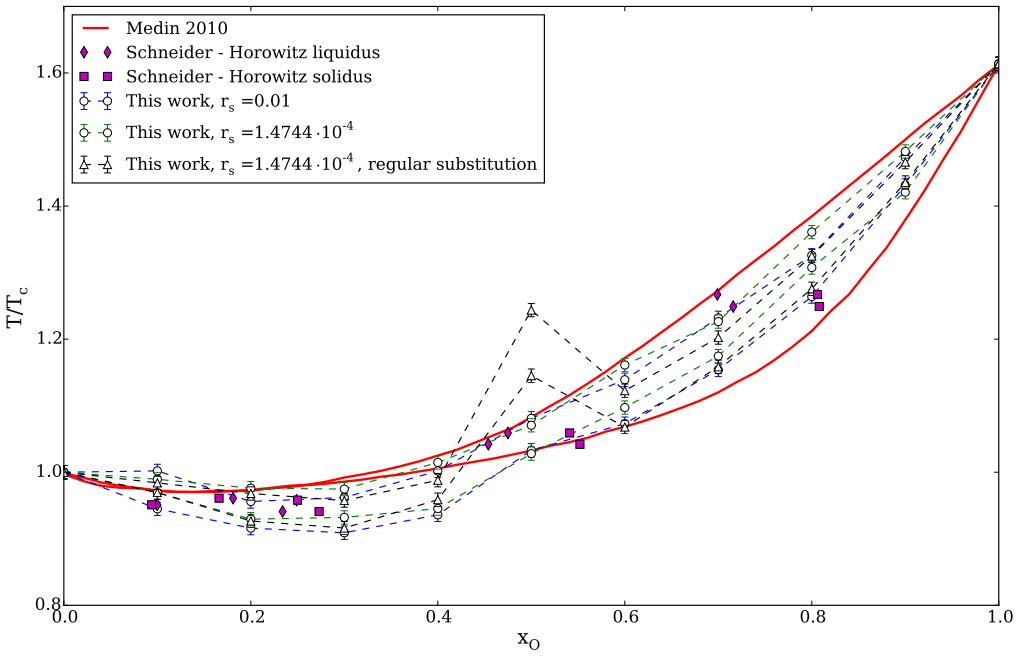

Figure 8.6: New phase diagrams from this work, compared with Medin [**?**] and Horowitz-Schneider calculations [**? ?**].

IV Conclusion

We proposed a new numerical method for estimating the phase diagram of the Yukawa or Coulomb mixtures, based on the coexistence of two phases. We confirmed previous results, such as the approximate temperature of the liquidus which is much lower in our work and the recent literature than in the previous Segretain-Chabrier diagram. As a consequence, a correct estimate of the age of a $0.6M_{\odot}$ WD showing a luminosity $\log L/L_{\odot} = -4.5$ - and, therefore of the age of the galaxy - seems to be around 10.7 Gyr - against the 11.7 Gyr obtained from the Segretain-Chabrier diagram [**?**].

If this diagram is still confirmed in future research work, the discrepancy between the estimate of the age of the galaxy by the WD and the globular cluster method must be considered a reopened question.

Part IV

Conclusions and perspectives

Conclusion and perspectives

In summary, we studied the thermodynamic properties of strongly coupled plasmas in various contexts, ranging from planetary interiors - where pressures reach a few Mbars - to white dwarfs interiors - where the pressure reaches 10^{11}Mbars.

In the planetary regime, the pressure leads to partial pressure ionization, and complex interactions between electrons and nuclei occur. Quantum effects have a high impact on the electronic behavior, and many complex physical phenomena take place in this regime. In the case of water and ammonia in these interiors, an exotic phase, called superionic ice, has been highlighted in numerical simulations, and various work have provided numerical calculations of the equation of state. We extended the pressure-temperature range of the known equations of state and phase diagrams for water, ammonia and methane with calculations based on the Density Functional Theory.

In chapter 5, we treated the case of water. We reached very high densities for Super-Jupiter conditions, until we matched the fully-ionized Thomas-Fermi limit. This allowed us to design an analytical fit, providing a thermodynamically consistent representation of the equation of state through a wide range of conditions, from the experimental data at usual pressures to this analytic limit. This equation of state is now ready-to-use in any calculation involving pure water compressibility, especially planetary interiors. We also found that the superionic phase, predicted at a few Mbars regime, is sustained at higher densities.

Moreover, we confirmed the existence of a superionic phase of ammonia in chapter 6, and questioned the superionic-fluid phase transition limit available in the previous literature. We found a superionic-fluid transition at higher temperature than previous work, which asks for more investigation in future research. Similarly to the case of water, we extended the knowledge of the equation of state to higher densities, but we stayed within the limit of Jupiter-like planets.

As also shown in chapter 6, the case of methane is slightly more complicated: the phase diagram shows a qualitatively different behavior than water and ammonia. A new phase has been established in a previous work, and we did not have time to completely test it in our own simulations; however, we have checked some features of this new phase, which tends to confirm this previous work. In the same spirit as for the other ices, we provide an extended thermodynamic table for methane as well.

However, this work on planetary ices is still only the first step of the planetary models, since methane shows a very different behavior in the planetary regime and the mixture of all these ices is still to be studied extensively. A few experimental studies have been conducted on "synthetic Uranus", a mixture of water, ammonia and isopropanol; the associated numerical investigation is still to come in the next years.

In the white dwarfs regime, the involved phenomena are quite different. The electronic contribution reaches the perfect Fermi gas behavior, and is analytically well-described - either through a simple functional or, as we did, through an effective ion-ion potential. While the Fermi gas pressure is the main contribution to the internal pressure of these stars, the ionic dynamic is the main thermal energy reservoir. In this context, the possibility of a solid-liquid transition phase may have dramatic consequences on the cooling dynamic of the star. In particular, typical white dwarves are mainly a mixture of carbon and oxygen nuclei, and the shape of the binary phase diagram can lead to a sedimentation of one species. Given the gigantic gravity fields reigning in these stars, this can lead to a substantial modification of the gravitational energy reservoir, and in consequence the cooling time may be affected, and the luminosity at a given age may be changed as well. The question of the luminosity function of white dwarves, as recalled in chapter 7, is related to datation of the galactic disk, since white dwarves are the most common stellar remnants: if our models can correctly estimate the age of a white dwarf from its luminosity, they allow us to estimate the age of the galaxy.

This question of the white dwarfs binary phase diagram have been reopened in recent literature, and we proposed in chapter 8 a new numerical strategy to explore this question, based on the Two-phase approach, yet unused for this problem. We found a new diagram, which is not totally compatible with the previous literature; in particular, we found a simple spindle diagram, while recent works showed an azeotropic point. However, we confirmed what was an assumption in previous work, that the binary diagram did not depend strongly on the density parameter, even taking into account the electronic polarizability.

The question of the age of the galactic disk is now reopened, since the Segretain-Chabrier spindle diagram, which previously settled the discrepancy between white dwarves datation and other methods, seems to be inaccurate. Further investigation is needed to understand in a finer manner the complete cooling dynamics of white dwarves.

Part V

Appendix

Appendix A

Ewald sums

Contents

I Describing a periodic system 118
II Separating the potential 119
III Efficiently computing the long-ranged contribution 121
IV Ewald sums and the pressure estimator 123

I Describing a periodic system

Let us consider a system of N ions interacting via either a Coulomb or Yukawa potential $\phi(r)$ in a box of volume V, and all the periodic replications of the box. The potential exerted on one particle i of charge Z_i by another particle j of charge Z_j separated by a distance $\mathbf{r}_{ij}$, plus all j's periodic replications could be naively written:

$$Z_i Z_j \phi^P(\mathbf{r}_{ij}) = Z_i Z_j \sum_{\mathbf{R}} \phi(|\mathbf{r}_{ij} + \mathbf{R}|) \tag{A.1}$$

with $\mathbf{R}$ defined as $(n_x L_x, n_y L_y, n_z L_z), (n_x, n_y, n_z) \in \mathbb{Z}^3$ and $\phi(r) = 1/r$ for Coulomb, $e^{-\alpha r}/r$ for Yukawa. Since this sum is not or slowly convergent, one has to add the neutralizing rigid electronic background to get a workable definition:

$$Z_i Z_j \phi^P(\mathbf{r}_{ij}) - Z_i \left(\sum_{j=1}^{N} Z_j \right) \phi^{back} = Z_i Z_j \sum_{\mathbf{R}} \phi(|\mathbf{r}_{ij} + \mathbf{R}|) - Z_i \frac{\sum_{j=1}^{N} Z_j}{V} \int \phi(|\boldsymbol{\rho}|) d\boldsymbol{\rho} \tag{A.2}$$

This sum is still only conditionally convergent in the Coulomb case. The total potential energy is then the sum of the potentials between all ion pairs and their replicas, between all the ions and the neutralizing background, and between the system and the replicas of itself:

$$U = \frac{1}{2} \sum_{i \neq j}^{N} Z_i Z_j \phi^P(\mathbf{r}_{ij}) + \frac{1}{2} \sum_{i}^{N} Z_i^2 \phi^{P*}(\mathbf{0}) - \frac{1}{2} \left(\sum_{i=1}^{N} Z_i \right)^2 \phi^{back} \tag{A.3}$$

where

$$\phi^{P*}(\mathbf{0}) = \sum_{\mathbf{R} \neq \mathbf{0}} \phi(|\mathbf{R}|) = \lim_{r \to 0} \left\{ \phi^P(\mathbf{r}) - \phi(\mathbf{r}) \right\} \tag{A.4}$$

is the Madelung constant. In the case of a polarizable background (Yukawa potential), one has to add the Debye sheath contribution, which has been computed in [**?**] and used in [**?**]:

$$U_{sheath} = -N \langle Z \rangle^2 \frac{1}{2\alpha} \tag{A.5}$$

with a_i the ionic Wigner-Seitz radius.

Since the potential is long-ranged one must take many replicas into account. If raw computational power is not a solution for handling such long-range forces, one must find another workaround.

The Ewald sum is a computation technique first introduced by Ewald in 1921 [**?**] in order to separate the evaluation of the Madelung energy of infinite crystals. The basic idea is to split the potential in two parts:

- a screened short-ranged potential, which might be computed directly as a the sum of the pair interactions in the minimum image convention ; mathematically, this is obtained by adding the potential created by a fictitious (generally Gaussian) charge distribution

- a long-range contribution, which is the potential created by minus the fictitious screening charge distribution, and which can be more easily estimated in Fourier space with relatively few wavevectors

II Separating the potential

Let us separate our pair potential into a short-ranged and a long-ranged part:

$$\phi(\mathbf{r}_{ij}) = \phi_{sr}(\mathbf{r}_{ij}) + \phi_{lr}(\mathbf{r}_{ij}) \tag{A.6}$$

The mathematical form of the separation will be provided but not discussed here; one can find the details, for example, in [**?** **?** **?** **?**] for Coulomb potential and in [**?**] for Yukawa potential - which also includes a discussion of the Coulomb limit. The first term will be designed to be rapidly convergent in order to only keep the $\mathbf{R} = \mathbf{0}$ contribution and be evaluated in direct space:

$$\phi^P_{sr}(\mathbf{r}_{ij}) = \phi_{sr}(r_{ij}) - \frac{Z_i Z_j}{V} \int \phi_{sr}(r_{ij}) d\mathbf{r}_{ij} \tag{A.7}$$

The second term will be a slowly varying contribution, and can then be evaluated quickly in the reciprocal space using inverse Fourier transform:

$$\phi^P_{lr}(\mathbf{r}_{ij}) = \int \hat{\phi}_{lr}(\mathbf{k}) e^{i\mathbf{k}\cdot\mathbf{r}_{ij}} d\mathbf{k} \tag{A.8}$$

The form of the separation of the ion-ion potential must be chosen carefully ; the general idea is to add and retract a Gaussian charge distribution with a characteristic length $1/\beta$:

$$\rho_G(\mathbf{r}) = \left(\frac{\beta^2}{\pi}\right)^{3/2} \exp(-\beta^2 \mathbf{r}^2) \tag{A.9}$$

and then separate the Poisson equation for the potential created by one charge (with $\alpha = 0$ in the Coulomb case):

$$(\Delta - \alpha^2)\phi(\mathbf{r}) = -4\pi\delta(\mathbf{r}) \tag{A.10}$$

into two Poisson equations:

$$(\Delta - \alpha^2)\phi_{sr}(\mathbf{r}) = -4\pi(\delta(\mathbf{r}) - \lambda\rho_G(\mathbf{r})) \tag{A.11}$$

$$(\Delta - \alpha^2)\phi_{lr}(\mathbf{r}) = -4\pi\lambda\rho_G(\mathbf{r}) \tag{A.12}$$

λ being a constant which is chosen to be $\exp(-\alpha^2/4\beta^2)$ in order to cancel the long-range contribution in the short-ranged part of the potential. The short-ranged potential then decreases as $e^{-(\beta r)^2}/r^2$.

The detailed calculation can be found in [**?**] ; here we just give the solution. The short-ranged ion-ion contribution is:

$$\phi^P_{sr}(\mathbf{r}) = \sum_{\mathbf{R}} \phi_{sr}(|\mathbf{r} + \mathbf{R}|) \tag{A.13}$$

$$= \sum_{\mathbf{R}} \frac{1}{2|\mathbf{r} + \mathbf{R}|} \left[\operatorname{erfc}\left(\beta|\mathbf{r} + \mathbf{R}| + \frac{\alpha}{2\beta}\right) e^{\alpha|\mathbf{r}+\mathbf{R}|} + \operatorname{erfc}\left(\beta|\mathbf{r} + \mathbf{R}| - \frac{\alpha}{2\beta}\right) e^{-\alpha|\mathbf{r}+\mathbf{R}|} \right] \tag{A.14}$$

where erfc is the complementary error function

$$\operatorname{erfc}(x) = \frac{2}{\sqrt{\pi}} \int_x^\infty e^{-t^2} dt \tag{A.15}$$

In the Coulomb case, this trivially reduces to

$$\phi^P_{sr,Coul}(\mathbf{r}) = \sum_{\mathbf{R}} \frac{\operatorname{erfc}(\beta|\mathbf{r}+\mathbf{R}|)}{|\mathbf{r}+\mathbf{R}|} \tag{A.16}$$

As previously stated, these expressions decrease quickly enough to keep only the $\mathbf{R} = \mathbf{0}$ part for a suitable value of β. The long-ranged contribution is expressed in Fourier space with the reciprocal lattice vectors $\mathbf{K} = (2\pi n_x/L_x, 2\pi n_y/L_y, 2\pi n_z/L_z), (n_x, n_y, n_z) \in \mathbb{Z}^3$:

$$\phi^P_{lr}(\mathbf{r}) = \frac{4\pi}{V} \sum_{\mathbf{K}\neq\mathbf{0}} \frac{1}{\mathbf{K}^2+\alpha^2} e^{-\frac{\mathbf{K}^2+\alpha^2}{4\beta^2}} e^{i\mathbf{K}\cdot\mathbf{r}} \tag{A.17}$$

And the background contribution:

$$-\phi^{back} = \frac{4\pi}{V\alpha^2}(1 - e^{\frac{-\alpha^2}{4\beta^2}}) \qquad \text{for Yukawa potential} \tag{A.18}$$

$$= -\frac{\pi}{\beta^2 V} \qquad \text{in the Coulomb limit} \tag{A.19}$$

The Madelung constant (A.4) is then:

$$\begin{aligned}\phi^{P*}(\mathbf{0}) = &\sum_{\mathbf{R}\neq\mathbf{0}} \frac{1}{2R}\left[\operatorname{erfc}\left(\beta R + \frac{\alpha}{2\beta}\right) e^{\alpha R} + \left(\beta R - \frac{\alpha}{2\beta}\right) e^{-\alpha R}\right] \\ &+ \frac{4\pi}{V} \sum_{\mathbf{K}\neq\mathbf{0}} \frac{1}{\mathbf{K}^2+\alpha^2} e^{-\frac{\mathbf{K}^2+\alpha^2}{4\beta^2}} - \frac{2\beta}{\sqrt{\pi}} e^{-\frac{\alpha^2}{4\beta^2}} + \alpha \operatorname{erfc}\left(\frac{\alpha}{2\beta}\right) + 4\pi \frac{e^{\frac{-\alpha^2}{4\beta}} - 1}{\alpha^2 V}\end{aligned} \tag{A.20}$$

the first term being negligible for a suitable value of β since this is the short-ranged contribution. Finally, one can rewrite the total energy of the system (A.3) as:

$$U = \sum_{\mathbf{R}} \frac{1}{2} \sum_{i\neq j} Z_i Z_j \phi_{sr}(|\mathbf{r}_{ij}+\mathbf{R}|) + \sum_{\mathbf{R}\neq\mathbf{0}} \frac{1}{2} \sum_{i=1}^{N} Z_i^2 \phi_{sr}(|\mathbf{R}|) \tag{A.21}$$

$$+ \frac{1}{2}\frac{4\pi}{V} \sum_{\mathbf{K}\neq\mathbf{0}} \frac{1}{\mathbf{K}^2+\alpha^2} e^{-\frac{\mathbf{K}^2+\alpha^2}{4\beta^2}} \sum_{i,j} Z_i Z_j e^{i\mathbf{K}\cdot\mathbf{r}_{ij}} \tag{A.22}$$

$$- \left(\sum_{i=1}^{N} Z_i\right)^2 \frac{2\pi}{\alpha^2 V}(1 - e^{-\frac{\alpha^2}{4\beta^2}}) \tag{A.23}$$

$$- \sum_{i=1}^{N} Z_i^2 \left\{\frac{\beta}{\sqrt{\pi}} e^{-\frac{\alpha^2}{4\beta^2}} - \frac{1}{2}\alpha \operatorname{erfc}\left(\frac{\alpha}{2\beta}\right)\right\} \tag{A.24}$$

$$- \frac{1}{N}\frac{1}{2\alpha}\left(\sum_{i=1}^{N} Z_i\right)^2 \tag{A.25}$$

In the case of Coulomb potential, the last term is null and the two previous ones reduce to:

$$-\left(\sum_{i=1}^{N} Z_i\right)^2 \frac{\pi}{2\beta^2 V} - \sum_{i=1}^{N} Z_i^2 \frac{\beta}{\sqrt{\pi}}$$

In order to make clear the extensivity in this evaluation of the energy, one can rewrite

it as:

$$\begin{aligned}\frac{U}{N} =& \sum_{\mathbf{R}} \frac{1}{2N} \sum_{i \neq j} Z_i Z_j \phi_{sr}(|\mathbf{r}_{ij} + \mathbf{R}|) + \frac{1}{2}\langle Z^2 \rangle \sum_{\mathbf{R} \neq \mathbf{0}} \phi_{sr}(|\mathbf{R}|) \\ &+ \frac{1}{2} 4\pi \frac{N}{V} \sum_{\mathbf{K} \neq \mathbf{0}} \frac{1}{\mathbf{K}^2 + \alpha^2} e^{-\frac{\mathbf{K}^2 + \alpha^2}{4\beta^2}} \frac{1}{N^2} \sum_{i,j} Z_i Z_j e^{i\mathbf{K} \cdot \mathbf{r}_{ij}} \\ &- \langle Z \rangle^2 \frac{2\pi}{\alpha^2} \frac{N}{V} (1 - e^{-\frac{\alpha^2}{4\beta^2}}) \\ &- \langle Z^2 \rangle \left\{ \frac{\beta}{\sqrt{\pi}} e^{-\frac{\alpha^2}{4\beta^2}} - \frac{1}{2} \alpha \operatorname{erfc}\left(\frac{\alpha}{2\beta}\right) \right\} \\ &- \frac{1}{2\alpha} \langle Z \rangle^2\end{aligned}$$

Let us now discuss the value of β. Since we want to keep only the $\mathbf{R} = \mathbf{0}$ contribution in the short-ranged part, the function must decrease fast enough to have $\phi_{sr}(L/2)$ negligible, L being the size of the box. In the original papers (e.g [**?**]) the choice was $\beta = \sqrt{\pi}/L$, so that $\phi_{sr}(L/2) = \operatorname{erfc}(\sqrt{\pi}/2)/(L/2) \approx 0.42/L$. Salin and Caillol [**?**] proposed a more correct approach to estimate this parameter, which leads to $\beta \simeq 6/L$ (with a dependence in the number of wavevectors kept in the $\mathbf{K}$ basis).

The force exerted on a particle i is then given by the gradient of the potential energy:

$$\begin{aligned}\mathbf{F}_i =& -\nabla_i U \\ & \sum_{\mathbf{R}} Z_i \sum_{k \neq i} Z_j \nabla_i \phi_{sr}(|\mathbf{r}_{ij} + \mathbf{R}|) \\ &+ \frac{4\pi}{V} \sum_{\mathbf{K} \neq \mathbf{0}} \frac{1}{\mathbf{K}^2 + \alpha^2} e^{-\frac{\mathbf{K}^2 + \alpha^2}{4\beta^2}} Z_i i\mathbf{K} \sum_{j=1}^{N} Z_j e^{i\mathbf{K} \cdot \mathbf{r}_{ij}}\end{aligned} \tag{A.26}$$

III Efficiently computing the long-ranged contribution

Let us rewrite the main Fourier term in (A.21) in a more readable way:

$$U_{lr} = \frac{1}{2} \frac{4\pi}{V} \sum_{\mathbf{K} \neq \mathbf{0}} f(|\mathbf{K}^2|) \sum_{i,j=1}^{N} Z_i Z_j e^{i\mathbf{K} \cdot (\mathbf{r}_i - \mathbf{r}_j)} \tag{A.27}$$

Let us then note that

$$|\sum_i Z_i e^{i\mathbf{K} \cdot \mathbf{r}_i}|^2 = \sum_{i,j=1}^{N} Z_i Z_j e^{i\mathbf{K} \cdot (\mathbf{r}_i - \mathbf{r}_j)} \tag{A.28}$$

and we can reduce the N^2-terms sum in 3 N-terms sums

$$U_{lr} = \frac{1}{2} \frac{4\pi}{V} \sum_{\mathbf{K} \neq \mathbf{0}} f(|\mathbf{K}^2|) \left\{ \left(\sum_i Z_i \cos(\mathbf{K} \cdot \mathbf{r}_i) \right)^2 + \left(\sum_i Z_i \sin(\mathbf{K} \cdot \mathbf{r}_i) \right)^2 \right\} \tag{A.29}$$

This is already an improvement, but we can also take advantage of the symmetry of the $\mathbf{K}$ collection. First, for the $\mathbf{K}$ vectors of the form $(k_x, 0, 0)$, it is immediate that the sums over the positive k_x and the negative k_x are equal ; one must then only compute

the positive values and then double the contribution. The same is of course true for the y and z axis. For the $\mathbf{K}$ vectors of the form $(k_x, k_y, 0)$, one can see that

$$\left(\sum_i Z_i \cos(k_x x_i + k_y y_i)\right)^2 = \left(\sum_i Z_i \cos(k_x x_i)\cos(k_y y_i)\right)^2 + \left(\sum_i Z_i \sin(k_x x_i)\sin(k_y y_i)\right)^2 - 2\sum_{i,j} Z_i Z_j \cos(k_x x_i)\cos(k_y y_i)\sin(k_x x_j)\sin(k_y y_j)$$

to check that, for given positive components k_x and k_y

$$\sum_{\mathcal{SP}} \left(\sum_i Z_i \cos(\pm k_x x_i \pm k_y y_i)\right)^2 = 4\left(\sum_i Z_i \cos(k_x x_i)\cos(k_y y_i)\right)^2 + 4\left(\sum_i Z_i \sin(k_x x_i)\sin(k_y y_i)\right)^2$$

where $\sum_{\mathcal{SP}}$ denotes the sum over the $\pm$ signs possible permutations. Similarly, for the sines:

$$\sum_{\mathcal{SP}} \left(\sum_i Z_i \sin(\pm k_x x_i \pm k_y y_i)\right)^2 = 4\left(\sum_i Z_i \cos(k_x x_i)\sin(k_y y_i)\right)^2 + 4\left(\sum_i Z_i \sin(k_x x_i)\cos(k_y y_i)\right)^2$$

and in the case of no zero component, one can show that

$$\sum_{\mathcal{SP}} \left[\left(\sum_i Z_i \cos(\pm k_x x_i \pm k_y y_i \pm k_z z_i)\right)^2 + \left(\sum_i Z_i \sin(\pm k_x x_i \pm k_y y_i \pm k_z z_i)\right)^2\right] = 8\left(\sum_i Z_i \cos(k_x x_i)\cos(k_y y_i)\cos(k_z z_i)\right)^2 + 8\left(\sum_i Z_i \cos(k_x x_i)\cos(k_y y_i)\sin(k_z z_i)\right)^2 + 8\left(\sum_i Z_i \cos(k_x x_i)\sin(k_y y_i)\cos(k_z z_i)\right)^2 + \ldots$$

with all the possible combinations of products of sines and cosines.

Finally, one has to compute once the $\cos(k_x x_i), \cos(k_y y_i), \cos(k_z z_i)$ (it is also possible to avoid the costly evaluation of many sines and cosines by using $\cos(2\pi(n+1)x_i/L_x) = \cos(2\pi n x_i/L_x)\cos(2\pi x_i/L_x) - \sin(2\pi n x_i/L_x)\sin(2\pi x_i/L_x)$ and so on). With these, one can perform in N complexity the computations for each $\mathbf{K}$ of strictly positive components (only one eighth of the phase space). Another interesting point is that the $\mathbf{K}$ vectors' contributions are independent, so that the computation can easily be parallelized either with a shared memory (OpenMP) or distributed memory (MPI) model.

For the forces computation, using the symmetries is more limited. The formulation we used is the following one:

$$\mathbf{F}_{i,lr} = \frac{8\pi}{V} Z_i \sum_{\mathbf{K}>\mathbf{0}} \frac{\mathbf{K}}{\mathbf{K}^2 + \alpha^2} e^{-\frac{\mathbf{K}^2+\alpha^2}{4\beta^2}} \sum_{j=1}^{N} Z_j \sin(\mathbf{K}\cdot\mathbf{r}_{ij}) \tag{A.30}$$

where the sum on $\mathbf{K} > 0$ means that we only estimate half-space contributions and double them thanks to the symmetry of each $\mathbf{K}$-term; but in this case, computing

only an eighth of the reciprocal lattice contributions is not sufficient , so we stick to computing half of the $\mathbf{K}$ vectors. The sum over the j-particles is expressed as follows:

$$\sum_{j=1\neq i}^{N} Z_j \sin(\mathbf{K}\cdot\mathbf{r}_{ij}) = \sin(\mathbf{K}\cdot\mathbf{r}_i)\sum_{j=1}^{N} Z_j\cos(\mathbf{K}\cdot\mathbf{r}_j) - \cos(\mathbf{K}\cdot\mathbf{r}_i)\sum_{j=1}^{N} Z_j\cos(\mathbf{K}\cdot\mathbf{r}_j) \quad \text{(A.31)}$$

IV Ewald sums and the pressure estimator

In chapter 2, we derived an estimator for the pressure of the system:

$$P(\{\mathbf{r}_i,\mathbf{p}_i\}) = \frac{NkT}{V} + \frac{\partial U}{\partial V}(\{\mathbf{r}_i,\mathbf{p}_i\}) \quad \text{(A.32)}$$

where U is the potential energy in the Hamiltonian of the system. If U only depends of the volume through the positions, the derivative in (A.32) reduces to a third of the virial of the system. In the case of the Ewald potential, one can see in (A.21) that this condition is not met; we must derive the derivative of U properly.

In order to limit our calculations, let us note that β and the reciprocal lattice vectors $\mathbf{K}$ depend on V as $V^{-1/3}$; in consequence, βr and $\mathbf{K}\cdot\mathbf{r}$ are independent from V, and composed derivatives introduce $\partial\beta/\partial V = -\beta/3V$ and $\partial K/\partial V = -K/3V$.

The short-ranged contribution, defined by the first term of (A.21), leads to:

$$\begin{aligned}\frac{\partial U_{sr}}{\partial V} &= -\frac{1}{3V}\frac{1}{2}\sum_{i\neq j} Z_iZ_j\frac{1}{2r_{ij}}\left\{\operatorname{erfc}(\beta r_{ij}+\frac{\alpha}{2\beta})(1-\alpha r_{ij})e^{\alpha r_{ij}} + \operatorname{erfc}(\beta r_{ij}-\frac{\alpha}{2\beta})(1+\alpha r_{ij})e^{-\alpha r_{ij}}\right\}\\ &= -\frac{1}{3V}U_{sr} + \frac{1}{3V}\frac{1}{2}\sum_{i\neq j} Z_iZ_j\alpha r_{ij}\left\{\operatorname{erfc}(\beta r_{ij}+\frac{\alpha}{2\beta})e^{\alpha r_{ij}} - \operatorname{erfc}(\beta r_{ij}-\frac{\alpha}{2\beta})e^{-\alpha r_{ij}}\right\}\end{aligned}$$

The Coulomb case can be found by setting $\alpha = 0$ or by direct calculation. Similarly, we can express the Fourier part:

$$\begin{aligned}\frac{\partial U_{lr}}{\partial V} &= -\frac{1}{V}U_{lr} + \frac{1}{3V}\frac{2\pi}{V}\sum_{\mathbf{K}\neq\mathbf{0}}\frac{1}{\mathbf{K}^2+\alpha^2}\left(\frac{2\mathbf{K}^2}{\mathbf{K}^2+\alpha^2} - \frac{\alpha^2}{2\beta^2}\right)e^{-\frac{\mathbf{K}^2+\alpha^2}{4\beta^2}}\sum_{i,j} Z_iZ_je^{i\mathbf{K}\cdot\mathbf{r}_{ij}}\\ &= -\frac{1}{3V}U_{lr} - \frac{1}{3V}\frac{\alpha^2}{2\beta^2}\frac{2\pi}{V}\sum_{\mathbf{K}\neq\mathbf{0}}\frac{\mathbf{K}^2+\alpha^2+4\beta^2}{(\mathbf{K}^2+\alpha^2)^2}e^{-\frac{\mathbf{K}^2+\alpha^2}{4\beta^2}}\sum_{i,j} Z_iZ_je^{i\mathbf{K}\cdot\mathbf{r}_{ij}}\end{aligned}$$

Once again, setting $\alpha = 0$ recovers the Coulomb case. The last terms lead to:

$$\frac{\partial U_{compl}}{\partial V} = \left(\sum_{i=1}^{N} Z_i\right)^2\frac{2\pi}{\alpha^2V^2}\{1-(1+\frac{\alpha^2}{6\beta^2})e^{-\frac{\alpha^2}{4\beta^2}}\} + \frac{1}{3V}\sum_{i=1}^{N} Z_i^2\frac{\beta}{\sqrt{\pi}}e^{-\frac{\alpha^2}{4\beta^2}} \quad \text{(A.33)}$$

in the Yukawa case and $-U_{compl}/3V$ in the Coulomb case. It is interesting to note that, in the case of a Coulomb potential, the derivative of the energy is $-U/3V$, which is a well-known property of the Coulomb interaction:

$$\frac{\partial}{\partial V}\left(\frac{1}{r}\right) = \frac{r}{3V}\frac{\partial}{\partial r}\left(\frac{1}{r}\right) = -\frac{1}{3V}\frac{1}{r} \quad \text{(A.34)}$$

The Yukawa potential does not exhibit a similar property. Finally, our estimator for the pressure is given by the sum of all these contributions.

Appendix B

Hugoniot experiments

Contents

I Shock experiments: an overview 125

II The Rankine-Hugoniot equations 126

III Theoretically estimating the Hugoniot 127

III.1 The principal Hugoniot 127

III.2 The perfect gas Hugoniot 127

III.3 The reshock states loci 128

In this appendix chapter, we are going to discuss the mathematical relations that arise in a shock-wave experiment, and the way it can be used to test an equation of state's validity.

I Shock experiments: an overview

Even if the thermodynamic conditions we are interested in are extreme, in the case of planetary ices they are not completely out of reach for experiments. While static compression experiments reach up to one Mbar [**?**], dynamic compression experiments allow to reach multi-Mbar pressures by propagating a shock wave through the sample. The shock can be created by a gas-gun detonation [**?**] [**?**], a laser impulsion [**?**] [**?**] or a flying projectile [**?**].

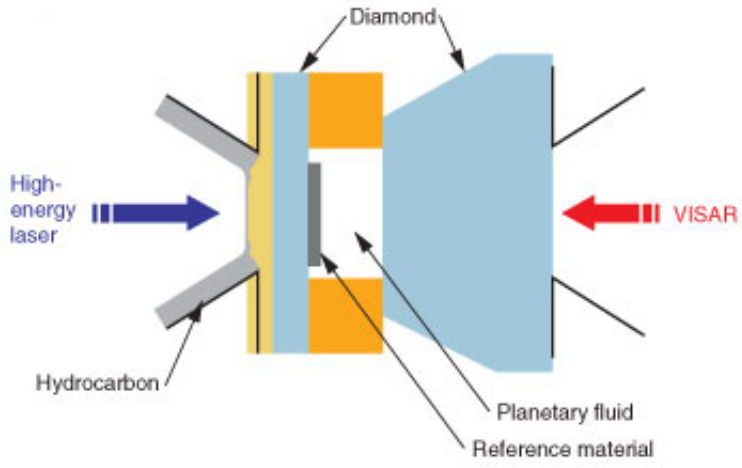

Figure B.1: Diamond Anvil Cell device for laser-driven shock

In Figure (B.1) we show the principle of a laser-driven shock: the diamond anvil cell (DAC) contains the sample and can be used to pre-compress it. A short laser impulse - about 1 ns long and with a power of a few TW - is then triggered on the target. In the case of an accelerated flying projectile, the projectile directly shocks the cell, as is shown in Figure (B.2). A shock wave propagates through the cell's window, then through the sample. A reference material, generally aluminum or quartz, is introduced inside the DAC between the target and the sample in order to measure properly the relative shock velocity. The velocities are measured with a velocity measurement interferometer (VISAR) [**?**].

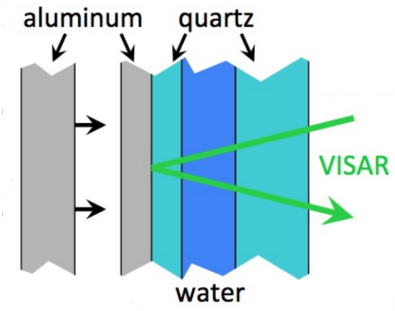

Figure B.2: Sandia Z [**?**] shock on water

In the case of the accelerated plates, when the shock wave reaches the rear window, it can be transmitted in the window and reflected, leading to a re-shocked state of the sample at higher P and ρ. This has mainly be used on water [**? ? ?**].

II The Rankine-Hugoniot equations

When a shock wave goes through a sample, a discontinuity appears in the thermodynamic properties before and after the shock front. We are going to show that their values are not independent.

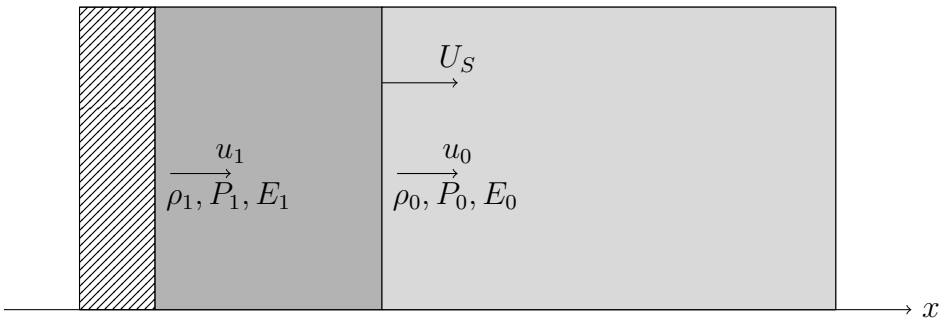

Figure B.3: Shock wave scheme

Let us consider a fluid sample of density ρ_0, pressure P_0 and internal energy E_0, flowing at speed u_0 in the laboratory frame (in practical experiments, the fluid is generally at rest). The shock wave moves through this sample at speed U_S and leaves the fluid behind at density ρ_1, pressure P_1 and internal energy E_1, flowing at speed u_1. We restrict ourselves to a linear one-dimensional shock (which is generally the case in shock experiments) and we will note S the section of the sample. The laboratory view is shown in Figure (B.3).

Let us change the frame to the shock wave self-frame like in Figure (B.4) and consider an element of fluid $ABCD$ going through the shock front. We note $u'_0 = u_0 - U_S$ the speed of the fluid flowing through the AD face and $u'_1 = u_1 - U_S$ the speed of the fluid flowing through the BC face. We assume the fluid element is large enough for the thermodynamic equilibrium to be reached.

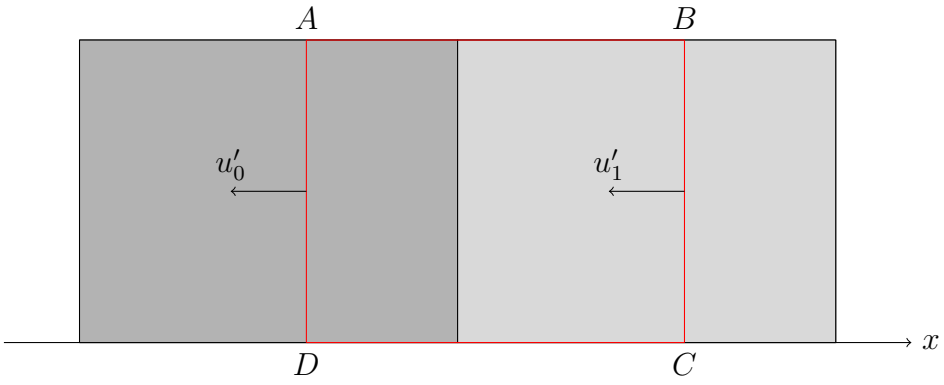

Figure B.4: Shock wave scheme in its own frame

The first conservation law we write is the conservation of mass flux through the $ABCD$ volume:

$$\rho_1 u'_1 S = \rho_0 u'_0 S \tag{B.1}$$

The conservation of the momentum is written as:

$$P_1 S + \rho_1 u_1'^2 S = P_0 S + \rho_0 u_0'^2 S \tag{B.2}$$

The conservation of energy flux is given by [**?**]:

$$S\rho_1 u_1'(\frac{1}{2}u_1'^{\,2} + E_1 + \frac{P_1}{\rho_1}) = S\rho_0 u_0'(\frac{1}{2}u_0'^{\,2} + E_0 + \frac{P_0}{\rho_0}) \tag{B.3}$$

Finally, this leads to the following system, known as the Rankine-Hugoniot equations:

$$\begin{cases} E_1 - E_0 = \frac{1}{2}(P_0 + P_1)(\frac{1}{\rho_0} - \frac{1}{\rho_1}) & \text{(B.4)} \\ P_1 - P_0 = \rho_0(u_1 - u_0)(U_S - u_0) & \text{(B.5)} \\ \rho_1 = \rho_0 \frac{U_S - u_0}{U_S - u_1} & \text{(B.6)} \end{cases}$$

Let us notice that (B.4) only involves the thermodynamic properties of the sample and not the dynamic of the shock, and does not involve the entropy; as a consequence, the Hugoniot curve can be deduced from the sole knowledge of a numerical equation of state.

III Theoretically estimating the Hugoniot

In this section, we will assume the knowledge of an equation of state and predict the corresponding Hugoniot curve, in order to compare it with the experimental curves. The equation of state will be assumed to be known in the form of the $E_{EOS}(\rho, T)$ and $P_{EOS}(\rho, T)$ functions.

III.1 The principal Hugoniot

The principal Hugoniot curve $P_H(\rho)$ is completely defined with the sole equation (B.4): for a given ρ, one has to solve for T the system

$$\begin{cases} E_{EOS}(\rho, T) - E_{EOS}(\rho_0, T_0) = \frac{1}{2}(P_0 + P_{EOS}(\rho, T))(\frac{1}{\rho_0} - \frac{1}{\rho}) & \text{(B.7)} \\ P_H(\rho) = P_{EOS}(\rho T) & \text{(B.8)} \end{cases}$$

In most cases, this has to be solved numerically. Let us illustrate a few possibilities on the perfect gas model.

III.2 The perfect gas Hugoniot

Let us start with a monoatomic perfect gas consisting of particles of mass m; the corresponding equation of state is:

$$\begin{cases} P_{EOS}(\rho, T) = \frac{\rho k_B T}{m} & \text{(B.9)} \\ E_{EOS}(\rho, T) = \frac{3}{2}\frac{k_B T}{m} & \text{(B.10)} \end{cases}$$

In this case, the resolution of (B.4) leads to:

$$P_H(\rho) = P_0 \frac{4\rho - \rho_0}{4\rho_0 - \rho} \tag{B.11}$$

One can immediately notice that the reachable densities have an upper bound $4\rho_0$. In he case of a diatomic gas, $E_{EOS}(\rho, T) = \frac{5}{2}\frac{k_B T}{m}$ and

$$P_H^{di}(\rho) = P_0 \frac{6\rho - \rho_0}{6\rho_0 - \rho} \tag{B.12}$$

where the upper bound have been translated to $6\rho_0$; this shows us that the more microscopic degrees of freedom the system has, the more compressed it can be. The corresponding Hugoniot curves are plotted in Figure (B.5).

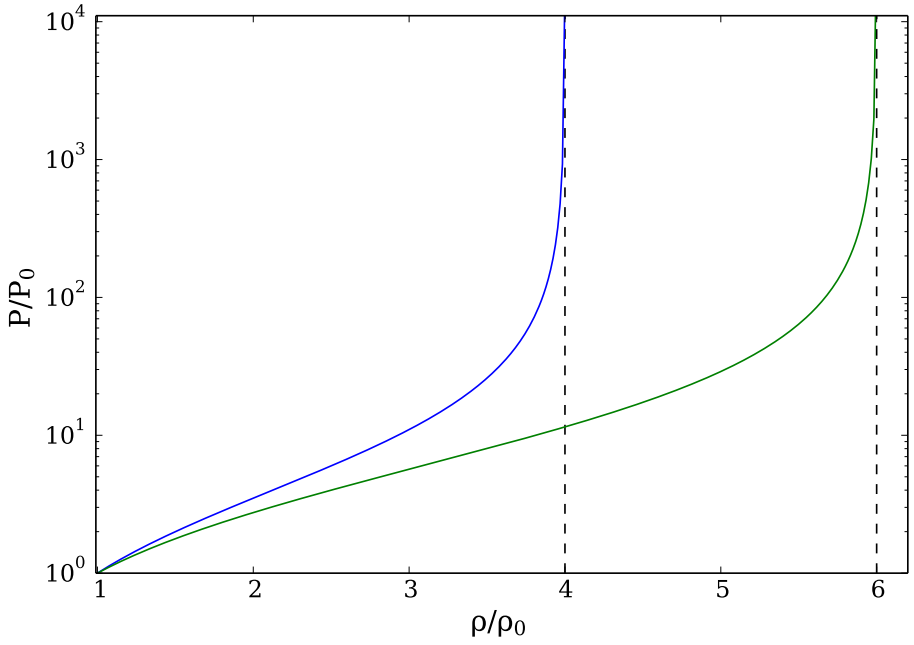

Figure B.5: Hugoniot curve for an ideal gas

In fact, any realistic material will dissociate into a perfect gas at very high pressure and temperature, so that the nuclear component of the Hugoniot curve always converges to $4\rho_0$; it can cross the limit due to extra microscopic degrees of freedom, and then the density can diminish as pressure still increases. An example of this behavior is shown on Figure (B.6) for deuterium.

III.3 The reshock states loci

Let us start with a sample in the state 0 ($\rho_0, P_0 \approx 0, T_0, E_0, u_0 = 0, U_{S0} = 0$). The principal Hugoniot is computed from the theoretical equation of state in the form of a collection of functions $P_H^0(\rho)$, $T_H^0(\rho)$, $E_H^0(\rho)$. Let us now consider a reshock from any state 1 on this principal Hugoniot (any ρ_1, and $P_1 = P_H^0(\rho_1)$ and so on). The rear quartz window is shocked by the sample in state 1, and the sample is shocked backwards at the interface into a state 2 with a shock front velocity U_{S2} and a particle velocity u_2. The conservation of pressure and velocities at the interface leads to:

$$P_2 = \rho_{quartz} U_{S,quartz} \cdot u_2 \tag{B.13}$$

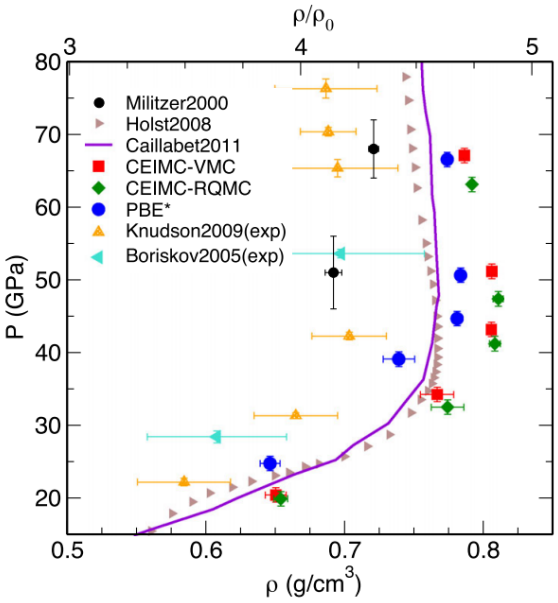

Figure B.6: Theoretical and experimental Hugoniot curve for deuterium, taken from [**?**]

Assuming a known equation of state for the quartz response $U_{S,quartz} = f_Q(u)$ (see, e.g, [**?**]), one can use this as a relation between P_2 and u_2. One can also calculate the reshock Hugoniot from the equation of state, leading to the following system:

$$\begin{cases} P_1 = P_H^0(\rho_1) & \text{(B.14)} \\ P_2 = P_H^1(\rho_2) & \text{(B.15)} \\ u_1 = \sqrt{P_1\left(\dfrac{1}{\rho_0} - \dfrac{1}{\rho_1}\right)} & \text{(B.16)} \\ U_{S1} = \dfrac{P_1}{\rho_0 u_1} & \text{(B.17)} \\ P_2 = P_1 + \rho_1(u_2 - u_1)(U_{S2} - u_1) & \text{(B.18)} \\ \rho_2 = \rho_1 \dfrac{U_{S2} - u_1}{U_{S2} - u_2} & \text{(B.19)} \\ P_2 = \rho_q f_Q(u_2) \cdot u_2 & \text{(B.20)} \end{cases}$$

the unknown being $u_1, u_2, P_1, P_2, \rho_2, U_{S1}, U_{S2}$, and ρ_1 varying along the principal Hugoniot curve. If one just wants the final loci ρ_2, P_2 of the reshocked states, the system may be expressed as:

$$\begin{cases} \dfrac{\rho_1}{1 - \rho_1/\rho_2}(u_2 - u_1)^2 - \rho_q f_Q(u_2) \cdot u_2 + P_H^0(\rho_1) = 0 & \text{(B.21)} \\ P_H^1(\rho_2) = \rho_q f_Q(u_2) u_2 & \text{(B.22)} \end{cases}$$

and solve it for u_2 and ρ_2 with ρ_1 as a fixed parameter, u_1 deduced from ρ_1, P_1 with (B.16) and $P_H^0 P_H^1, f_Q$ known equations of state.

Appendix C

Numerical Tables

Contents

I Water 132

I.1 DFT computations 132

I.2 OFMD computations 133

II Ammonia 134

III Methane 135

In this appendix chapter, we gather our table values for the equations of states of water, ammonia and methane.

I Water

I.1 DFT computations

T	ρ	P	U	Phase
6000	20	0166.80	034.061	SI
6000	25	0267.63	046.989	SI
6000	30	0390.48	060.208	SI
6000	35	0535.24	073.625	SI
6000	40	0700.66	087.061	SI
6000	45	0886.53	100.582	SI
6000	50	1091.84	114.154	SI
11000	20	0171.54	036.136	SI
11000	25	0273.33	049.143	SI
11000	35	0543.11	075.986	SI
11000	40	0709.97	089.440	SI
11000	45	0897.11	103.070	SI
11000	50	1095.89	115.292	SI
16000	20	0172.59	037.122	SI
16000	25	0274.36	050.175	SI
16000	30	0398.35	063.486	SI
16000	35	0543.68	076.892	SI
16000	40	0710.18	090.376	SI
16000	45	0897.12	103.861	SI
16000	50	1103.66	117.354	SI
20000	20	0174.69	038.268	Fluid
20000	25	0279.60	051.850	Fluid
20000	30	0401.46	064.540	Fluid
20000	35	0547.39	077.961	Fluid
20000	40	0714.42	091.445	Fluid
20000	45	0901.76	104.950	Fluid
20000	50	1109.50	118.446	Fluid
24000	20	0176.79	039.282	Fluid
24000	25	0279.76	052.195	Fluid
24000	30	0404.54	065.581	Fluid
24000	35	0551.19	079.000	Fluid
24000	40	0718.43	092.472	Fluid
24000	45	0906.77	105.980	Fluid
24000	50	1114.72	119.475	Fluid
30000	30	0409.22	067.019	Fluid
30000	35	0556.38	080.430	Fluid
30000	40	0724.81	093.917	Fluid
30000	45	0913.84	107.435	Fluid
30000	50	1122.72	120.926	Fluid
40000	07	0021.71	012.939	Fluid
40000	20	0185.11	043.021	Fluid
40000	25	0289.94	056.061	Fluid
40000	30	0416.82	069.367	Fluid
40000	35	0565.26	082.716	Fluid
40000	40	0734.89	096.219	Fluid
40000	50	1127.53	121.902	Fluid
50000	07	0023.61	015.253	Fluid
50000	15	0107.26	032.836	Fluid
50000	20	0190.31	045.311	Fluid
50000	25	0296.40	058.343	Fluid
50000	30	0424.62	071.632	Fluid
50000	35	0574.61	085.085	Fluid
50000	40	0745.49	098.560	Fluid
50000	45	0937.21	112.128	Fluid
50000	50	1137.17	123.646	Fluid

Table C.1: Numerical value for water EOS from DFT calculations. The energy reference is a calculation for an isolated water molecule. Densities are given in g·cm^{-3}, temperatures in K, pressures in Mbar and energies in eV/atom.

I.2 OFMD computations

T	ρ	P	U	Phase
6000	50	1093	114.2	SI
6000	60	1560	141.0	SI
6000	80	2723	194.1	SI
6000	100	4164	246.3	SI
11000	50	1097	115.6	SI
11000	60	1568	142.4	SI
11000	80	2723	195.5	SI
11000	100	4171	247.7	SI
16000	50	1102	116.9	SI
16000	60	1564	143.9	SI
16000	80	2747	197.0	SI
16000	100	4200	249.2	SI
20000	50	1108	118.1	SI
20000	60	1583	144.9	SI
20000	80	2756	198.1	SI
20000	100	4212	250.3	SI
30000	50	1121	120.7	SI
30000	60	1598	147.4	SI
30000	80	2778	200.8	SI
30000	100	4224	251.4	SI

Table C.2: Numerical value for water EOS from OFMD calculations. The energy reference is chosen to be consistent with the DFT calculations by equating the energies at 6000 K, 50 g.cm^{-3}. Densities are given in g·cm^{-3}, temperatures in K, pressures in Mbar and energies in eV/atom.

II Ammonia

T	ρ	P	U	Phase
2000	3	250.6	-78.521	SI
2000	4	566.6	-77.190	SI
2000	5	1012.9	-75.569	SI
2000	6	1591.5	-73.740	SI
2000	8	3110.1	-69.795	Solid
2000	10	5113.0	-65.463	Solid
2000	12	7641.0	-60.913	Solid
3000	3	247.0	-78.298	SI
3000	4	574.7	-76.931	SI
3000	5	1022	-75.310	SI
3000	6	1616.2	-73.428	SI
3000	8	3121.2	-69.534	SI
3000	10	5177.1	-65.201	SI
3000	12	7706.2	-60.608	SI
3000	15	12340.1	-53.574	SI
5000	2	87.5	-78.535	SI
5000	3	267.4	-77.768	SI
5000	4	597.3	-76.448	SI
5000	5	1055.0	-74.855	SI
5000	6	1637.8	-72.879	SI
5000	8	3190.9	-68.977	SI
5000	10	5252.2	-64.456	SI
5000	12	7797.6	-60.082	SI
5000	15	12502.1	-52.960	SI
10000	3	335.4	-76.263	Fluid
10000	4	678.3	-74.935	Fluid
10000	5	1153.2	-73.315	Fluid
10000	6	1756.0	-71.564	Fluid
10000	8	3346.2	-67.554	Fluid
10000	10	5441.9	-63.173	Fluid
10000	12	8031.8	-58.643	Fluid
10000	15	12200.0	-51.515	Fluid
15000	3	388.9	-75.242	Fluid
15000	4	750.1	-73.922	Fluid
15000	5	1239.5	-72.339	Fluid
15000	6	1860.8	-70.524	Fluid
15000	8	3498.2	-66.451	Fluid
15000	10	5630.1	-62.066	Fluid
15000	12	8260.0	-57.471	Fluid
15000	15	13098.3	-50.346	Fluid
20000	3	439.4	-74.256	Fluid
20000	4	816.8	-72.937	Fluid
20000	5	1330.1	-71.288	Fluid
20000	6	1967.2	-69.474	Fluid
20000	8	3634.6	-65.426	Fluid
20000	10	5809.6	-61.326	Fluid
20000	12	8477.3	-56.409	Fluid
20000	15	13365.4	-49.278	Fluid
25000	3	489.6	-73.302	Fluid
25000	4	883.3	-71.979	Fluid
25000	6	2074.5	-68.474	Fluid
25000	8	3771.5	-64.441	Fluid
25000	10	5989.5	-59.977	Fluid
25000	12	8686.5	-55.373	Fluid
25000	15	13630.9	-48.214	Fluid
30000	3	543.7	-72.239	Fluid
30000	4	955.9	-70.923	Fluid
30000	5	1501.2	-69.304	Fluid
30000	6	2177.7	-67.431	Fluid
30000	8	3911.2	-63.381	Fluid
30000	10	6149.7	-58.991	Fluid
30000	12	8891.4	-54.341	Fluid

Table C.3: Numerical value for ammonia EOS from DFT calculations. Densities are given in $g{\cdot}cm^{-3}$, temperatures in K, pressures in GPa and energies in eV/atom.

III Methane

T	ρ	P	U	Phase
1000	1	15.08	-43.686	Mol.
1000	1.5	63.28	-43.393	Mol.
1000	2	153.73	-42.936	Mol.
1000	3	462.12	-41.447	Mol.
1000	4	904.74	-39.644	Mol.
1000	5	1507.77	-37.777	Polym.
1000	6	2307.15	-35.731	Polym.
1000	8	4369.79	-31.141	Polym.
1000	10	7052.44	-21.684	Polym.
1000	12	10324.19	-22.120	Polym.
1000	15	16358.08	-15.014	Polym.
5000	1.5	75.16	-42.106	Polym.
5000	2	167.96	-41.589	Polym.
5000	3	479.01	-40.284	Polym.
5000	4	959.30	-38.635	Polym.
5000	5	1614.59	-36.738	Polym.
5000	6	2438.00	-34.679	Polym.
5000	8	4558.53	-30.310	Polym.
5000	10	7301.49	-25.729	Polym.
5000	12	10641.4	-21.025	Polym.
5000	15	16747.8	-13.820	Polym.
10000	1	38.85	-41.118	Polym.
10000	1.5	102.26	-40.099	Plasma
10000	2	205.75	-40.550	Plasma
10000	3	546.82	-39.280	Plasma
10000	4	1057.06	-37.574	Plasma
10000	5	1738.84	-35.670	Plasma
10000	6	2586.81	-33.584	Plasma
10000	8	4756.40	-29.202	Plasma
10000	10	7564.74	-24.533	Plasma
10000	12	10975.76	-19.784	Plasma
10000	15	17144.89	-12.592	Plasma
20000	1	78.224	-39.241	Plasma
20000	1.5	165.863	-39.102	Plasma
20000	2	292.626	-38.671	Plasma
20000	3	676.854	-37.375	Plasma
20000	4	1232.45	-35.689	Plasma
20000	5	1960.82	-33.708	Plasma
20000	6	2859.17	-31.614	Plasma
20000	8	5133.84	-27.138	Plasma
20000	12	11529.43	-17.689	Plasma
20000	15	17861.42	-10.396	Plasma
30000	1	119.04	-37.221	Plasma
30000	1.5	228.19	-37.096	Plasma
30000	2	377.42	-36.710	Plasma
30000	3	809.05	-35.435	Plasma
30000	4	1401.88	-33.754	Plasma
30000	5	2174.95	-31.821	Plasma
30000	6	3116.10	-29.676	Plasma
30000	8	5469.64	-25.196	Plasma
30000	10	8488.77	-20.417	Plasma
30000	12	12057.96	-15.642	Plasma
30000	15	18547.32	-8.311	Plasma

Table C.4: Numerical value for methane EOS from DFT calculations. Densities are given in g·cm^{-3}, temperatures in K, pressures in GPa and energies in eV/atom.

Appendix D

Useful formulae

Contents

I The atomic units system 138
II Unit conversions 138
III Physical constants 138
IV The degenerate electron gas 138

In this Appendix, we regroup some current useful constants and formulae, which can be used to estimate orders of magnitude.

I The atomic units system

The atomic units system is the most natural unit system for atomic properties: it is defined by:

$$\hbar = m_e = e^2 = 1 \tag{D.1}$$

As a consequence, the Bohr radius is the unit length, the Hartree is the unit energy and $c = 1/\alpha$. Hereafter, the atomic units will be denoted au.

II Unit conversions

Energies:	$1\text{erg} = 10^{-7}\text{J} = 2.2937\text{au}$
Forces:	$1\text{dyne} = 10^{-5}\text{N} = 121.38\text{au}$
Pressures:	$1\text{dyne}\cdot\text{cm}^{-2} = 0.1\text{Pa} = 3.399 \cdot 10^{-15}\text{au}$

III Physical constants

Einstein's constant	$c = 2.99792458 \cdot 10^8\text{m/s}$
Reduced Planck's constant	$\hbar = 1.054571726 \cdot 10^{-34}$
Boltzmann's constant	$k_B = 1.3806488 \cdot 10^{-23}\text{J/K} = 3.167 \cdot 10^{-6}\text{au} = 8.617 \cdot 10^{-5}\text{eV/K}$
Electron's charge	$e = 1.60217657 \cdot 10^{-19}\text{C} = 4.803 \cdot 10^{-10}\text{esu}$
Electron's mass	$m_e = 9.10938215 \cdot 10^{-31}\text{kg} = 0.511\text{MeV}$
Bohr's radius	$a_0 = 5.2917721092 \cdot 10^{-11}\text{m} = 0.529\mathbf{r}\text{A}$
Fine structure constant	$\alpha = \frac{e^2}{\hbar c} = 7.2973525698 \cdot 10^{-3} \sim 1/137$

IV The degenerate electron gas

Let us give some typical formulae of the equation of state, in both the non-relativistic and ultra-relativistic limits. For the Fermi energy:

$$E_{F,NR} = \frac{1}{2} mc^2 x_F^2 \tag{D.2}$$

$$E_{F,UR} = mc^2 x_F \tag{D.3}$$

with $mc^2 \sim 0.5\text{MeV}$. For the pressure, we get:

$$P_{NR} = \frac{1}{5} P_q x_F^5 \tag{D.4}$$

$$P_{UR} = \frac{1}{4} P_q x_F^4 \tag{D.5}$$

with $P_q = \frac{1}{6\pi^2} \left(\frac{mc}{\hbar}\right)^3 \sim 4 \cdot 10^{17}\text{atm}$.